Title

Temperature-Dependent Studies on the Photophysics and Ligand Shell Structure of CdSe/CdS Quantum Dots

Author

Balan, Arunima Deya

Publication Date

2019

Peer reviewed|Thesis/dissertation

Temperature-Dependent Studies on the Photophysics and Ligand Shell Structure of CdSe/CdS Quantum Dots

by

Arunima Deya Balan

A dissertation submitted in partial satisfaction of the

requirements for the degree of

Doctor of Philosophy

in

Chemistry

in the

Graduate Division

of the

University of California, Berkeley

Committee in charge:

Professor A. Paul Alivisatos, Chair
Associate Professor Naomi Ginsberg
Professor Feng Wang

Spring 2019

Temperature-Dependent Studies on the Photophysics and Ligand Shell Structure of CdSe/CdS Quantum Dots

Abstract

Temperature-Dependent Studies on the Photophysics and Ligand Shell Structure of CdSe/CdS Quantum Dots

by

Arunima Deya Balan

Doctor of Philosophy in Chemistry

University of California, Berkeley

Professor A. Paul Alivisatos, Chair

Colloidal quantum dots (QDs) are a class of materials that have received significant interest due to their disinctive optical properties when compared to other materials. Their tunable, sharp, and bright emissions, improved photostability, and high molar extinction coefficients make them of interest to a number of fields. In addition, QD structures can be synthesized with different compositions and geometries in order to maximize luminescence efficiency, or rates of charge separation. The presence of a shell of surface ligands provides another mechanism by which the properties of QDs can be tuned, including their photoluminescence and coupling with other QDs or molecules. Effective utilization of QDs in a number of applications is reliant upon understanding how to efficiently radiatively recombine or separate photoexcited carriers, while minimizing undesirable loss mechanisms. To better control photoexcited charges in QD systems, it is necessary to understand the mechanisms that underpin each charge recombination process. Because these processes are often complex and interconnected, knowing the temperature-dependence can be used to determine the relevant energetics governing excited state processes, which often yields mechanistic insights. In addition, developing an understanding the structure of the QD surface allows for further control of QD properties.

In Chapter 1, I will introduce different excited state relaxation pathways in colloidal QDs. The roles of the core/shell interface, binding of surface ligands, interactions involving the ligand tail group, and redox-active ligands in modulating QD properties will be discussed. In addition, I will briefly describe why performing temperature-dependent measurements is of interest for each of these parameters.

Chapter 2 shows how the presence of the core/shell interface modulates the radiative rate. This leads to a decrease in the radiative rate in CdSe/CdS QDs as temperature is increased. How this relationship is impacted by both core size and shell thickness is described. In addition, different factors that can impact the radiative rate, including thermal fluctuations, and electronic excitations are evaluated computationally to show which factors most change the radiative rate.

In Chapter 3, I show how the temperature-dependent structure of the ligand shell is modified by the ligand composition. Introduction of either short chain ligands or a ligand with a *cis* double bond shifts an order/disorder transition within the ligand shell to lower temperatures. This order/disorder transition is observed experimentally using both temperature-dependent photoluminescence and infrared spectroscopies. The observed behavior is then explained by invoking a simple lattice model, which shows how domains of one ligand can seed disorder into another.

In Chapter 4, I will describe temperature-dependent studies of hole transfer from photoexcited QDs to molecular acceptors. The observed temperature-dependence of the hole transfer rate found does not match with several Marcus theory models of the charge transfer process. Using a trap-mediated hole transfer model, the temperature-dependence can be explained. This observation indicates the importance of reversible surface trapping in changing QD properties. Finally, Chapter 5 will discuss the findings found in this dissertation and provide an outlook for future experiments.

Acknowledgments

I would like to begin by thanking my advisor, Prof. Paul Alivisatos for fostering a scientifically curious, thorough, and supportive lab environment. His ability to concisely describe the physical chemistry principles underpinning any number of complicated phenomena made presenting results to him particularly useful in honing my understanding of my research projects and allowed me to grow as a scientist.

Thank you to my two graduate student mentors, Dr. Jacob Olshansky and Dr. Tina Ding, who helped get me settled in the Alivisatos group and started on these projects. They made sure that our subgroup was a source of information and entertainment to me and other members in the group, and helped me learn how to analyze data under a time crunch. Additionally, Jacob performed much of the work detailed in Chapter 4, and he and Tina developed the model system of ferrocene derivatives bound to CdSe/CdS QDs used in Chapter 4.

I have been fortunate to be able to collaborate with a number of people, including Prof. Eran Rabani, Dr. Hagai Eshet, Dr. Yonatan Horowitz, and Dr. Hui-Ling Han. Without them, there would be no computational results from Chapter 2, or SFG results from Chapter 3. In addition, numerous members of the group have been helpful with developing the low temperature infrastructure in the group, including Dr. Son Nguyen and Dr. Jianbo Gao. A number of other members in the Alivisatos group have been a great source of support and discussions, including Dr. Noah Bronstein and Dr. Erin O'Brien. I would also like to thank an undergraduate student that I worked with, Lucio Tang, who was patient with me as I learned how to be a mentor and helped with several projects.

Finally, I would like to thank my family and friends, who provided support and perspective throughout the highs and lows of graduate school.

Contents

Contents **ii**

List of Figures **iv**

List of Tables **vi**

1 Introduction **1**
1.1 General properties of quantum dots 1
1.2 Quantum dot photophysics governs potential applications 2
1.3 Effect of the shell material 3
1.4 The semiconductor/organic interface 6
1.5 Role of the ligand tail group 7
1.6 Charge transfer to redox-active ligands 8
1.7 Understanding temperature-dependent rates and phases in QDs 10

2 Temperature-Dependent Behavior of the Radiative Rate **12**
2.1 Background 12
2.2 Synthesis and sample photoluminescence data 13
2.3 Relevant energy scales 16
2.4 Comparison of the change in PL peak 17
2.5 Understanding the change in radiative lifetime with temperature 19
2.6 Conclusions 23

3 Temperature-Dependent Structure of Mixed Ligand Shells **24**
3.1 Background 24
3.2 QD synthesis and surface characterization 25
3.3 Temperature-dependent photoluminescence measurements 27
3.4 Temperature-dependent IR spectroscopies 30
3.5 Composition-dependent behavior 33
3.6 Ising model with induced disorder 36
3.7 Additional ligand compositions 39
3.8 Discussion 42
3.9 Conclusions 45

4 Temperature-Dependent Hole Transfer From Photoexcited QDs **46**
4.1 Background . . . 46
4.2 Room temperature hole transfer . . . 46
4.3 Temperature-dependent hole transfer measurements . . . 50
4.4 Analysis of the temperature-dependence . . . 51
4.5 Evidence for trap-mediated hole transfer . . . 52
4.6 Conclusions . . . 56

5 Concluding Remarks **58**

Bibliography **59**

A Synthetic Methods **66**
A.1 Chemicals . . . 66
A.2 CdSe core synthesis . . . 66
A.3 CdSe/CdS synthesis . . . 67
A.4 Ligand Exchanges . . . 67

B Spectroscopic and Computational Methods **69**
B.1 Cryostat PL and TRPL measurements . . . 69
B.2 Temperature-dependent integrating sphere measurements . . . 70
B.3 VT-FTIR measurements . . . 74
B.4 SFG measurements . . . 75
B.5 PL quenching curves . . . 75
B.6 Quantitative NMR . . . 75
B.7 TEM . . . 75
B.8 Determination of QD concentrations . . . 75
B.9 Ising model simulation . . . 76
B.10 Computation of temperature-dependent emissions and lifetimes . . . 76

List of Figures

1.1 Densities of states associated with 0D to 3D confinement 2
1.2 The effect of a QD shell on photophysical processes 4
1.3 Ligand binding motifs in II-VI QDs 6
1.4 Marcus theory schematic 9

2.1 Sample temperature-dependent PL data 13
2.2 Sample temperature-dependent TRPL data 15
2.3 Temperature-dependent PLQY of the 3.4 nm core, 9.7 nm total diameter QD . . 15
2.4 Energy scales relevant in CdSe/CdS QDs 16
2.5 Change in PL with temperature 18
2.6 Change in lifetime with temperature 20
2.7 Low-lying excited states for the different samples 21
2.8 Change in electron and hole probability densities due to lattice fluctuations . . . 22

3.1 Schematic of an order/disorder transfer within the ligand shell 25
3.2 Ligand exchange to ODPA and NMR quantification 26
3.3 Observing the ligand phase transition through PLQY and TRPL 28
3.4 Temperature-dependent PL of ligand-exchanged QDs 29
3.5 VT-FTIR data of two ligand compositions 30
3.6 Temperature-dependent SFG spectra 32
3.7 Comparison of the s-CH_3/s-CH_2 ratio 33
3.8 Phase transition temperature and width 34
3.9 Phase transition temperature using the numerical derivative 35
3.10 Ising-like model schematic 37
3.11 Ising simulations of the ligand phase transition 38
3.12 Temperature snapshots of the phase transition 39
3.13 Dependence of phase transition temperature on chain length 40
3.14 Phase transition behavior with stearic acid 41
3.15 Phase transition behavior assuming segregated OA and ODPA 44

4.1 Energy level diagram for hole transfer 47
4.2 Room temperature quenching curves 48

4.3 RT dependence of rate on driving force 49
4.4 Temperature-dependent hole transfer measured by TRPL 50
4.5 Temperature-dependent hole transfer rates measured using PLQY 52
4.6 Marcus theory models of temperature-dependent charge transfer 53
4.7 Arrhenius behavior for the 6.3 nm QDs 54
4.8 Two-step hole transfer process energy diagram 55
4.9 Global fits to the two-step hole transfer model 56

B.1 QD quenching for different sample cell materials 69
B.2 Temperature calibration using emission 71
B.3 Temperature calibration using emission and time 72
B.4 Newton's law of cooling fits 72
B.5 External QD for temperature calibration 73
B.6 Phase transition behavior using same QDs as the calibrant 74
B.7 QD PLQY using the external calibrant 74

List of Tables

2.1 Sizes and PLQY of CdSe/CdS for TRPL studies 13

3.1 NMR quantification of ligand binding 27

Chapter 1

Introduction

1.1 General properties of quantum dots

Semiconductor nanocrystals, also known as quantum dots (QDs), have distinct properties from their bulk counterpart. The energy levels of bulk semiconductors are represented as continuous bands, as shown in Figure 1.1. An electron from the valence band (highest energy filled band) can be promoted (often through absorption of a photon) to the conduction band (lowest energy empty band). This excitation produces a negative charge (electron) that is now in the conduction band, and an associated positive charge (hole) that is now in the valence band. Both electron and hole can be described as quasiparticles that have an effective mass given by the dispersion of the conduction or valence band, respectively. When any of the dimensions of the semiconductor are shrunk to the nanoscale, the energy levels are no longer full bands, but have discrete features depending on the degree of confinement. As the semiconductor is confined in one (plate), two (wire), and three (QD) dimensions, the density of states becomes more discrete and molecule-like, as described in Figure 1.1.[1]

The energy levels of QDs can be described using a quantum mechanical particle-in-a-box model, and results in the size-dependent absorption and photoluminescence properties that are characteristic of QDs. The Böhr exciton radius, a_B, is the length scale that governs the degree of confinement. When a_B is larger than the radius of the QD, the QD can be considered to be in the strong confinement regime and the properties are most sensitive to the size of the QD. For example, the Böhr exciton radius of CdSe is 5.6 nm, and changing the particle radius of CdSe QDs between 1 and 4 nm will shift the absorption and emission peaks almost 1 eV across most of the visible spectrum.[2,3] In addition to a change in the energy levels arising from quantum confinement, the Coulomb interaction between the electron and hole must also be considered. This is because both electron and hole have been confined into a smaller space and now interact more strongly. For this reason, to better describe QD properties, such as the optical band gap, electron-phonon coupling, and degree of charge localization, it is necessary to include electron-hole interactions.[4]

The significant increase in surface area as materials are shrunk to the nanoscale is another factor that governs QD properties. Atoms at the surface are not fully coordinated, and thus are bonded less strongly than the bulk. The higher surface energy can result in changes in pressure- and temperature-dependent phase transitions.[5,6] The presence of these undercoordinated atoms at the surface can also create electronic states within the bandgap, which can trap either the electron or hole and are discussed later in this Introduction. Often, QD properties such as their photoluminescence (PL) or stability are improved by isolating the QD

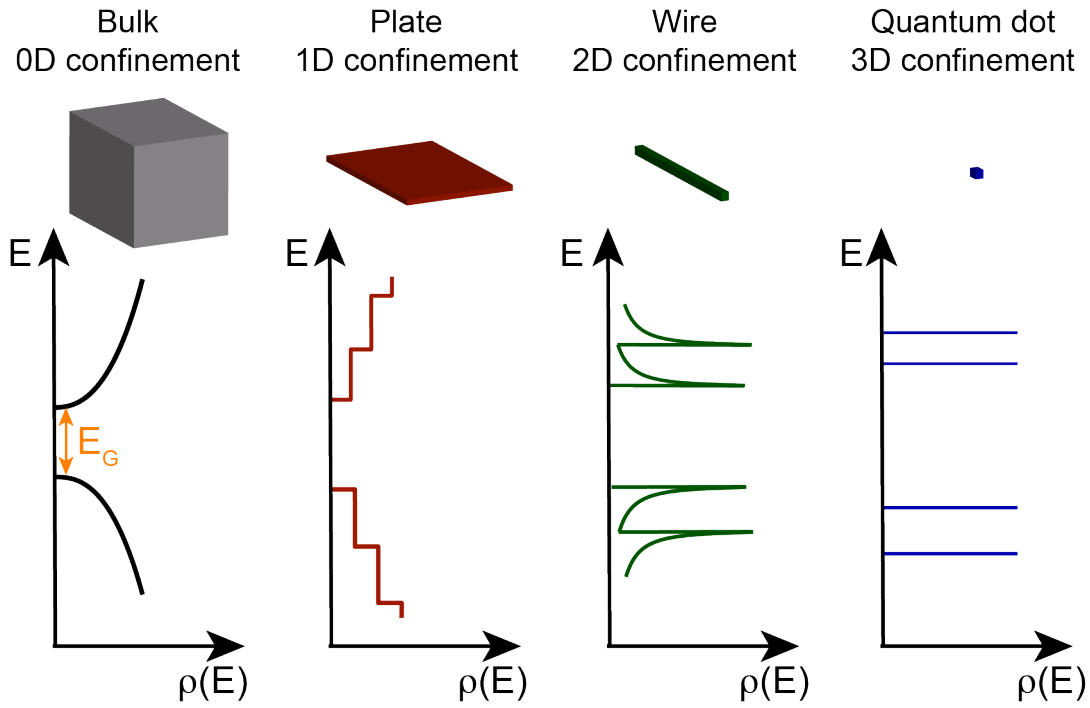

Figure 1.1: Densities of states associated with 0D to 3D confinement for a semiconductor material. The band gap for the bulk semiconductor is shown in orange.

from the surface by growing a shell of another material.[7,8] The surface in nanoscale systems can also be harnessed by tuning its composition or faceting to enable specific heterostructure growth or to change the optical properties of QDs.[9–11]

There is significant diversity in the types of QDs that can be synthesized, ranging from elemental semiconductors such as Si[12,13] to quaternary semiconductors such as Cu-In-Ga-S[14] to ionic materials such as the $CsPbX_3$ X=(Cl,Br,I) perovskites.[15,16] While QDs can be synthesized a number of ways, this dissertation will focus on colloidal QDs. In colloidal QDs, there is shell of organic ligands around the semiconductor material that helps ensure colloidal stability. This shell of organic ligands provides another way by which to control the properties of colloidal QDs.

1.2 Quantum dot photophysics governs potential applications

The size-tunable, bright, and narrow emission that arises from quantum confinement in QDs makes them of interest for a number of applications.[2] For example, QDs have the potential to be used as luminescent labels for bio-imaging[2,11] and in displays and solid-state lighting.[17] In addition, due to the ability to modify the QD structure by combining

other materials in different morphologies, QD structures can be designed to maximize charge separation.[18,19] Such QD architectures are of interest to a different class of applications, which rely upon effective light absorption by the QDs and then fast charge transfer. The resulting separated charges are then used to drive photovoltaic processes[20] and a number of photocatalytic reactions, including hydrogen evolution,[21,22] C-C coupling reactions,[22,23] and CO_2 reduction.[24,25] In these applications, the rate of charge transfer must be designed to out-compete radiative and undesirable nonradiative recombination pathways.

An understanding of the interplay among excited state rates is necessary to better design complex QD structures for various applications. The large number of excited state pathways by which electron and hole can recombine is shown schematically in Figure 1.2, and illustrates the complexity of QD systems. Understanding the temperature-dependent behavior of each of these rates can yield mechanistic insights. In particular, low temperature measurements are useful as by reducing the thermal energy, the underlying processes that govern excited state dynamics can be elucidated. For example, previous low temperature studies of the photoluminescence lifetime of QDs have given insight into the exciton fine structure in CdSe QDs[26,27] and temperature-dependent studies have also resulted in an improved understanding of the energy distribution and rates of surface trapping processes.[28–30]

While there is great structural diversity in QD materials as described in Section 1.1, this dissertation will focus on understanding CdSe/CdS QDs, as they are a prototypical QD system. It is possible to synthesize CdSe/CdS QDs in a number of morphologies, including as "spherical" core/shells,[7,31] dot-in-rod structures,[9,32,33] and nanoplatelets.[34] The small lattice mismatch (<5%) between the CdSe and the CdS makes it possible to grow epitaxial shells of varying thickness without placing undue strain at the core/shell interface.[7,31] Furthermore it is possible to synthesize these materials with high photoluminescence quantum yield (PLQY)[7,33] and to control and quantify the surface composition.[35] In this Introduction the role of the QD shell, the inorganic/organic interface, and the ligand tail group in modulating the photophysics and behavior of CdSe/CdS QDs will be discussed, as will the potential temperature-dependence for each of the rates.

1.3 Effect of the shell material

The growth of a shell in colloidal QDs can impact both the rate of charge trapping and the radiative recombination rate. Charge trapping is a deleterious process during which either the electron and hole localizes to a defect either at the surface or within the semiconductor material. This process can be either reversible or irreversible, which can result in delayed emission,[36] nonradiative recombination,[10] and photodegradation of QDs.[37,38] Charge trapping behavior can be due to both surface trapping and trapping to the core/shell interface, as indicated in Figure 1.2. By growing a Type I shell around the core, surface charge trapping and charge transfer processes are decreased due to the presence of a tunnel barrier that decreases the coupling between the exciton and the surface.[7,18] This results in a greater PLQY and greater photostability for Type I core/shell materials.[7] However, if the interface

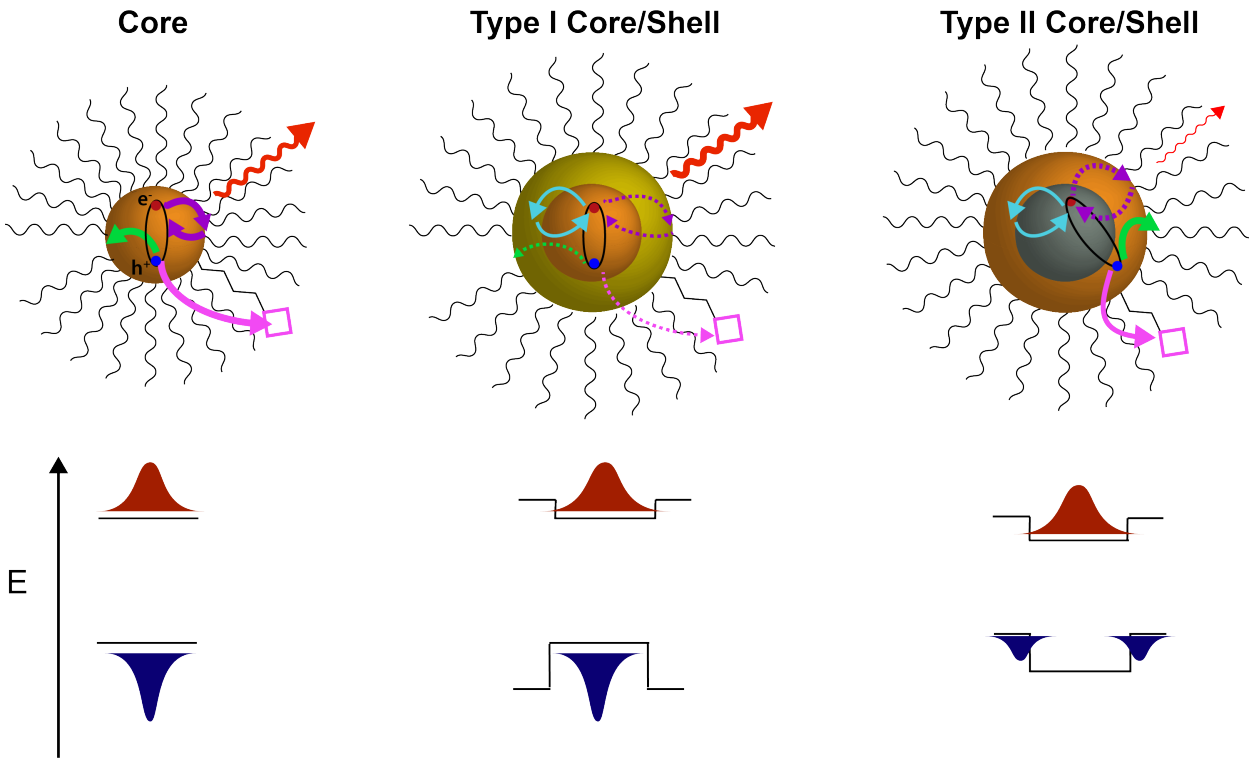

Figure 1.2: The effect of a QD shell on photophysical processes is shown for a core, Type I core/shell and a Type II core/shell QD. Upon photoexcitation, there a number of pathways by which the electron and hole can recombine, including radiative recombination (red arrow), surface reversible charge trapping (purple arrow), surface irreversible charge trapping (green arrow), interfacial charge trapping (cyan arrow), and charge transfer to molecular species (pink arrow). The thickness of the arrow indicates the magnitude of each process for the different structures. There is suppressed surface trapping for the Type I core/shell and for one charge in the Type II core/shell. Schematics of the electron and hole probability densities, which govern these processes, are also shown.

between the core and shell materials is not ideal, growth of a shell can result in interfacial charge trapping processes.[39] Type II QDs reduce the charge trapping for one charge (the electron in Figure 1.2), but do not improve charge trapping processes for the other charge.

The growth of a shell also impacts the radiative rate for core/shell QDs. The radiative rate (rate of spontaneous emission) is given by Fermi's Golden Rule and the Einstein coefficients, shown in Equation 1.1.[40]

$$k_r = \frac{\omega^3 n^3}{3\pi\varepsilon_0 \hbar c^3} |\mu_{12}|^2 \tag{1.1}$$

ω describes the angular frequency of the transition, and all other constants have their traditional definitions. From equation 1.1 the main parameter that can be tuned is μ_{12}, the transition dipole moment. The transition dipole moment can be broken up into two parts in QDs: one that is governed by the symmetries of the underlying orbitals and one by electron-hole overlap.[41] As the symmetries of the underlying orbitals can primarily be changed by using a different material, the electron-hole wavefunction overlap is the main tunable parameter and is modified through the addition of different types of shell materials. The addition of a Type-I shell, in which both electron and hole prefer to reside in the core would result in similar radiative rates between the core and the core/shell material. However, the addition of a Type-II shell can have a significant impact on the radiative rate. In a Type-II configuration the electron and hole prefer to reside in different materials, resulting in significantly less electron-hole overlap and a slower radiative rate.[42] This behavior is shown schematically in Figure 1.2.

CdSe/CdS is neither fully Type I nor Type II, which somewhat changes how the core/shell interface impacts QD excited state dynamics. In CdSe/CdS the hole is strongly confined to the CdS core due both to the 400 meV valence band offset and the effective mass of the heavy hole, $0.6m_e$, where m_e is the electron rest mass. The heavier effective mass results in a smaller confinement energy for the hole, and therefore significantly less tunneling into the shell. However, for the electron the 300 meV conduction band offset is of similar order of magnitude to the increased kinetic energy of the electron due to quantum confinement.[43] This would allow a single electron to more easily access states in the CdS shell, but due to the presence of the hole that remains confined to the core, the electron is attracted back to the core by a Coulomb interaction with the hole.[44,45] As a result the radiative rate in CdSe/CdS QDs is highly dependent on the precise dimensions of both the CdSe core and the CdS shell, with larger CdS shells and smaller CdSe cores resulting in slower radiative rates.[31,45]

For ideal two-state systems, a change in the radiative rate with temperature is not expected, because the radiative rate is fundamentally quantum mechanical in character. However, QDs are not a simple two-state system. In multi-level systems the observed radiative rate is not a simple formula, but is weighted over accessible electronic states as shown in equation 1.2, as long as the exciton is in thermal equilibrium. For example, due to both the exciton fine structure and the presence of confined phonon modes, at low temperatures there is a drastic increase in the excited state lifetime due to the presence of a "dark"

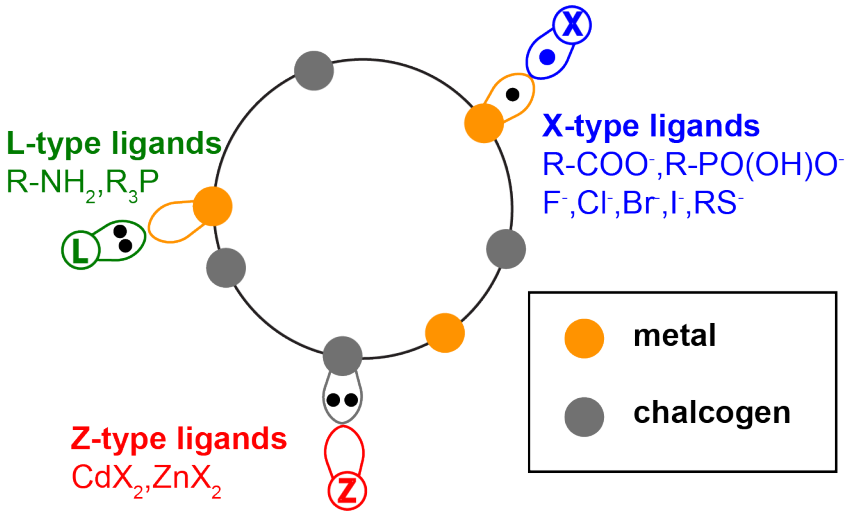

Figure 1.3: Ligand binding motifs in II-VI QDs

excitonic state.[26,27,46,47] In addition to the exciton fine structure, other states within the system can also impact the radiative rate. At higher temperatures, there are also a number of accessible excitations of the lattice and of the exciton, which results in a complex temperature-dependence of the radiative rate.

$$k_r(T) = \sum_{\nu} k_{r,\nu} \times \exp\left(-E_\nu / k_B T\right) \tag{1.2}$$

1.4 The semiconductor/organic interface

Due to the significant increase in the surface area to volume at the nanoscale, understanding the role of the semiconductor/organic interface in QD photophysics is essential. Undercoordinated atoms at the surface of the QD (both metal and chalcogen) create defect states within the band gap, which are sites at which electron and hole can nonradiatively recombine. This charge trapping behavior can be mitigated by passivating the QD surface through ligand binding. Surface ligands can bind to the QD in three main binding motifs, consistent with Green's covalent bond classification method: either L, X, or Z type, shown schematically in Figure 1.3.[48,49] L-type ligands provide two electrons in their interaction with the QD surface, forming a dative covalent bond. Common L-type ligands used in QD syntheses and surface passivation include amines (such as oleylamine) and phosphines (such as tri n-octyl phosphine (TOP)). Since L-type ligands do not change the charge balance of the QD surface, they typically can be displaced through sufficient cleaning steps. For example, although the synthesis of wurtzite-CdSe QDs is performed in an excess of TOP, NMR of cleaned CdSe QDs shows no TOP bound to the surface.[50] Despite the weaker binding of L-type ligands, addition of amines and phosphines to CdSe QDs have been shown to signifi-

cantly improve the photoluminescence properties, indicating that such ligands can effectively passivate undercoordinated metal sites.[51,52]

The second class of ligands are X-type ligands, which bind through a traditional covalent bond, where the ligand and the metal each contribute one electron to the bond. In QDs typical X-type ligands include carboxylates, phosphonates and thiols. These ligands additionally serve to provide charge balance to the QD surface, and thus are difficult to displace in nonpolar organic solvents without performing a ligand exchange.[49,53] Both X-type and L-type ligands bind to the metal (Cd) of the QD surface, and as the metal orbitals comprise the majority of the states near the bottom of the conduction band, X- and L-type ligands passivate electron traps.[10,52]

The third type of ligands are Z-type ligands, which accept two electrons contributed by the QD surface. Typical Z-type ligands in QDs are CdX_2 ligands, in which two X-type ligands bind to a Cd cation, producing a neutral ligand. Such ligands bind to undercoordinated chalcogen sites at the surface of the QD and are thought to help passivate hole traps. As a result, as the excess amount of Cd in the QD is increased (the surface becomes more Cd rich), the PLQY also increases.[49,52] Since Z-type ligands, like L-type ligands, are charge neutral they can desorb from the the QD surface without disrupting the charge neutrality of the QD. However, promoting Z-type desorption is somewhat harder than getting L-type desorption. Previous work has shown that adding an excess of L-type ligand to a QD solution can induce such Z-type desorption from the QD surface, often associated with a decrease in the PLQY of the QD.[49]

While a number of studies utilize room temperature time-resolved photoluminescence and PLQY to gain information about surface traps,[10,51,52] temperature-dependent measurements can also provide useful information. For example, temperature-dependent studies of defect luminescence in CdSe QDs suggest that the observed luminescence can be explained through charge trapping to a single shallow trap.[29] Temperature-dependent studies of the time-resolved photoluminescence show complex behavior that can be explained through passivation through charge transfer to a series of surface traps.[28] Understanding the temperature-dependence of surface trapping processes can be helpful in designing systems with higher PLQY and the roles different ligands play in the charge trapping behavior.

1.5 Role of the ligand tail group

Just as the ligands can control charge trapping behavior through head group binding, the ligand tail group (R in Figure 1.3) mediates interactions between the QD and the surrounding environment. In applications that rely upon electronic coupling between QDs long aliphatic ligands are replaced with shorter chain or all-inorganic ligands, or removed entirely to enhance charge mobility through QD films.[54–57] Similarly, exciton diffusion within films of QDs can be modulated by changing the chain length of the aliphatic ligands.[58,59] Additionally, the solubility of the colloidal QDs can be modified through changing the ligand tail groups. Introduction of branched chains into the ligand tail group can modify the solubility limit

of QDs in toluene over four orders of magnitude.[60] By adding polar groups (ex. carboxylic acids, poly-ethylene glycol etc.) to the end of the ligand tail group, QDs can be stabilized in water and other polar solvents.[2,61,62]

In addition to the composition of the ligand shell playing a significant role in QD properties, the conformation of the ligands in the shell can also be tuned. Long, aliphatic ligands on the surface of QDs and other materials interact *via* van der Waal's interactions between the chains. In these systems there is an enthalpic driving force for the chains to pack, but as temperature increases the entropy associated with disordering the chains dominates. This results in an order-disorder phase transition within the ligand shell. Such transitions have been previously observed in experimental studies of amine-capped CdSe QDs[63] and studied computationally on CdS QDs and nanorods.[64,65] A similar transition has also been studied in alkanethiolate-capped Au nanoparticles.[66–68]

Molecular dynamics simulations show that the order/disorder phase transition in the ligand shell of CdS nanorods modulates the interaction potential between these rods, resulting in a nanorod attraction in the ordered phase.[64] The change in ligand conformation can impact other properties, including their solubility in different solvents.[60,69] Similarly, the inter-ligand interactions can impact the crystal structure of QD superlattices.[70] For example, the distance between PbS QDs in a superlattice does not depend linearly on the number of carbons in the aliphatic tail due to a phase transition that disorders longer chains. Shorter chains accommodate upright ligands, while longer ligands can adopt a more compact, disordered, profile.[59,71] Finally, the ligand shell permeability depends on the conformation of the surface ligands. For example, the Au deposition motif on CdS nanorods changes from depositing on the tips to depositing on the sides as the the ligand shell composition and temperature change, which corresponds to a ligand phase transition in the amine ligands.[63,72] Temperature-dependent measurements are vital in developing a more complete understanding of such phase transitions on the surface of the QD, which could have a significant role in modifying properties of colloidal QDs.

1.6 Charge transfer to redox-active ligands

The ligand shell of QDs can be additionally modified through the addition of redox-active ligands. In such systems, an electron (hole) can be extracted from the QD via reduction (oxidation) of the redox-active ligand. In molecular species, such charge transfer processes can be described using the framework of Marcus electron transfer theory.[73] Marcus theory assumes a parabolic potential *versus* a combined nuclear reaction coordinate for both the initial and final electronic states (DA and D^+A^-), as described in Figure 1.4A. In the Born-Oppenheimer approximation the electron moves along the nuclear potential energy curves, and can only transfer when the two states are isoenergetic (when the parabolae cross). The associated activation energy is given by the energy of this crossing point. The combined nuclear reaction coordinate includes the change in bond lengths of the donor and acceptor and a change in the polarization of the solvent during the charge transfer process. The

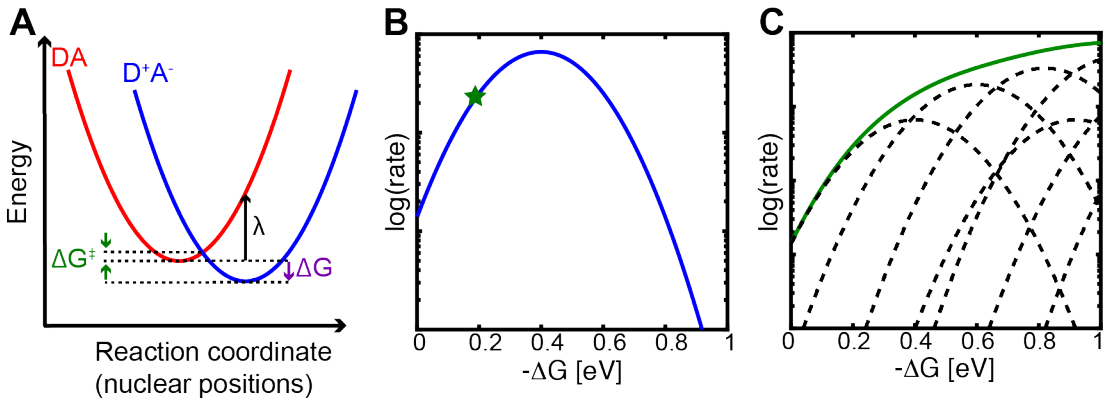

Figure 1.4: Marcus theory schematic A Shows the potential energy surfaces and relevant parameters. B shows the relationship between charge transfer rate and driving force. The green star indicates a driving force corresponding to the schematic shown in A. C shows the relationship between charge transfer and driving force for the auger-assisted (multi-state) model. The dashed lines indicate individual Marcus parabolas, and different heights indicate different degeneracies. The reorganization energy for both B and C is 0.4 eV.

reorganization energy, λ, corresponds to the energy associated with changing the solvent polarization and molecular bond lengths in the system to the final configuration without transferring a charge as shown schematically in Figure 1.4A. Using these approximations, the rate of charge transfer is given by equation 1.3, where $|H_{DA}|^2$ describes the donor-acceptor coupling. The temperature-dependence of the exponential pre-factor arises from the partition function of the electron moving along a harmonic potential. At high driving forces (greater than the reorganization energy) Marcus theory predicts an inverted regime, as shown in Figure 1.4B, in which the rate decreases as the driving force increases, due to the difficulty of the nuclei to rearrange to accommodate the charge transfer process, and was first observed by Closs et al. in molecular systems.[74]

$$k_{CT} = \frac{2\pi}{\hbar}|H_{DA}|^2 \frac{1}{\sqrt{4\pi\lambda k_B T}} \exp\left(-\frac{(\lambda + \Delta G)^2}{4\lambda k_B T}\right) \tag{1.3}$$

Charge transfer from photoexcited QDs to bound or adsorbed molecular species is more complex than in molecular acceptors. As there can be multiple ligands bound to the surface of a QD, the charge transfer rate varies linearly with the number of bound redox-active ligands.[18] Despite this complicating factor, charge transfer in QD systems has been studied through a number of techniques, including transient absorption and photoluminescence (PL) quenching.[18,75–80] For both hole and electron transfer from QDs to molecular species, the Marcus inverted regime has not been observed.[75,76] Instead, as the driving force is increased there is a steady increase in the charge transfer rate.

The strong electron-hole interaction present in QDs has been invoked to rationalize the

lack of an inverted regime in QD to molecular charge transfer.[75,76,81] At high driving forces, Marcus theory predicts an inverted regime due to the difficulty of the system to reorganize into a configuration such that the charges can transfer. However, if there is another mechanism by which the energies of the initial and final states can be equalized, fast charge transfer can be achieved at high driving forces. Strong coupling between electron and hole allows for an Auger-like process by which during hole (electron) transfer the remaining electron (hole) can be excited into higher conduction (valence) band states. This reduces the degree to which the system has to reorganize at high driving forces, and can be described by Equation 1.4. Rather than the charge transfer rate being described by one Marcus parabola, as shown in Equation 1.3, it is described by a sum of Marcus parabolae offset by the degree of excitation of the remaining charge. Although nominally the donor-acceptor coupling could also change depending on the excitation of the remaining charge, as the major overlap is between the transferring charge and the acceptor molecule, previous studies have neglected any change in the donor-acceptor coupling.[75,76]

$$k_{CT} = \frac{2\pi}{\hbar}\frac{1}{\sqrt{4\pi\lambda k_B T}}\sum_i |H_{DA}|^2 \exp\left(-\frac{(\lambda + \Delta G + E_i)^2}{4\lambda k_B T}\right) \tag{1.4}$$

Temperature-dependent studies of charge transfer from photoexcited QDs are of interest as they can help determine the activation energy associated with the charge transfer process. In the QD systems, the lack of an inverted regime suggests that the charge transfer process cannot be explained by simple two-state Marcus theory. While one potential explanation for the fast charge transfer even at large driving forces is the Auger-assisted charge transfer mechanism, there are other factors that could also result in the observed behavior. For example, a trap-mediated charge transfer mechanism could result in a more variable effective driving force and therefore a lack of an inverted regime. In addition, previous work on molecular charge transfer processes has shown that coupling to high energy vibrational modes is another process by which the system can effectively reduce the activation barrier at high driving forces.[74] Measuring the activation energy of the charge transfer process could be useful in evaluating the accuracy of current theories of QD charge transfer, and can be most easily achieved through temperature-dependent measurements.

1.7 Understanding temperature-dependent rates and phases in QDs

As described in the previous sections, each interface present in colloidal QDs can have a significant impact on their observed properties and the excited state rates. In this dissertation, two techniques are used to measure the excited state rates. Time-resolved photoluminescence (TRPL) can be used to measure the excited state lifetime. The time constant of the decay, τ, is related to both the radiative rate, k_r, and all nonradiative rates, k_{nr}, which can include the charge transfer rate, as shown in Equation 1.5a. An increase in τ corresponds to

either a decrease in k_{nr} or k_r. The other technique useful in determining both the radiative and nonradiative rates is PLQY, shown in Equation 1.5b. An increase in PLQY tends to be attributed to a decrease in k_{nr}, although a sharp increase in k_r would also increase the PLQY.

$$\tau = (k_r + k_{nr})^{-1} \tag{1.5a}$$

$$\text{PLQY} = \frac{k_r}{k_r + k_{nr}} \tag{1.5b}$$

In the next chapters of this dissertation, I will describe work that has been undertaken to better understand the role of the core/shell interface in modulating the radiative rate (Chapter 2),[82] the temperature-dependent phase behavior of mixed ligand shells and how that impacts charge trapping (Chapter 3), and how temperature-dependent hole transfer is impacted by the presence of reversible surface traps (Chapter 4).[83]

Chapter 2

Temperature-Dependent Behavior of the Radiative Rate

2.1 Background

In this chapter, the role of thermal fluctuations on the radiative rate in core/shell QDs will be explored. In the bulk, thermal fluctuations in the nuclear positions average over different configurations to create a density of states just below the band gap of the pure material, and presents as a sub-bandgap absorption feature.[84,85] Due to the smaller interaction energy between electron and hole in the bulk, this energetic feature can generally be described without the inclusion of electron-hole interactions. In nanoscale systems the electron-hole interaction is much stronger and must be included to accurately describe the energetics and rates in the system. It is therefore possible that similar thermal disorder on the nanoscale could impact the electron-hole interactions and therefore modify the TRPL.

In CdSe/CdS there is the additional complication of the core/shell interface. As described in Chapter 1, in CdSe/CdS QDs, the hole is localized to the CdSe core, but the electron is only weakly confined to the core, resulting in a radiative rate the varies with both core size and shell thickness.[31,45] Previous work on CdSe/CdS dot-in-rods have shown that the lifetime increases with temperature between 78 K and 300 K, and has suggested a changing, temperature-dependent conduction band offset could account for this effect.[86] However, the expected change in conduction band offset between core and shell over the temperature regime studied is on the order of 20 meV (using bulk parameters), which would be insufficient to describe the observed change in radiative rate, according to computational models.[87] Therefore, questions still remain on the mechanism of the observed change in radiative rate with temperature. Furthermore, the lack of computational support for the experimental measurements limits the conclusions than can be drawn, as a number of factors influence radiative recombination.

Development of a more complete understanding of the temperature-dependence of the radiative rate requires input from theory. This has proven challenging due to the requirement of modeling systems that consist of thousands of nuclei and electrons. So far, the effects of lattice fluctuations on the electronic properties of QDs have been limited to fairly small

Core diameter [nm]	Total diameter (error) [nm]	PLQY (error) at RT
3.4	7.5 (0.8)	0.76 (0.02)
3.4	9.7 (0.7)	0.84 (0.03)
3.4	12.5 (1.0)	0.89 (0.05)
4.9	9.7 (0.9)	0.52 (0.02)
4.9	10.9 (1.8)	0.60 (0.04)
4.9	13.1 (2.2)	0.58 (0.04)

Table 2.1: Sizes and PLQY of CdSe/CdS for TRPL studies

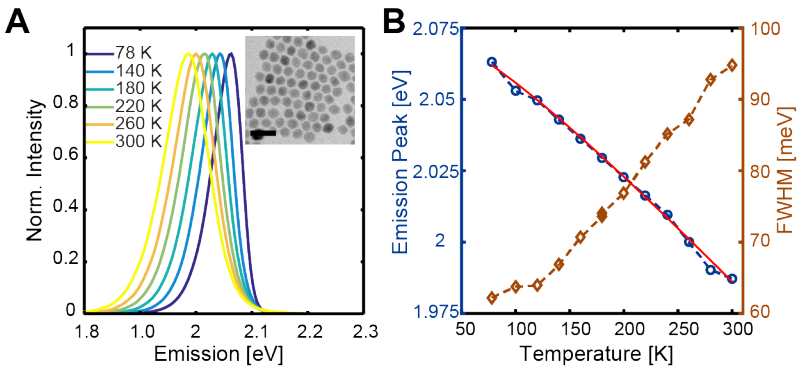

Figure 2.1: Sample temperature-dependent PL data. A selection of temperature-dependent PL data is shown for the 3.4 nm core, 9.7 nm total diameter QD. A) Shows the raw spectra (Inset: TEM micrograph, scale bar=20 nm) B) Shows the processed PL peak position and FWHM. The red fit line shows the Varshni fit for the PL peak position

systems.[88] An additional complication in determining changes in the radiative rate is that at non-cryogenic temperatures, it is often changes in the nonradiative rate that govern changes in the lifetime. The joint experimental and computational results presented in this chapter will give insight into the mechanism by which the radiative rate changes with temperature in CdSe/CdS QDs.

2.2 Synthesis and sample photoluminescence data

Wurtzite-CdSe/CdS core/shell QDs were synthesized using a modification of a literature preparation.[7] Two different sizes of CdSe cores were synthesized, and three different CdS shells were grown for each core size. The sizes and PLQY at room temperature (RT) are shown in Table 2.1. Computations were done on particles with sizes comparable to four of the six synthesized samples, on particles with 3 and 5 nm diameter cores and 9 and 12 nm total diameter for each core size.

$$E_G(T) = E_G(0) - \frac{\alpha T^2}{T + \beta} \tag{2.1}$$

Representative experimental PL data from 78 to 300 K are shown in Figure 2.1. The synthesized QDs are spherical, with a narrow size distribution as shown *via* the representative TEM micrograph in Figure 2.1A (inset). Furthermore, all samples have a high PLQY, which indicates that the recombination is dominated by radiative as opposed to nonradiative processes. PL spectra across the temperature range studied are shown in Figure 2.1A. As is expected for CdSe, there is a redshift of approximately 80 meV in the PL peak position from 78 K to 300 K, shown quantitatively in Figure 2.1B. The processed PL data can be fit using the Varshni Law, shown in Equation 2.1, an empirical relation that describes the change in semiconductor band gap with temperature. α is a measure of electron-phonon coupling and β is related to the Debye temperature. The fit shown in Figure 2.1B uses parameters $E_G(0) \sim 2.8$ [eV], $\alpha \sim 4 \times 10^{-4}$ $\left[\frac{\text{eV}}{\text{K}}\right]$, and $\beta \sim 110$ [K]. The α and β parameters are comparable to those of bulk CdSe, while the 0 K band gap, $E_G(0)$, is blue-shifted from the bulk value due to quantum confinement. Similarly, the full width at half maximum (FWHM) increases across the studied temperature range, as expected due to the effects of exciton-phonon coupling. The FWHM increase is in approximate agreement with previous studies, but is not fit here as the fit would be significantly over-parameterized.[86,89] In addition, as shown in the temperature-dependent PL spectra in Figure 2.1A, there is some asymmetry present in the PL peak, which is particularly observable at lower temperatures. This is likely due to reduced homogeneous (and therefore symmetric) broadening at lower temperatures. As a result, inhomogeneous broadening due to the presence of a size distribution is more evident at low temperatures. In general, the change in PL peak position as well as FWHM with temperature indicates that the PL originates from the CdSe core of the QD, consistent with previous measurements.[86,89]

Representative experimental TRPL spectra are shown in Figure 2.2. Notably, the lifetime increases with temperature for the CdSe/CdS QDs. In addition, it is possible to qualitatively observe that at higher temperatures, the TRPL decay appears increasingly non-monoexponential. This feature would be consistent with observations that reversible electron trapping behavior can result in delayed PL and a long-lived component in an otherwise monoexponential decay.[36,52] Since these QDs have a high PLQY, the increase in lifetime with temperature is due to a change in the radiative rate in the material. Temperature-dependent PLQY of the 3.4 nm core diameter samples shows that the PLQY is always higher at lower temperatures, and decreases between 10-20% as the temperature is increased to room temperature. One example of the temperature-dependent PLQY is shown in Figure 2.3. This suggests, that although there can be nonradiative recombination present, the observed change in lifetime is due to a change in the radiative rate of the material.

One assumption made is that within the temperature range studied, the exciton thermalization rate remains much faster than the radiative rate. Previous studies on carrier thermalization in CdSe/CdS dot-in-rods have shown that the hole relaxes to the band edge in less than 1 ps, which is much faster than the radiative rate.[90] Therefore, it is reasonable

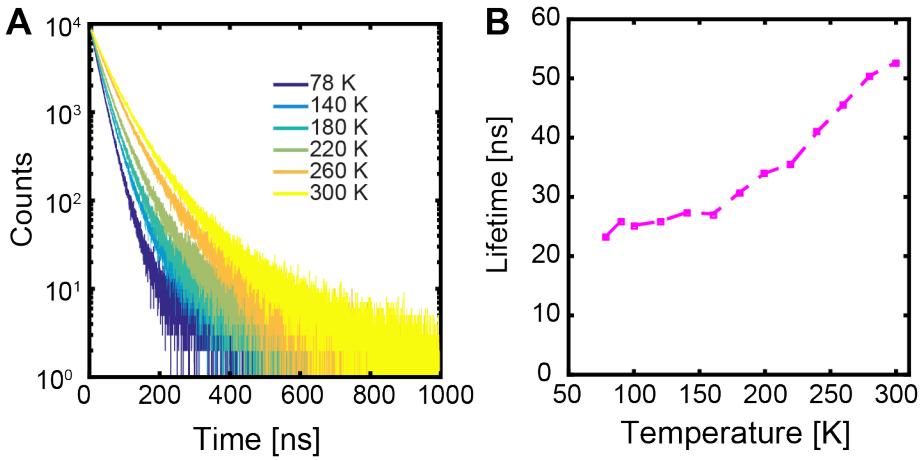

Figure 2.2: Sample temperature-dependent TRPL data. A section of the temperature-dependent TRPL data is shown for 3.4 nm core, 9.7 nm total diameter QD. A) Shows the raw spectra and B) shows the processed lifetime data using monoexponential fits to the first decade and a half of the decay.

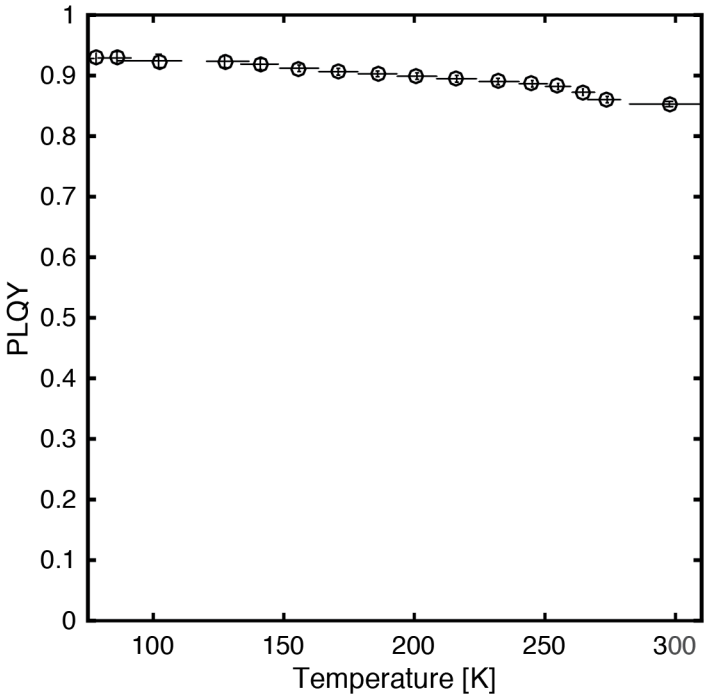

Figure 2.3: Temperature-dependent PLQY of the 3.4 nm core, 9.7 nm total diameter QD.

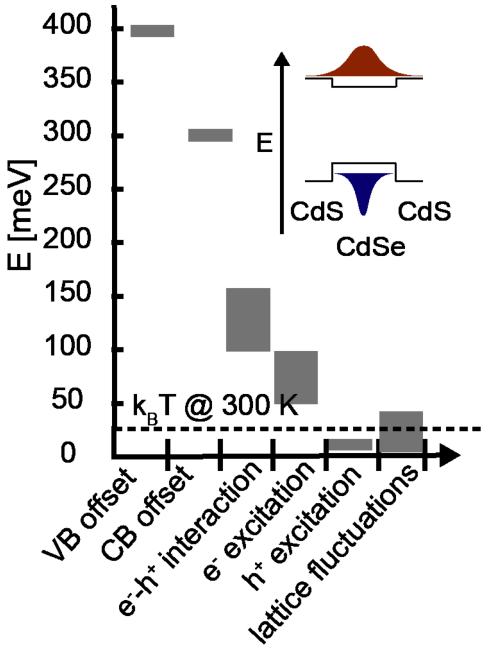

Figure 2.4: Energy scales relevant in CdSe/CdS QDs. The effects of the band edge offsets, the Coulomb interaction, higher energy electron and hole states, and lattice fluctuations are shown.

to assume that the exciton is in thermal equilibrium. Within this assumption, the presence of higher order electronic states would not change the observed monoexponential decay of the TRPL spectra.

Monoexponential fits to the first decade and a half of the TRPL data are shown in Figure 2.2B. While it would be possible to also use multi-exponential fits to better describe the higher temperature data, as this chapter primarily focuses on the more well-defined radiative recombination, this method was not used. To better understand the observed two-fold change in the radiative lifetime over the temperature regime studied, the relevant energy scales that dictate radiative recombination must be known.

2.3 Relevant energy scales

The energy scales in the system determine which fluctuations are relevant in dictating radiative behavior. For quantum confined systems, an understanding of the relevant energy scales is complicated by the additional strong electron-hole interaction. The energy scales for CdSe/CdS QD excitations are presented in Figure 2.4. The conduction and valence band offsets have previously been determined.[43] Although there is a 300 meV band offset in the conduction band, the kinetic energy of the electron is of the same scale, so the electron is not completely confined to the core (neglecting electron-hole interactions). The hole kinetic

energy is less than the electron kinetic energy due to its larger effective mass; this coupled with the large valence band offset effectively confines the hole to the core. Computations show that the electron-hole interaction is on the order of $\approx 100 \pm 50$ meV as shown in Figure 2.5, resulting in further confinement of the electron to the core. In addition to understanding the energy scales of the ground state exciton, it is also necessary to note the energy scales of higher excitations. Hole excitation takes < 10 meV of energy, while electron excitation is strongly dependent on the core and shell sizes of the CdSe/CdS, ranging from $50 - 120$ meV.

Lattice fluctuations (phonon modes) occupy a large energy range, but as a lower bound, confined acoustic phonons have energies on the order of 1 meV.[91] Optical phonons are expected to have excitations on the order of 10's of meV, and this would be the upper bound of the energy scales for lattice excitations. Therefore, at room temperature, the main thermally accessible excitations involve those accessed by hole excitation and lattice vibrations. In addition, electron excitation into the shell is also a possibility. As a result there are many potential causes that could change the radiative rate. For this reason, further discussion will primarily be focused on contributions to the change in radiative rate due to lattice fluctuations, with some discussion of the contribution from higher electronic excitations.

2.4 Comparison of the change in PL peak

As shown in Figure 2.1, thermal fluctuations can shift the CdSe PL peak by approximately 80 meV between 78 and 300 K. Using bulk parameters, the expected change in band gap due solely to thermal expansion of the lattice is only 8 meV; the other 90% of the observed change in band gap with temperature is due to coupling between electronic states and lattice fluctuations, consistent with the empirical parameters present in the Varshni fit. For this reason, before simulating the radiative lifetime at different temperatures, it is possible to assess the accuracy of the atomistic model by comparing the calculated and measured change in the band gap with temperature. Shown in Figure 2.5A-B is the experimentally observed change in PL peak with temperature. Figure 2.5C-D shows the the computations of the CdSe/CdS optical band gap for similar core and shell sizes. The resulting calculations, which match well to the experimental data, predict a change in the PL peak of approximately 100 meV, about 20 meV larger than experimental data. Similarly, the difference between theory and experiment in the absolute values of the band gap of the material is less than 20 meV for the small core samples.

For the large core samples, the deviation between the model and experiment is approximately 40-50 meV, slightly larger than the deviation for the small core samples. The experimental large core samples show almost no dependence of the PL peak on the shell thickness. As a larger core would result in both electron and hole being more confined to the core, and therefore less sensitive to shell thickness, this behavior is reasonable. However, the comparison between theory and experiment does not perfectly capture this behavior, suggesting that there is a scaling inconsistency. Indeed, for larger shell thicknesses the computations do show a saturation in the band gap as is observed experimentally in Figure 2.5B. The use

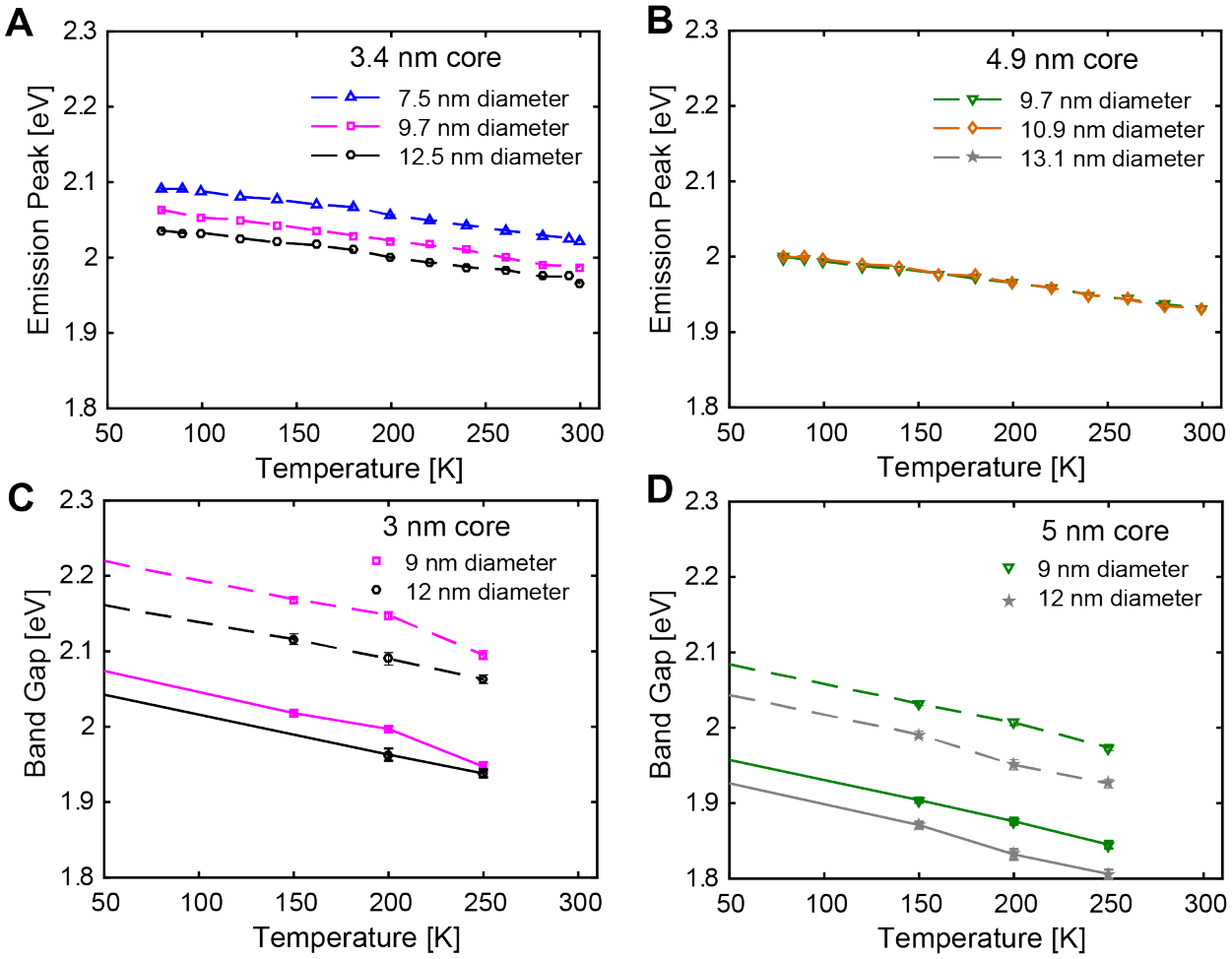

Figure 2.5: Change in PL with temperature. A) and B) show the change in PL peak with temperature for the 3.4 nm and 4.9 nm core diameter samples respectively. C) and D) show the computed change in band gap with temperature for the 3 nm and 5 nm core diameter QDs. The dashed lines represent the fundamental gap and the solid lines the exciton energy. Computational error bars arise from average over a number of nuclear configurations.

of a semi-empirical pseudopotential model for the electronic structures, the static screening approximation for the Bethe-Salpeter calculations, and the force-field approximation to simulate nuclear configurations could all introduce small errors in the observed measurements.

Despite the small differences described above, there is close correspondence between theory and experiment. A deviation of only 10's of meV between the electron structure computations and experiments can be considered sufficient to use this theory to further study the radiative rate. Additionally, the computations show that the exciton energy is about 100-150 meV lower than the fundamental gap, highlighting the importance of including the electron-hole interaction in QD systems, consistent with previous measurements.[43] The observed agreement between experiments and computations indicates that the simulations are accurate enough to proceed with more complex calculations of the radiative lifetime at different temperatures.

2.5 Understanding the change in radiative lifetime with temperature

Figure 2.6A-B shows the experimental dependence of the CdSe/CdS excited state lifetime on temperature. For all samples there is an increase in the lifetime with temperature. This feature is most prominent for the samples with thicker shells, and also more prominent for the 3.4 nm core. In order to understand the underlying causes of the observed change in radiative rate, the effects of both thermal population of excited states and thermal fluctuations in nuclear positions were simulated.

The effect of thermal population of higher energy excitonic states on the radiative lifetime is shown in the dotted lines for Figure 2.6C-D. It is clear that thermal population of higher energy states is insufficient to describe the observed change in lifetime, and only accounts for 20-30% of the observed experimental change. The effect of thermal population does, however, match the observed trends of smaller cores and larger shells having larger changes in radiative lifetime. The observed changes in lifetime due to thermal excitation can be understood as arising from differences in contributions from the hole and the electron to low-lying excited states. The primary contribution to these low-lying excitonic states results from hole excitation as described in Figure 2.7. However, as the hole is strongly confined to the core, the change in electron-hole overlap is likely small upon hole excitation. The smaller electronic contribution to this feature, however, also influences the observed trend with core size and shell thickness. The excited states corresponding to primarily electron excitation occur at lower excitation energies in the large shell particles, down to 50 meV for the 3 nm core, 12 nm total diameter QD. In addition, large shell particles are expected to have a larger density of shell states accessible to the electron. This combination of entropic and energetic effects would result in greater electron delocalization into a larger CdS shell. Furthermore, for a smaller CdSe core, the conduction band level would be elevated due to quantum confinement and thus reduce the energy for the electron to delocalize into the

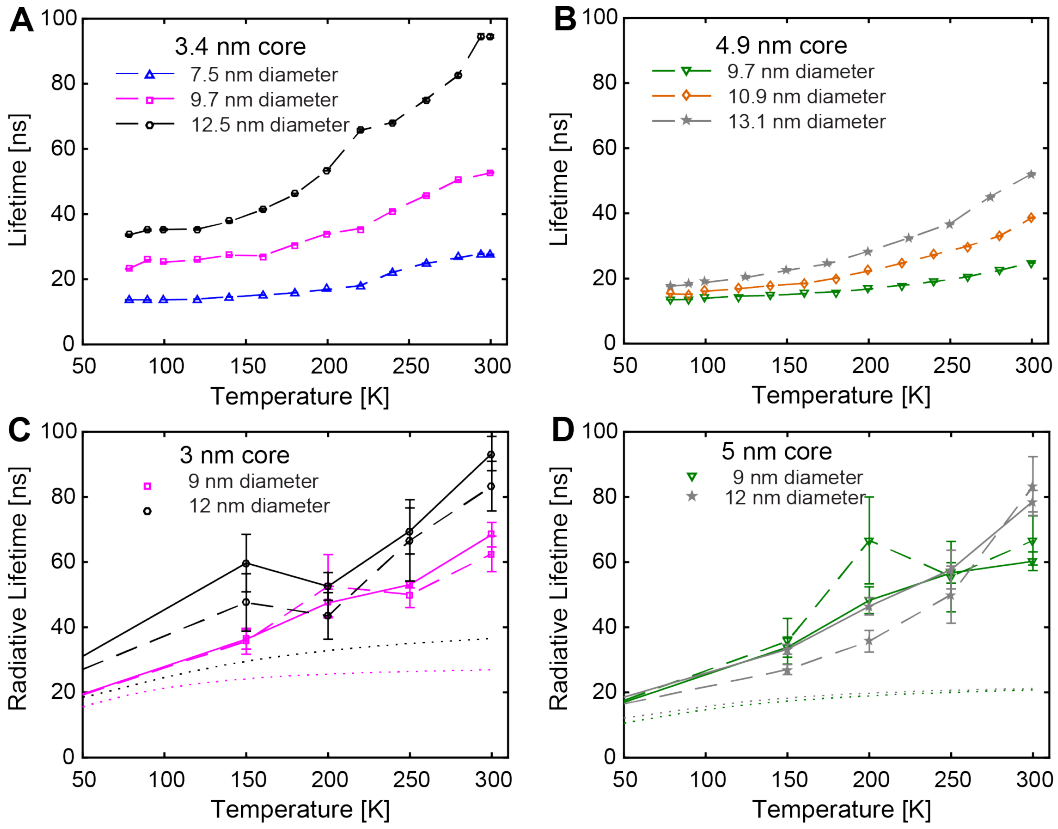

Figure 2.6: Change in lifetime with temperature. A-B) Change in the excited state lifetime with temperature for the 3.4 nm core (A) and 4.9 nm core (B) samples. C-D) Computational determination of the radiative rate for the 3 nm (C) core and 5 nm (D) core samples. The effects of thermal excitation (dotted), thermal fluctuations (dashed line), and both thermal excitation and fluctuations (solid line) are shown. Computational error bars arise from averaging over a number of nuclear configurations.

shell. The increased ability for the electron to delocalize into the CdS shell would result in an increase in the radiative lifetime, due to decreased electron-hole overlap. However, thermal population of higher excited states does not describe the scale of the observed change of lifetime with temperature.

In Figure 2.6C-D, the computed radiative lifetime as a function of temperature due to lattice fluctuations is shown (dashed lines). This is achieved by simulating a number of potential nuclear configurations and calculating the radiative lifetime from the excitonic state for each nuclear configuration. The values for each configuration at a given temperature are then averaged to compute the radiative lifetime as a function of temperature. The magnitude of the computed change in lifetime with temperature due to nuclear fluctuations is comparable to the experimental results. For the 3 nm diameter core, there is a clear difference in the room temperature lifetimes due to nuclear fluctuations of the 9 nm and 12 nm total

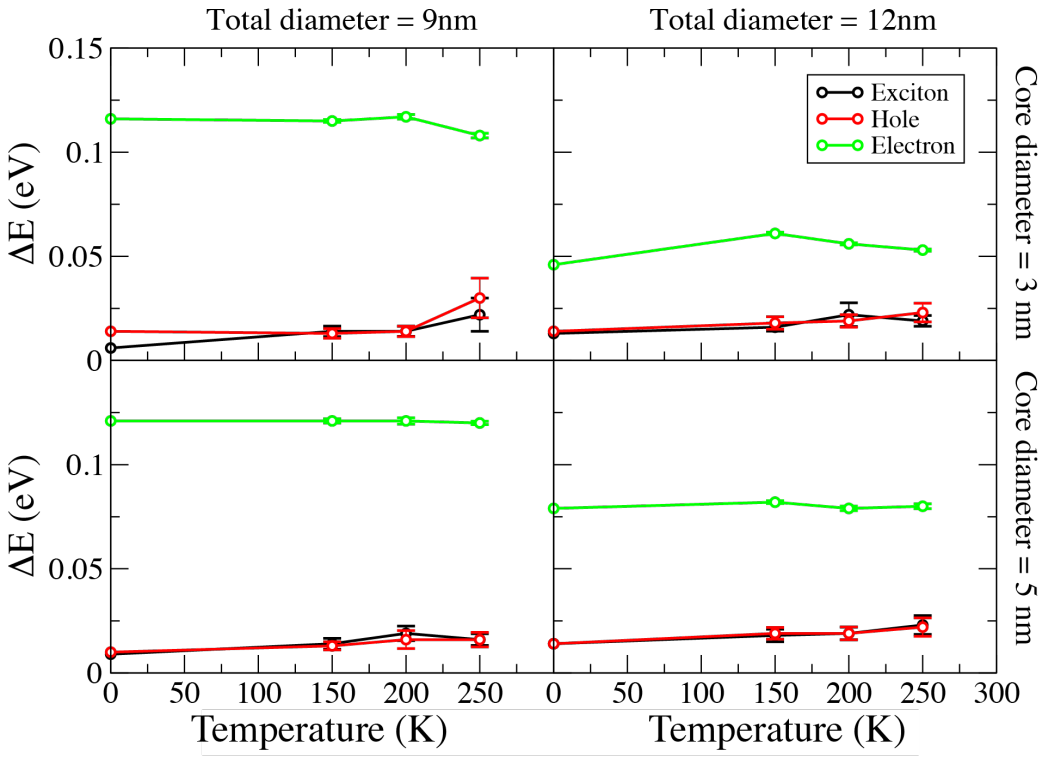

Figure 2.7: Low-lying excited states for the different samples. Computed energies of the first excited state of the exciton, the electron, and the hole for the four QD sizes.

diameter particle (Figure 2.6C), which matches well with the experimental data (Figure 2.6A). For the 5 nm core size, the difference in the calculated room temperature radiative lifetimes for the two total diameter sizes is within the statistical error of the calculations (Figure 2.6D). The reduced impact of shell thickness for the 5 nm cores suggest that the larger cores have less electron and hole density near the core/shell interface, which would reduce the influence the shell thickness has on the radiative lifetime. In addition, due to the small number of configurations used to determine the radiative lifetime (between 10 and 20), the results are somewhat noisy and show non-monotonic behavior in the dependence of the radiative lifetime with temperature. The inclusion of a greater number of nuclear configurations would reduce this feature.

The effect of both lattice fluctuations and thermal population of excited states in shown in Figure 2.6C-D (solid lines), and most accurately represents the experimental data. The radiative lifetime is computed by additionally averaging over thermally accessible excitonic states for each nuclear configuration. By including both the effects of thermal population of excited states and thermal fluctuations of the lattice, the observed trend with shell size is recovered for the 5 nm QDs. With the incorporation of both the effects of thermal excitations and nuclear fluctuations, the non-monotonic behavior discussed above is also

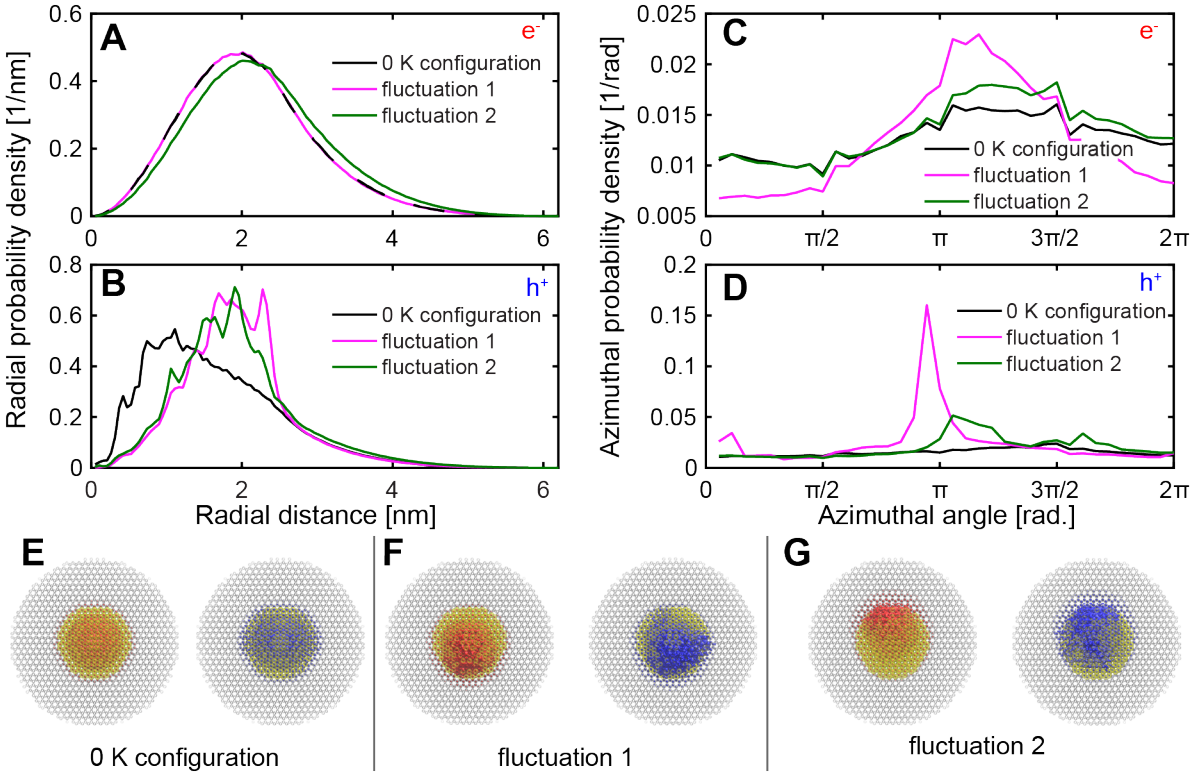

Figure 2.8: Change in electron and hole probability densities due to lattice fluctuations. Radial probability density for the electron (A) and hole (B) for the 5 nm core and 12 nm total diameter particle at 0 K and two sample configurations at 250 K. The azimuthal probability density computed over a shell of thickness 0.8 nm at the core/shell interface is shown for the electron (C) and hole (D). E-G show the probability densities for the electron (left,red) and hole (right,blue) for the same three sampled configurations. The yellow region corresponds to the CdSe core.

not as prominent. This suggests that although some local, transient excitonic trapping can occur, these events are rare and are averaged out.

The calculated and the experimental results show the greatest deviations at temperatures near room temperature; this is partially a result of the lower PLQY of the synthesized 4.9 nm core diameter samples, which would result in a shorter lifetime due to nonradiative quenching. Other sources of error could include to differences between the interfacial structure for the synthesized and modeled particles. Alloying during shell growth is expected in slow-injection shelling procedures,[31] but is not included in the computations.

To gain a better understanding of the impact of lattice fluctuations on the radiative lifetimes, the probability density for the electron and hole at 0 K and two sample configurations at 240 K are shown for the 5 nm core and 12 nm total diameter QD in Figure 2.8. Similar conclusions can be drawn from the other sizes of QDs that were computed. The radial prob-

ability densities are shown for both the electron (Figure 2.8A) and hole (Figure 2.8B). There are small differences between the 0 K and two sample fluctuations for both the electron and hole probability densities. There is a consistent delocalization of the electron into the shell in one sample fluctuation (magenta line) but less in the other sample fluctuation (green line), for which the radial electron density is nearly identical to the 0 K result. On the other hand, the hole localizes towards the interface between the core and shell in both sample fluctuations. The increased asymmetry in the hole angular distributions at 250 K (shown in Figure 2.8D) also suggests that the hole localize to small areas at the core/shell interface, which is not the case for the electron. The lack of asymmetry for the 0 K configurations also highlights the ability of the hole to localize at higher temperatures. The small increase in the electron asymmetry most evident in fluctuation 1 (magenta line) also indicates the hole localization can then drive the electron's behavior. This is supported by the electron and hole probability density maps, shown in Figure 2.8E-G. For the 0 K both electron and hole have symmetric probability densities that are primarily localized in the core. As the nuclear positions are allowed to fluctuate at higher temperatures, both electron and hole probability densities exhibit increased asymmetry and the hole begin to localize towards the core/shell interface. These results clearly show that the overlap between the electron and the hole is reduced when nuclear fluctuations are included since the degree of localization induced by lattice fluctuations is different for the electron and the hole.

2.6 Conclusions

The results presented highlight the importance of thermal fluctuations in determine excited state rates in QDs. In QDs, due to the strong electron-hole interactions, thermal fluctuations can change the radiative rate by a factor of three between 78 K and 300 K. We demonstrate that the inclusion of fluctuations at the atomic level is necessary in order to describe the temperature dependence of the radiative lifetime for QDs. Previous work has attempted to elucidate the source of the temperature dependence of the radiative lifetimes in nanostructured QDs[86,92] and in quantum wells,[93,94] but it is difficult to do so without a detailed theoretical model, which we have presented. We show that the presence of these nuclear fluctuations results in an electron-hole overlap strongly dependent on both core and shell dimensions, which suggests that temperature could have a significant effect on other rates for which the electron probability density is important, including Auger recombination processes. Additional features that would likely tune the magnitude of the observed effects include degree of alloying and the precise structure of the interface.

Chapter 3

Temperature-Dependent Structure of Mixed Ligand Shells

Reproduced in part with permission from: Arunima D. Balan, Jacob H. Olshansky, Yonatan Horowitz, Hui-Ling Han, Erin A. O'Brien, Lucio Tang, Gabor A. Somorjai, and A. Paul Alivisatos. "Unsaturated Ligands Seed an Order to Disorder Transition in Mixed Ligand Shells of CdSe/CdS Quantum Dots" *ACS Nano*, submitted for publication.

3.1 Background

Control over the structure of the ligand shell is essential in tuning interactions between QDs,[64] solubility of QDs in organic solvents,[60,95,96] and the structure of assemblies of QDs.[59,70,71] A phase transition within the ligand shell of QDs is shown schematically in Figure 3.1 and strongly impacts the above properties. Previous computational studies have explored the role of surface coverage and particle curvature in modifying the phase transition temperature.[65] Several experimental studies have also shown how such phase transitions depend on the ligand chain length.[63,95] However, studies are lacking on the effects of mixed ligand shells on the phase transition behavior, likely due to the added complication of quantifying the ligand shell composition. In particular, this chapter focuses on the study of mixed ligand shells of octadecylphosphonic acid (ODPA) and oleic acid (OA), both bound in the singly deprotonated form. The role of ligand chain length and binding group head is also addressed in this chapter.

One benefit of using CdSe/CdS QDs to study the structure of the ligand shell is that previous work has suggested that the PLQY is sensitive to the structure of the ligand shell, which provides a handle to determine the conformation of the ligand shell. Previous work has shown that when the ligand shell undergoes an order/disorder system, the PLQY of the system increases. This has been observed in CdSe QDs capped with amines,[63] in water-soluble CdTe QDs,[97] and in CdSe/ZnS core/shell QDs.[98] The observed increase in PLQY, which previous studies have suggested corresponds to a decrease in the nonradiative rate,[63] is likely due to a decrease in charge trapping when the ligands disorder. While the precise nature of this trap state is unknown, the presence of such a trap in the ordered, low-temperature, ligand shell structure is consistent with the strong influence that surface ligands can have on QD PLQY. For example, even subtle changes in the surface dipole moment based of

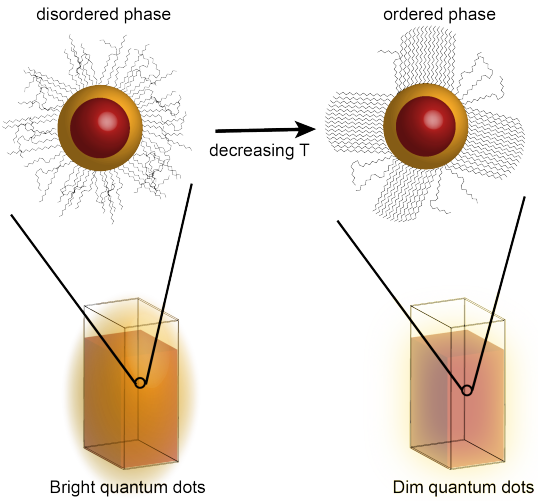

Figure 3.1: Schematic of an order/disorder transfer within the ligand shell

the orientation of ligands at the surface of the QD have been shown to shift the band edge positions of QDs.[99] Despite this uncertainty in the nature of the trap state, the PLQY can still be used as a probe for the structure of the ligand shell. In order to get a more molecular understanding of the phase transition, IR and SFG spectroscopies were also performed, and a lattice model was developed to understand the behavior of this system.

3.2 QD synthesis and surface characterization

As previous work has observed the ligand phase transition via optical properties in CdSe QDs, a similar system, CdSe/CdS core/shell QDs, was used here.[63] The addition of a thin CdS shell serves multiple purposes. First of all, the CdS shell significantly increases the PLQY of the QDs, such that it is possible to more accurately determine changes in lifetime and PLQY. Additionally, the high-quality wurtzite CdSe cores used here are synthesized with only ODPA ligands bound to the surface of the QD.[50] Due to the difficulty of performing ligand exchange from phosphonates, it is useful to introduce other ligands into the shell. This can be done using a modification of a literature procedure for the synthesis of CdSe/CdS QDs. The shelling reaction proceeds through the slow-addition of Cd-oleate and octanethiol.[7] As a result, after the shelling procedure the only two ligands that are present on the surface are OA and ODPA.

To interrogate the role of ligand composition on a phase transition within the ligand shell, it is necessary to both tune and to quantify the composition of the ligand shell. Ligand exchanges on the QDs were performed through the sub-stoichiometric addition of ODPA in tetrahydrofuran (THF), as ODPA has limited solubility in other solvents. A 1:1 ligand exchange was assumed during this process, as previous studies have shown that ODPA

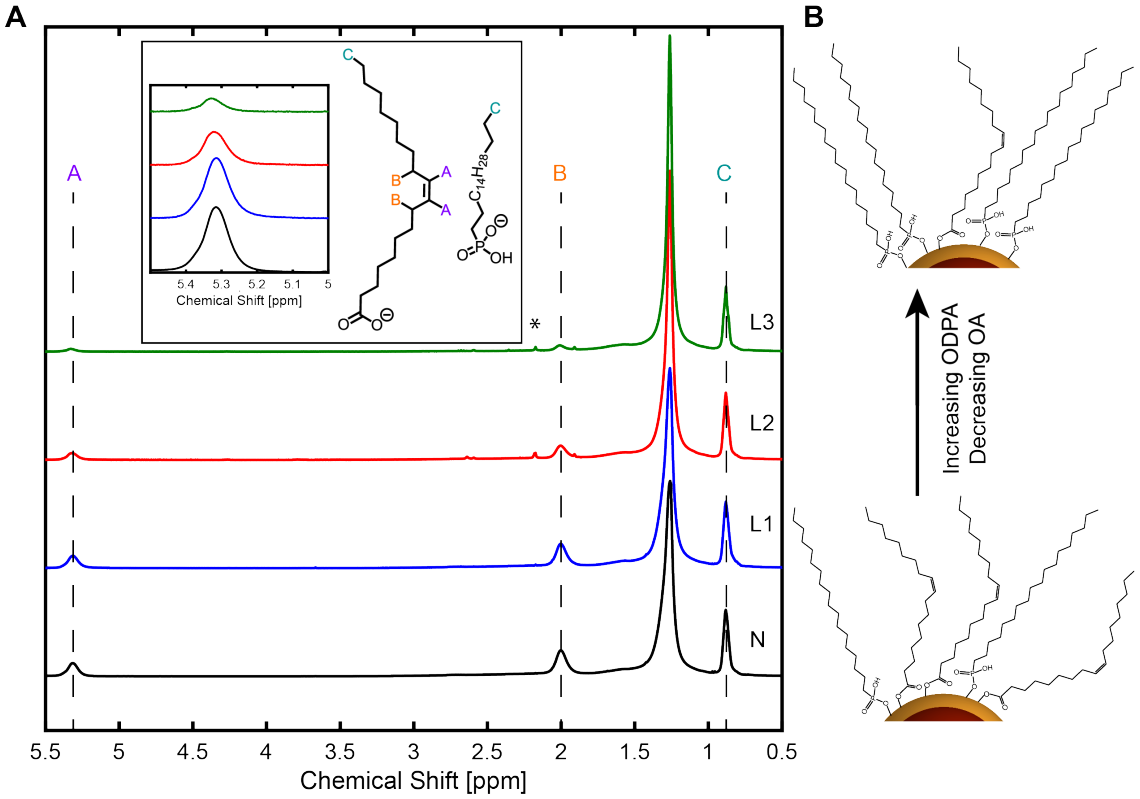

Figure 3.2: Ligand exchange to ODPA and NMR quantification. A) Quantitative proton NMR of native (N) and ligand-exchanged (L1-L3) samples. The inset shows the decrease in the vinyl peak as the ligand exchange proceeds, and associated NMR peaks for the ligands used. B) Schematic of the ligand exchange process, during which OA is replaced with ODPA.

primarily binds in its mono-deprotonated form.[50] The ligand exchange that was performed is shown schematically in Figure 3.2B. Upon exchange, QDs are precipitated with antisolvent (acetone) at least two times in order to remove free ligands. Proton NMR of the cleaned samples is used to determine the ligand composition on the surface. Shown in Figure 3.2A are the proton NMR spectra for all samples. NMR was performed at high concentrations, of around 20-90 mM in ligand, and around 10-50 μM in QDs, to ensure minimal Z-type (Cd-ODPA or Cd-oleate complexes) desorption of ligands. The NMR peaks of ligands bound to QDs are characteristically broadened,[18,35,50] and the absence of sharp peaks indicates all ligands are bound to the QD surface. The peaks corresponding to the OA vinyl protons (A), protons on the carbon adjacent to the alkene, (B), and the methyl protons of both OA and ODPA (C) are distinct, and are labeled in Figure 3.2. The other aliphatic protons are in the large unlabeled peak around 1.2 ppm. Notably, the protons on the alpha carbon of OA are difficult to observe in the NMR spectra, likely due to increased broadening because of their

sample	percent OA (error)	percent ODPA (error)	normalized coverage
N	64(3)	36(3)	1
L1	55(3)	45(3)	.95
L2	34(2)	66(2)	.95
L3	16(1)	84(1)	.77

Table 3.1: NMR quantification of ligand binding

proximity to the QD surface.

NMR spectra for these QD samples are normalized using an external standard of ferrocene in toluene-d_8 and the optical density of the QD solution. The extent of the ligand exchange is monitored through the decrease in the vinyl peak (A) as the ligand proceeds, highlighted in the inset of Figure 3.2. The composition of ligands on the surface is quantified by taking a ratio of peak A to C, normalized by the number of protons per each functional group (2 for peak A, 3 for peak C). Furthermore, any change in the area of peak C is related to a small stripping of the surface ligand coverage. The data on ligand composition and total surface coverage are shown in Table 3.1. As the error on the ligand coverage encompasses error from the external NMR standard, the NMR measurement itself, and error from the absorption measurement, it is likely rather large, but the coverage is still a useful metric. Across all ligand-exchanged samples, we observe a small decrease in total ligand coverage compared to sample N. However, the bulk of the decrease in surface coverage can be attributed to sample L3. One possibility is that during the ligand exchange and subsequent purification process, trace water or other protic solvents could result in stripping of ligands from the QD surface, which has previously been shown for both CdSe and PbSe QDs.[53] Additionally, as the phosphonate head group is larger than the carboxylate it is also possible that fewer phosphonates can fit onto the surface of the QD. Despite the deviation in the surface coverage measurements, it is clear that the surface composition can be tuned and quantified using this method.

3.3 Temperature-dependent photoluminescence measurements

Temperature-dependent PL measurements were done in order to observe the phase transition. While the mechanism by which a change in the ligand shell conformation can modify the optical properties is not intuitive, it has been observed several time previously in QD systems.[63,98] Previous work on CdSe[63] and CdSe/ZnS[98] QDs have shown that when the temperature of the system increases, the ligands disorder and there is a resulting increase in PLQY. Furthermore it is possible to obtain highly precise temperature-dependent photoluminescence spectra, so this technique is useful to better better map out the phase transition. As the sensitivity of the PL is due to a trap state, the likely root of this is an increase in the

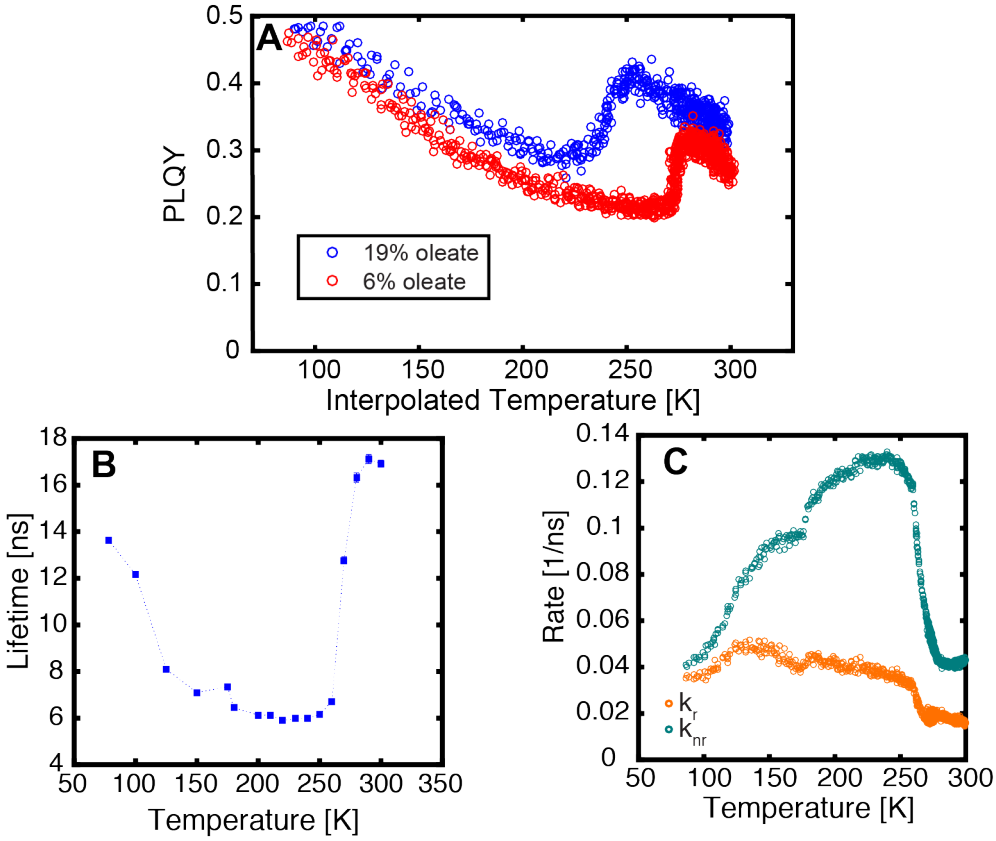

Figure 3.3: Observing the ligand phase transition through PLQY and TRPL for a different QD sample. A) Temperature-dependent PLQY for two ligand compositions, using a Varshni calibration to the emission peak. B) Temperature-dependent TRPL for the 6% ODPA composition, C) radiative (k_r) and nonradiative (k_{nr}) rates for the 6% ODPA sample using data from A and B.

nonradiative rate, k_{nr}, when the ligands are ordered. There are two ways to observe a change in k_{nr}: *via* TRPL or PLQY. The comparison of observing the ligand phase transition through both TRPL and PLQY is shown for a different QD sample in Figure 3.3 and demonstrates that both techniques provide similar information and together confirm that the k_{nr} is indeed the changing parameter. The small change in k_r around the phase transition temperature (approximately 260 K) observed in Figure 3.3C is likely due to small errors in interpolating the change in lifetime or in calibrating the temperature for the PLQY measurements.

For the subsequent studies, PLQY is chosen here as a more effective way of interrogating changes in the ligand shell. This is partially due to the previous findings described in Chapter 2. As k_r also changes with temperature, a difference in the excited state lifetime could be attributed to either k_r or k_{nr}. While this is perhaps not as much of an issue due to the fact that the samples here have thinner shells, if the phase transition is weak, it could be

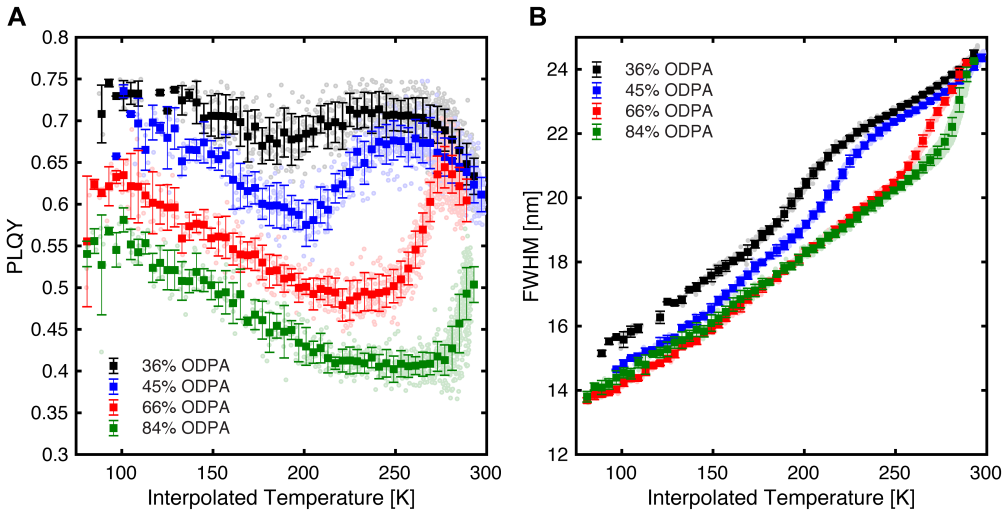

Figure 3.4: Temperature-dependent PL of ligand-exchanged QDs. The temperature dependent PLQY (A) and FWHM (B) for the four ligand compositions are shown as a function of temperature.

difficult to deconvolute these two effects. Additionally, the integrating-sphere temperature-dependent PLQY measurements described previously produce significantly more data in a shorter time, allowing for better statistics and analysis.

Shown in Figure 3.4 is the temperature-dependent PL data performed on the sample described in Table 3.1 and Figure 3.2. In addition to the Varshni calibration to the emission peak, due to some non-monotonic behavior around the phase transition temperature, a Newton's law of cooling calibration method is used only for this sample, and is further described in Appendix B. In all samples there is a region during which the PLQY increases with temperature (Figure 3.4A). This phase transition region increases in temperature and narrows as the amount of ODPA in the ligand shell is increased. This suggests that the the observed behavior is being driven by a change in the ODPA.

There is also a corresponding change in the FWHM, as shown in Figure 3.4B. In both bulk semiconductors and in nanocrystalline CdSe/CdS the FWHM tends to increase with temperature, due to the presence of electron-phonon coupling.[82,86] The relation between FWHM and temperature is complex, as a number of phonon modes with different densities of state exist, but typically the FWHM increases smoothly with temperature, as observed in Figure 2.1B. The data in Figure 3.4B show a jump in FWHM, that is not smoothly increasing, and furthermore changes in position as the composition of the ligand shell changes, just like the PLQY data. This suggests that the underlying ligand phase transition can impact both the FWHM and the PLQY. While the PL properties are useful in providing insight into this phase transition, it is difficult to gain a molecular picture using the optical data. To gain a more molecular understanding of the phase transition, IR spectroscopy of the C-H region is used.

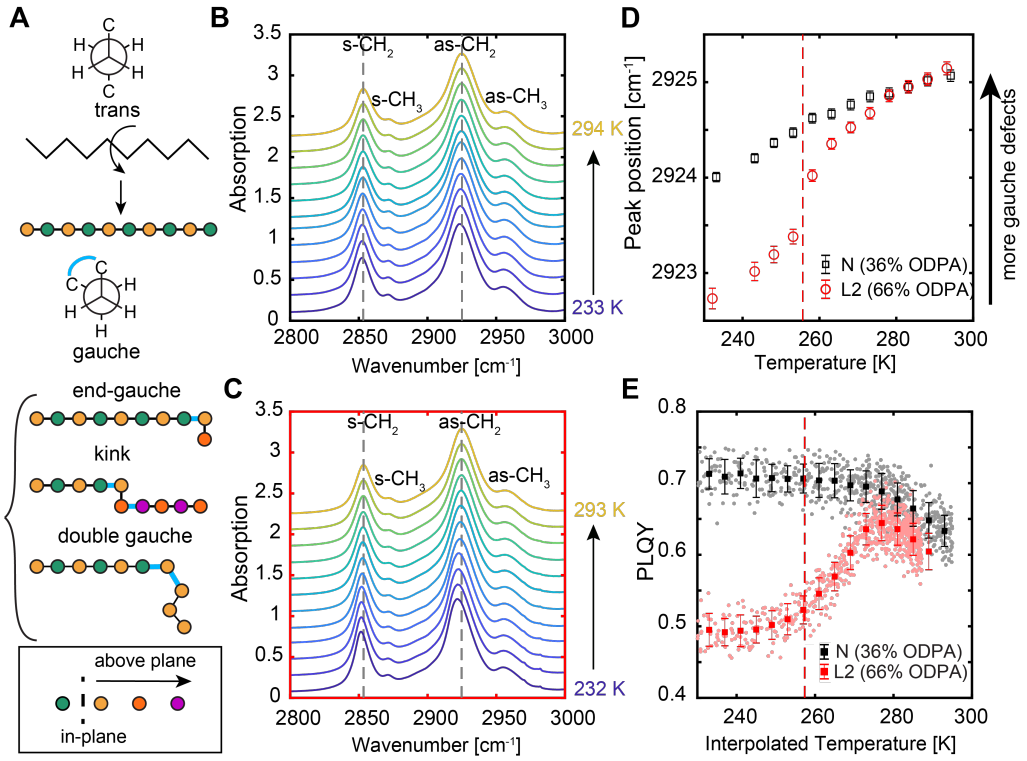

Figure 3.5: VT-FTIR data of two ligand compositions. A) shows common *gauche* defects that would cause the ligand chains to disorder at the studied temperatures. The FTIR data in the C-H stretching region is shown for samples N (B) and L2 (C). In addition, the variation with temperature of the as-CH_2 stretch is shown in D, and compared with the observed change in PLQY (E) from Figure 3.4

3.4 Temperature-dependent IR spectroscopies

Variable-temperature fourier transform infrared spectroscopy (VT-FTIR) measurements were performed on two samples, N (36% ODPA) and L2 (66% ODPA). These measurements were performed in solution in $CDCl_3$ to minimize overlap of the solvent and C-H stretching modes, while ensuring QD solubility. $CDCl_3$ is convenient as it was the solvent for the NMR spectra, and VT-FTIR measurements were performed at similar concentrations as the NMR experiments. This ensures that all ligand signatures observed in the VT-FTIR measurements arise from ligands that are bound to the QD surface, not free in solution, which allows the methylene stretching frequencies to be used to determine qualitative information about the conformation of the QD ligands. A portion of the C-H stretching region is shown in Figure 3.5B-C, for both samples N and L2. There are four main peaks present within this range: the symmetric methylene stretch (s-CH_2), symmetric methyl stretch (s-CH_3), antisymmetric methylene stretch (as-CH_2), and the antisymmetric methyl stretch (as-CH_3). In addition,

the vinyl C-H stretch decreases in relative intensity from sample N to L2, further confirming the ligand exchange shown by the NMR data.

Small shifts are observed in the (s-CH_2) and (as-CH_2) stretching frequencies with temperature that give insights into the structural conformation of the aliphatic ligand chains. An increase in stretching frequency corresponds to an increase in the number of *gauche* configurations present in the methylene chain.[100] Figure 3.5A shows the most common *gauche* defects at these temperatures.[100] The all *trans* configuration has a planar carbon backbone, which would allow for efficient packing of the aliphatic chains. The *gauche* defects disrupt the otherwise planar carbon backbone, and would serve to disorder the ligand shell. This is shown in Figure 3.5D, where the as-CH_2 stretch frequency is shown for both sample N and L2. Both samples show a gradual decrease in the as-CH_2 stretch frequency as the temperature decreases. At just below the PL-observed phase transition temperature for L2, there is a sharp decrease in the as-CH_2 stretching frequency for L2, but not for N. Unfortunately, due to temperature limitations because of the chloroform freezing point and a decrease in QD solubility at low temperatures, signatures of the phase transition for sample N through VT-FTIR were not captured. However, the observed change in as-CH_2 for sample L2 highlights that the phase transition observed using PL is related to a change in packing of the aliphatic chains. Furthermore, we observe a similar transition in the s-CH_2 frequency, but the frequency change for the s-CH_2 stretch is smaller.

The observed magnitude of change for both methylene stretching frequencies is significantly smaller than previous observations of self-assembled monolayers on both planar substrates[101] and on 2-3 nm diameter octadecanethiolate capped Au nanoparticles.[102] Additionally, we observe a higher methylene stretch frequency in the low temperature phase than in the aforementioned other systems. This suggests that the low-temperature, ordered phase in the CdSe/CdS system has more disorder present than in the Au-thiolate system. One possibility is that the small particle size, which results in variable faceting present in these particles reduces the ordering through an increase in chain defects at the facet edges, as has been observed previously in platelet systems,[103] and has similarly been shown to be more prominent for smaller diameter QDs.[65] Additionally, the Cd sub-lattice spacing is further apart than the Au spacing or that of elemental semiconductors. This would reduce the strength of the inter-ligand interactions and result in a weaker phase transition, as is observed here. To gain more detailed information on the degree of order during this phase transition, temperature-dependent SFG spectroscopy is utilized.

SFG measurements were performed with QDs spun-cast onto a quartz substrate and then immersed in hexanes to ensure that ligand solvation would remain relatively consistent between the PL, FTIR, and SFG experiments. Since SFG is particularly sensitive to order at interfaces, it is an effective way to probe the ligand surface structure. The characteristic vibrations of both the phosphonic and carboxylic acid head groups attaching the ligands to the QD surface were beyond the SFG spectral range. However, the aliphatic tail structure was within the spectral range, which enables study of the aliphatic chain conformation and order. Similar to the VT-FTIR measurements the s-CH_2, s-CH_3, and as-CH_2 are seen. The as-CH_3 is also present, but is hidden behind other resonances present. In SFG, the Fermi

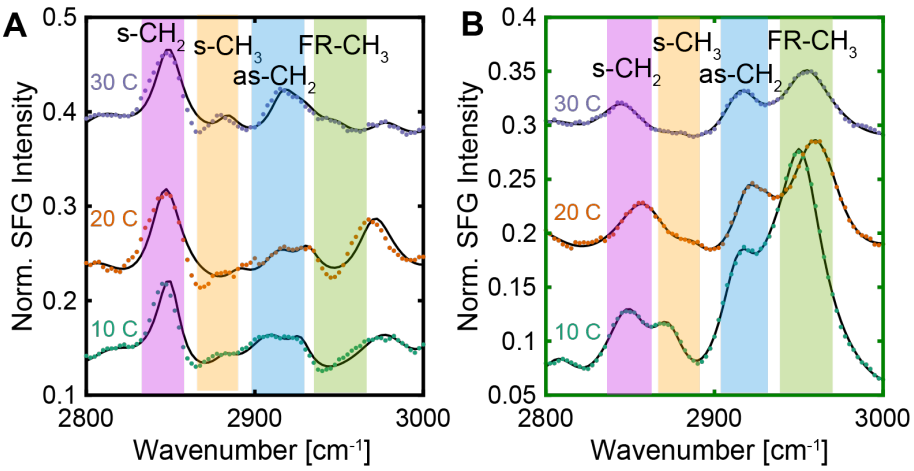

Figure 3.6: Temperature-dependent SFG spectra of samples N (A) and L3 (B) are shown. Important SFG peaks are highlighted in the figure.

resonance of the methylene and methyl groups, which shift their energies and intensities due to coupling to other modes can be observed as well. As the ordered ligands are likely to stand somewhat perpendicular to the QD surface, the laser beams were polarized to an *SSP* combination.

The ratio between the s-CH_3 (highlighted in purple in Figure 3.6) and s-CH_2 (highlighted in orange in Figure 3.6) stretches is diagnostic of the degree of order in the ligand monolayer. More order results in a higher ratio of s-CH_3 to s-CH_2 peak intensities, as the s-CH_2 are in a centrosymmetric, therefore SFG inactive, environment when the chains are ordered. By comparing the temperature-dependent SFG spectra formed on samples N (36% ODPA) and L3 (84% ODPA), information about the ordering of the ligand shell can be obtained. For sample N, shown in Figure 3.6A, there is no significant change in the SFG, both in lineshape and peak intensity, over the observed temperature range. The ratio of methyl to methylene stretch is about 1:10, as shown in Figure 3.7, which suggests a disordered ligand shell. This data is in agreement with both the PL (Figure 3.4) and the FTIR data (Figure 3.5), as both suggest that the change in the ligand tail structure would occur at lower temperature than those accessible by the SFG experiments. On the other hand, the SFG of sample L3 (84% ODPA) shows a change in the spectral shape, in particular between 10 ^{o}C and 20 ^{o}C , the same temperature regime in which a phase transition is observed using PL (Figure 3.4). In particular, there is a significant decrease in the s-CH_3 as the temperature increases from 10 to 30 ^{o}C, indicative of disordering of the ligand shell. This suggests a somewhat ordered configuration at 10 ^{o}C, as equal methylene and methyl amplitudes is consistent with approximately one *gauche* defect per aliphatic chain (excluding the OA *cis* double bond).[103,104] In fact the 30 ^{o}C SFG spectra of both samples N and L3 are quite similar, suggesting that at this temperature the ligand shell structure is similar for both

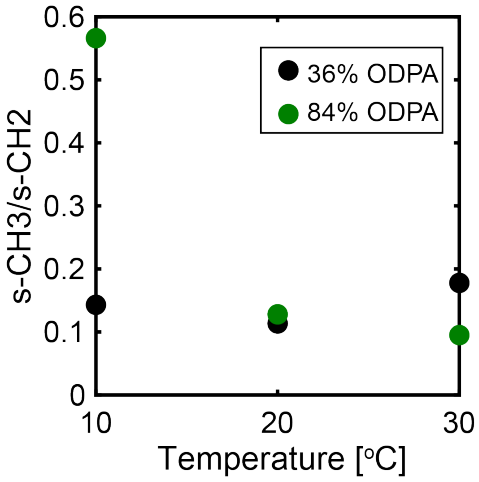

Figure 3.7: Comparison of s-CH_3/s-CH_2 ratio. Using SFG fits shown in Figure 3.6, the s-CH_3/s-CH_2 ratio is shown for the two samples studied.

samples. The s-CH_3/s-CH_2 ratio is a useful parameter that describes the degree of order in the aliphatic chain. It further confirms that there is a phase transition with sample L3 and not in sample N around 10-20 ^{o}C. This ratio is shown in Figure 3.7.

In addition to the symmetric stretches, analysis of the CH_3 Fermi resonance (FR-CH_3) and the as-CH_2 can give more information about the structure of the ligand shell. Qualitatively, there is a significant difference in this region between sample N and sample L3. In particular, for sample L3 (84% ODPA) there is a clear increase in the FR-CH_3 at 10 ^{o}C compared to all temperatures for sample N and other temperature for sample L3. An increase in the relative intensity of a Fermi resonance is due to a higher degree of similarity between the two modes. For example, tighter packing of neighboring ODPA, specifically their aliphatic tails, can induce their tails to stretch to their full (all *trans*) length. This in turn can give rise to coupling between a fundamental vibration and the overtone of another vibration (e.g., a C-H stretching mode coupled with a deformation mode). This relation between the s-CH_2 and as-CH_2 can also yield information about the tilt angle of the aliphatic chains, but for these samples no significant trend can be discerned. This is potentially due to the isotropic arrangement of ligands, which inhibits such an analysis. However, in total, the SFG data complements the structure we received from the VT-FTIR analysis: an increase in *gauche* defects in the aliphatic chains consistent with an order/disorder type of phase transition occurs at similar temperatures as the transition in PL.

3.5 Composition-dependent behavior

The FTIR and SFG spectroscopies show a clear correlation between the change in the PL of the QDs and the structure of the ligand shell. Due to the large change and higher

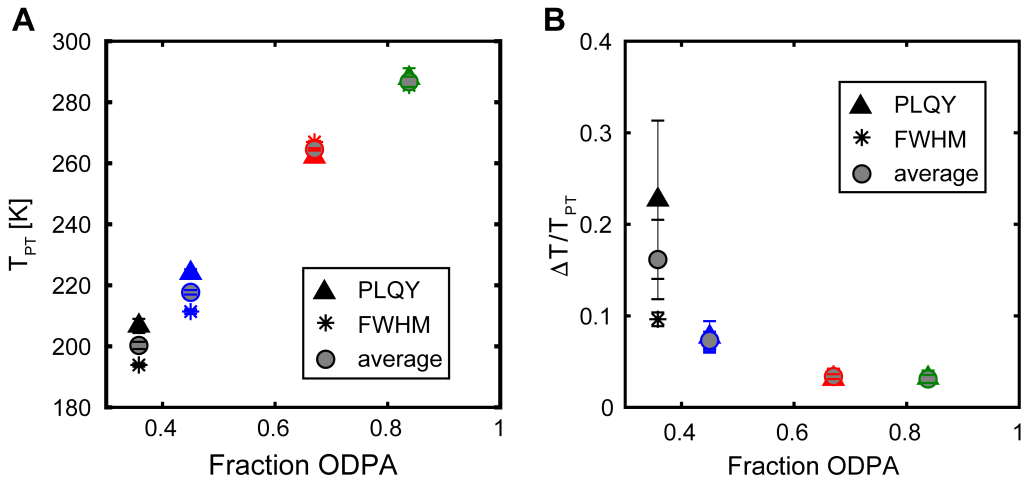

Figure 3.8: Phase transition temperature and width. The phase transition temperature (A) and width (B) are determined for the four ligand compositions using Equation 3.1

temperature resolution of the PL properties, we can treat both the PLQY and the FWHM as order parameters that give insight to the extent of the phase transition. In order to better analyze the phase transition temperature and the associated transition width, both the PLQY and FWHM data are fit to the integral of the Cauchy distribution superimposed on a linear change in temperature as shown in Equation 3.1.

$$O(T) = O_o + bT + c\tanh\left(\frac{T - T_{PT}}{\Delta T}\right) \tag{3.1}$$

$O_o + bT$ approximates the change in PLQY and FWHM with temperature excluding the phase transition, which are expected to have more complicated functional forms.[82,86] The parameters c, T_{PT}, and ΔT refer to the strength of the transition, the phase transition temperature, and the width of the phase transition, respectively. Although the use of the integral of the Cauchy distribution to approximate the observed finite phase transition is somewhat arbitrary, it is not obvious which functional form to use, and similar distribution are likely to fit and yield similar information. To confirm the accuracy of this fitting method, a numerical derivative was also performed to determine the phase transition temperature. The numerical derivative method results in significant error if there is any noise in the underlying data. Additionally, the (additive) error bars for this analysis method are extremely large and are not shown in Figure 3.9. Despite these pitfalls it possible to perform this analysis to determine the phase transition temperature, as is shown in Figure 3.9, and the two data analysis methods show reasonable agreement. This analysis suggests that fits to Equation 3.1 will give reasonable information about the phase transition.

The fitted phase transition temperatures and widths are shown in Figure 3.8 as a function of ligand shell composition. The phase transition temperature increases and the phase transition width decreases with increasing ODPA composition. There is quite a significant change

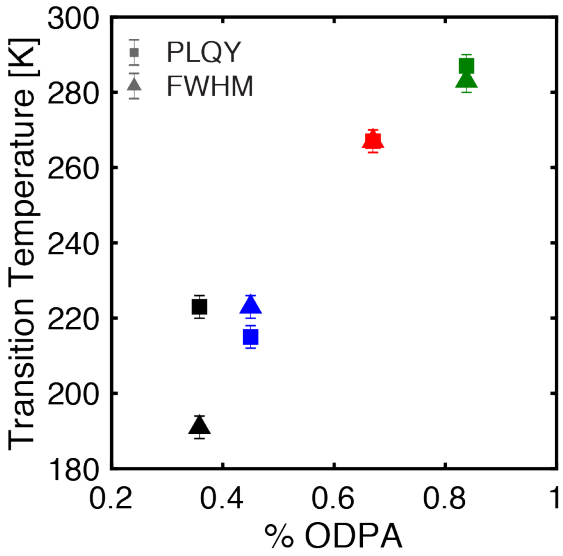

Figure 3.9: Phase transition temperature using the numerical derivative. The phase transition temperature is shown determined using the maximum of the numerical derivative for the binned PLQY and FWHM data.

in both parameters over the samples studied. The phase transition temperature changes by almost 90 K, while the phase transition width changes by about a factor of three. The PLQY and FWHM data match quite well, but there is a significant deviation for sample N. Sample N has the least amount of ODPA and, correspondingly, the smallest change in PLQY. This results in significant error in the PLQY-derived phase transition width, primarily. However, the FWHM data for sample N shows no more error than for the ligand-exchanged samples.

While the data in the above sections indicates that the observed phase transition is driven by the ODPA chains packing, the precise role by which OA facilitates disordering of the ODPA chains is unclear. One possibility is that OA plays a minimal role in changing the phase transition. Rather, what dictates the phase transition behavior is the total number of ODPA present in the system, N_{ODPA}. It is well-established that for first order phase transitions decreasing the size of the system (number of molecules involved) will result in a decrease in the phase transition temperature and a broadening of the phase transition.[105,106] However, the large change in the phase transition temperature observed here is inconsistent with previous observations in other finite-size systems. For example, in the Au-dodecanethiolate system a change in the number of surface ligands by about a factor of four results in only a 15 K decrease in the phase transition temperature.[107] Similar analysis of ODPA on CdS shows a decrease of approximately 40 K for around a 13-fold change in particle surface area, mainly attributed to an increased surface curvature.[65] This suggests that the OA chains are playing a more active role in disrupting the ODPA chain packing.

3.6 Ising model with induced disorder

To better explain the observed transition, we can use a simple model that describes the interactions between ODPA and OA chains in both the disordered and ordered states. While complex molecular dynamics simulations are able to most accurately describe the true behavior of such systems, somewhat simplified models are of use in providing a qualitative understanding. The phase transition observed here is similar to the gel-to-liquid transition present in phospholipid bilayers. This gel-to-liquid transition can be mapped onto the Ising model with a trigonal lattice, where spin-up is the ordered phase, and spin-down is the disordered phase.[108,109] We can use the parameters of the gel-to-fluid transition to instead approximate the phase transition in the ligand shell of the QDs. In the simplest case, the model assumes an energy difference, ε, between the ordered and disordered phases. There is a coupling term, W, that accounts for favorable inter-chain coupling only when both chains are ordered. Coupling between two disordered chains or between one ordered and disordered change is approximated as zero. Finally, there is an associated entropy of the disordered state, S, that can then be mapped to a temperature-dependent field. In the model used here, we assume a square lattice both for simplicity and because the Cd sublattice geometry is different on the various w-CdS facets likely present in the QDs. This is sufficient to describe the order/disorder transition within a ligand shell composed entirely of ODPA ligands and these parameters are shown schematically in Figure 3.10. In order to simulate the presence of OA within the ligand shell, a given fraction of fixed disorder phase ligands are introduced randomly within the simulations. This is a reasonable approximation because OA cannot order in an all *trans* configuration due to the *cis* double bond between carbons 9 and 10.

The three parameters involved in this simulation and inter-related and likely different combinations of these parameters could result in similar model outcomes. By mapping the parameters of the ligand transition system onto the Ising model, we can determine the expected phase transition temperature for the 100% ODPA sample, as is shown in Equation 3.2. From this, we can see that increasing ε and W would increase the phase transition temperature. Similarly, the S of the disordered state can have a significant impact on the phase transition temperature, with increasing S decreasing the phase transition temperature. However, the only parameter which would change the strength of the intermolecular interactions is W. For this work, the S was held fixed, and ε and W were optimized to better fit the experimental results.

$$T_{PT} = \frac{\varepsilon + 2W}{S} \tag{3.2}$$

The energy spacing ε is 109.5 meV and corresponds to the energetic cost of forming *gauche* defects to "melt" the aliphatic chains. The energetic cost of one *gauche* defect is approximately 40 meV,[110] so the chosen value accounts for on average slightly more than two *gauche* defects in the aliphatic chains. Additionally, there is a small change in the volume of the ligand shell, which in the lipid bilayers translates to about a 19.5 meV enthalpy change

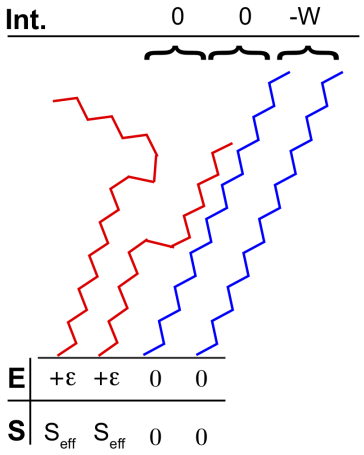

Figure 3.10: Ising-like model schematic. This schematic shows the different assumptions of the model. Straight chains are assumed to have no associated entropy or energy, while there is an energetic cost and increase in entropy from disordering the aliphatic chains. The interaction energy between chains also depends on the structure, with a favorable interaction energy only being present between two ordered chains.

per site as well. The coupling energy W is derived from the van der Waals interaction between two packed aliphatic chains. In close-packed stearic acid this energy is approximately 360 meV, but due to geometric differences and the steep drop-off of van der Waals interactions, the 140 meV is not unreasonable.[111,112] The coupling parameter was varied to better match the experimental results. Decreasing the coupling parameters results in a smaller change in the width and temperature of the phase transition, and shifts it to lower temperatures, as per Equation 3.2. Finally an entropy S of $14.6k_B$ is used, which corresponds to a degeneracy of several hundred thousand. While this value is quite high, there is a significant increase in configurational entropy as well as positional entropy upon chain melting. This value was chosen because previous experimental studies on lipid bilayer melting have determined an associated entropy change of $14.6k_B$.[108]

The results of simulating compositions consisting of 30% to 100% ODPA are shown in Figure 3.11. Figure 3.11A shows the change in the amount of the ordered phase as a function of temperature. The results are similar to that of the observed PL data; as the amount of ODPA in the ligand shell is increased the phase transition shifts to higher temperatures and narrows. It is possible to quantify the phase transition temperature and width again using the integral of the Cauchy distribution, as was done for the PL data, shown in Figure 3.8. Because the amount of the ordered phase is correlated to the mole fraction ODPA, χ_{ODPA}, there are only two fit parameters used, T_{PT} and ΔT, as shown in Equation 3.3.

$$\text{Fraction ordered phase} = \chi_{\mathrm{ODPA}} \left(1 - \tanh\left(\frac{T - T_{PT}}{\Delta T}\right)\right) - 1 \tag{3.3}$$

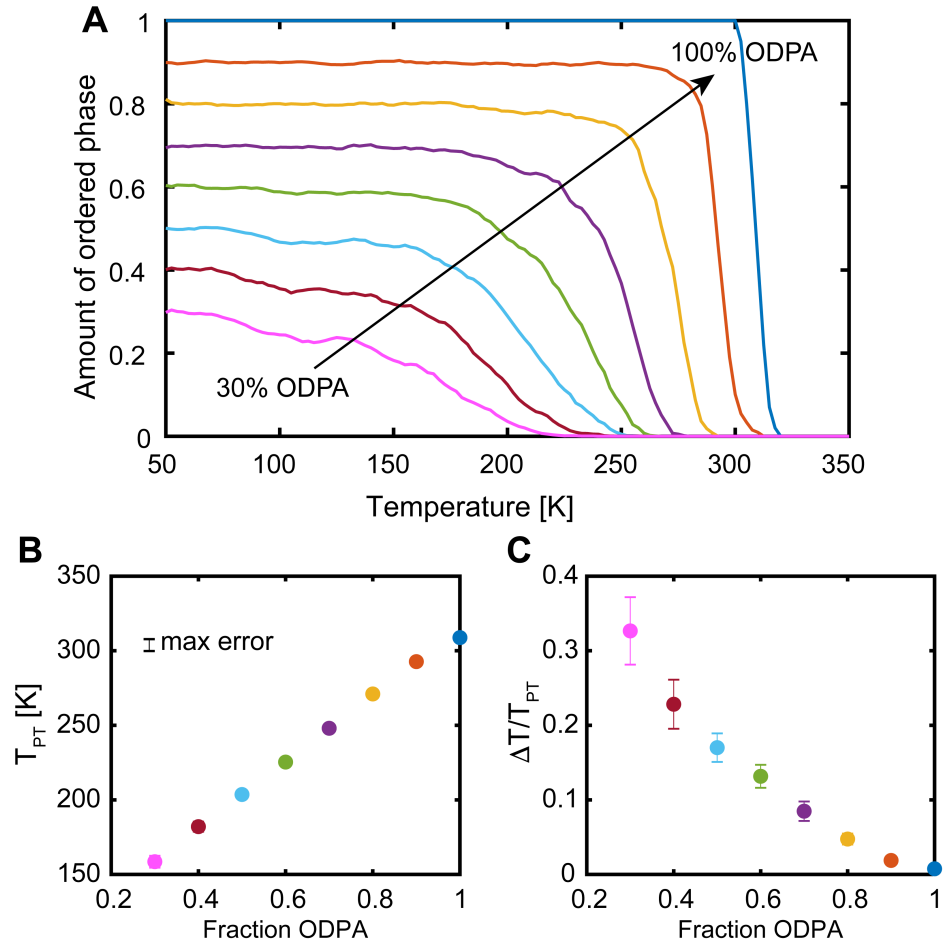

Figure 3.11: Ising simulations of the ligand phase transition. A) Amount of order at different temperatures for different OA fractions in the ligand shell. Phase transition temperature (B) and width (C) as a function of the amount of OA.

The results of fitting the data from Figure 3.11A to Equation 3.3 are shown in Figure 3.11B-C. The temperature range of the phase transition, which is approximately 120 K for the compositions studied, fits particularly well with the experimental results. The trend in describing the phase transition width generally matches the experiment as well, but the FWHM underestimates the phase transition width for sample N (36% ODPA) as compared to the simulation. All together, the general agreement between the model and the experimental results suggests that it is likely that the OA chains act as local points of disorder, facilitating the observed phase transition.

This model also gives insight into the microscopic nature of the phase transition. Shown in Figure 3.12 are snapshots in temperature of a configuration with 70% ODPA. At low temperatures, randomly distributed OA seed small disordered domains. This results in the phase

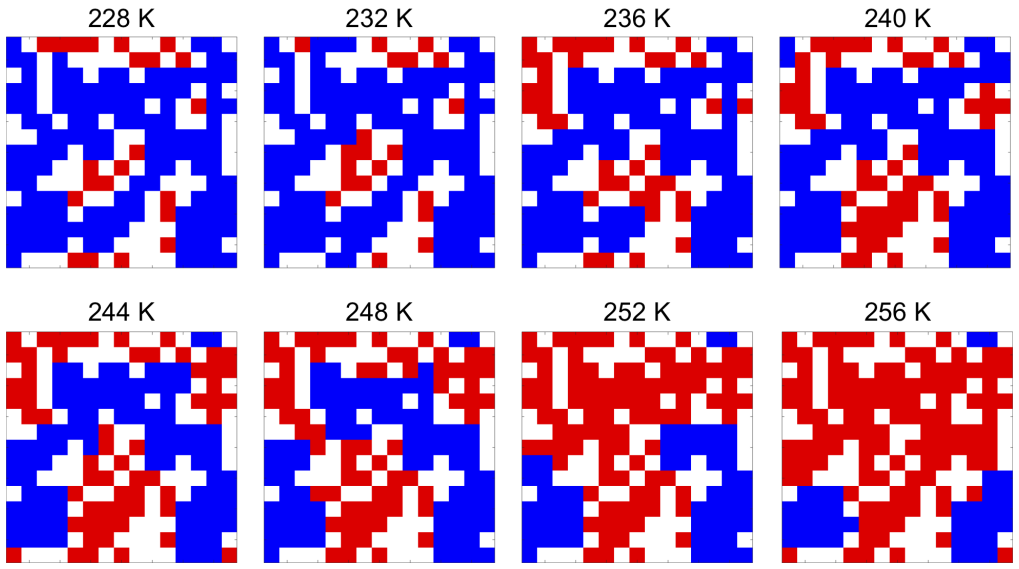

Figure 3.12: Temperature snapshots of the phase transition. Shown is the configuration of a 30% OA sample across the phase transition region. The blue represents ordered ODPA, the red represents disordered ODPA, and the white represents OA.

transition propagating outwards from regions with more OA as the temperature is increased. The regions in which there are the least amount of OA require the highest temperature to disorder. This also explains the slight asymmetry shown in the phase transition in Figure 3.11A. The shape of the phase transition is somewhat sharp as the system completely disorders, whereas during the initial melting there is a more gradual disordering. This is can be explained by the fact there is more variation in the environments of the ordered ODPA chains at the beginning of the phase transition than at the end, resulting in an asymmetric phase transition profile that is not present in the 100% ODPA case.

3.7 Additional ligand compositions

While the OA/ODPA system was chosen in order to be able to quantitatively determine the ligand composition on the surface of the QD, using other mixed ligand shell compositions is of interest to better determine what other factors impact the phase transition behavior. There are several areas of further exploration here, including the effects of chain length and the role of the binding group. To perform these ligand exchanges, a new sample of QDs of similar dimensions were synthesized. Rather than performing the emission calibration measurement in a cryostat, the results for this measurement are presented with the emission peak wavelength in the x-axis. In general, the emission peak wavelength can be considered proportional to the temperature, with larger (redder) wavelengths corresponding to higher temperatures. Sometimes at the phase transition temperature there is non-monotonic be-

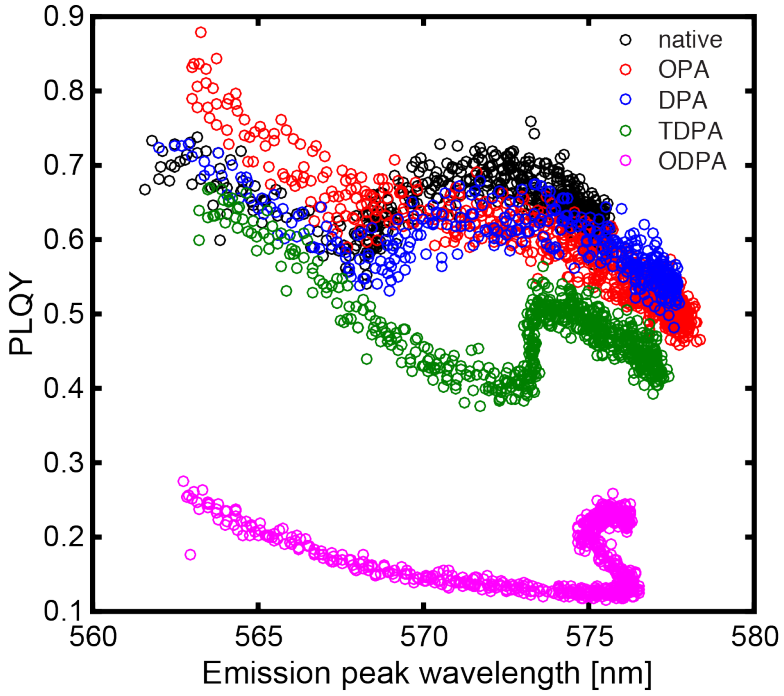

Figure 3.13: Dependence of phase transition temperature on chain length. The PLQY as a function of emission peak wavelength is shown. The OA in the ligand shell is exchanged to different chain lengths of phosphonic acids including octylphosphonic acid (OPA), decylphosphonic acid (DPA),tetradecylphosphonic acid (TDPA), and ODPA. The ODPA sample was cleaned in air, not under Ar, which explains the significant drop in PLQY compared to the other samples.

havior in the temperature-dependent PLQY. This is a result of imperfections in using the QD emission peak position as the temperature calibrant, and is discussed in more detail in Appendix B. The results presented here can be understood qualitatively even without an ideal calibration for the temperature.

The data shown in Figure 3.13 indicate that as the chain length of the capping ligand is increased, the phase transition shifts to higher temperatures, in agreement with previous work on CdSe QDs.[63] The chain length trend is more difficult to discuss here, as there is still 30-40% ODPA present on the surface of the QD after the OA has been exchanged. The fact that the OPA and DPA samples appear to have similar phase transition behavior as the native sample can be understood in terms of the Ising-like model developed. Because the OPA and DPA are short-chain ligands their van der Waals interaction with nearest neighbor ODPA is small, and thus more resembles the negligible interaction energy of OA or an empty lattice site. For this reason, there is no shift in the phase transition behavior for the short chain ligands. As the ligand chain length is increased to TDPA, the phase transition clearly shifts to higher temperatures, and is consistent with strong inter-ligand interactions between

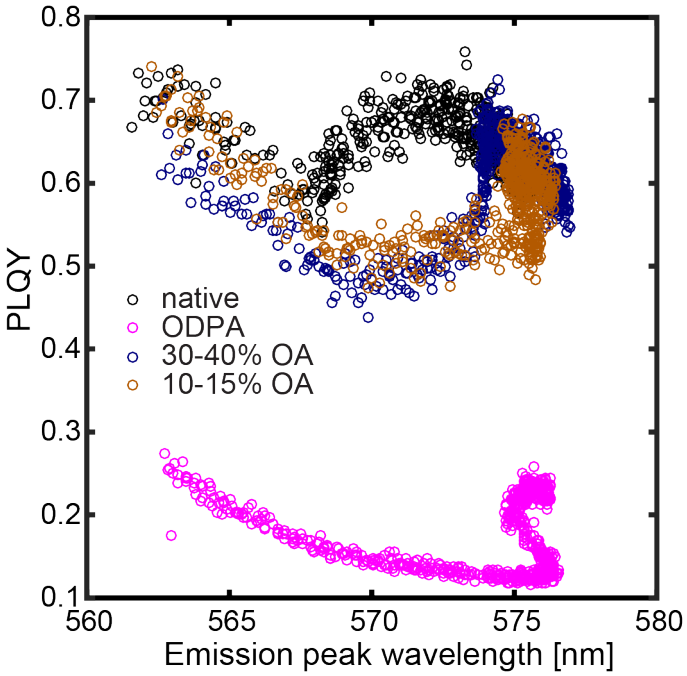

Figure 3.14: Phase transition behavior with stearic acid. Native and ODPA QDs are compared with QDs that are exchanged with stearic acid until 30-40% of OA (navy) or 10-15% of OA (tan) is remaining.

ordered TDPA and ODPA, although less so than between two ordered ODPA. The fully ODPA sample has the highest phase transition temperature as expected. The significantly lower PLQY and higher non-monotonic character for the all ODPA sample is likely partially due to the fact that the ODPA sample was cleaned in THF in air, and not under Ar as the rest of the samples. The data shown in Figure 3.13 confirms the expectations of how the phase transition is affected by the chain length.

The previous results suggest that the main factor that determines the phase behavior of the ligands on QD surfaces is the structure of the aliphatic chain. However, it is possible that the binding group could modify the phase transition behavior if it results in a significantly different tilt angle. This aliphatic chain would then interact differently with the ligands currently on the surface of the QD. To address this question, OA ligands on the QD were exchanged to stearic acid. The data comparing stearic acid exchanges to an ODPA exchange is shown in Figure 3.14. Quantification of the surface is particularly difficult in the case of partial exchange of stearic acid, as it is difficult to distinguish between bound ODPA and stearic acid. The most effective way of determining the binding of stearic acid is through observing the decrease in OA bound to the surface of the QD. Two different stearic acid compositions were synthesized, and the temperature-dependent PLQY was measured, as shown in Figure 3.14. As the amount of stearic acid is increased on the surface of the QD,

the phase transition shifts to higher temperatures and narrows, again as expected from the understanding developed in the above sections of this phase transition. The phase transition temperature of the tan curve looks slightly lower, but quite comparable to that of the ODPA sample, suggesting that there are minimal differences in the phase behavior due to the binding group in the QDs studied. One feature of note is that there is less of a decrease in PLQY in the stearic acid-exchanged samples when compared to ligand exchanges with phosphonic acids, shown for the same QDs in Figure 3.13. In the phosphonic acid-capped QDs the PLQY appears to decrease linearly before the phase transition temperature. However, for the samples that are ligand-exchanged to stearic acid there is a slight plateau in the change in PLQY with temperature before the phase transition. It is possible that this difference is due more to the degree to which the PLQY accurately reflects the phase composition of the ligand shell; the PLQY could be more sensitive to the conformation of phosphonic acids than carboxylic acids, which further supports the hypothesis that charge trapping is responsible for the observed change in PLQY.

3.8 Discussion

The systematic study of the order/disorder transition in mixed ligand shells presented here suggests several key areas for further analysis, which will be discussed in this section. Developing a better understanding of how the QD PL can be impacted by the ligand phase, comparing the PL and VT-FTIR measurements, relating the phase transition observed here to other systems, and determining what model parameters account for the observed phase transition are all of interest. We will first discuss the origin of the observed change in PL properties.

Both this work and that of several other groups now indicate that a transition in the optical properties correlates with a change in the structure of the ligand chains.[63,98] Similar effects occur for systems that have amine binding groups as well as those that have a mix of carboxylate and phosphonate binding groups. However, initial experiments, as shown in Figure 3.14 do suggest that there can be a difference in the degree of the observed PLQY change depending on the binding group used. In general, the mechanism by which the PLQY is impacted by the aliphatic chain structure must be one that could occur for a number of binding geometries. One potential explanation is that there is a change in the relative energy of of the QD surface states upon the ligand phase transition.

If there is a change in the binding group geometry during the ligand phase transition, that could explain the observed change in PLQY. There is likely a preferential orientation of the binding group to the QD. When the aliphatic chains are disordered, there is no impact on the binding group geometry. When the aliphatic chains are ordered, there can be an effective strain at the surface of the QD, analogous to the strain that arises at an interface between two lattice mismatched materials. The strain could cause a change in the angle of the binding group to the nanocrystal surface, which would reduce the degree of surface passivation present in the QD, thus lowering the PLQY when the ligands are ordered. There

is an additional possibility that a change in binding mode (changing between a bridging or chelating mode, for example) could also result in a change in surface passivation. A related phenomenon is a change in the binding group orientation modulating the dipole at the QD surface, which can shift the band energies relative to a surface trap.[99]

A change in the trap state energy suggests that there is coupling between the exciton and surface ligands. The presence of such an interaction can help explain the observed trend in FWHM: increasing upon ligand disordering. Due to the thin shell, the exciton can interact with surface states. Therefore, a higher amount of disorder at the surface can impact the QD optical properties. When the ligands are ordered, the ligand binding geometry is governed by the aliphatic chains. However, when the ligands are disordered there could be greater fluctuations in binding configurations, resulting in a broader emission spectrum. Computational work has shown that for small CdSe QDs, the ligands can have a significant impact in the homogeneous photoluminescence linewidth, so varying the ligand binding configurations could indeed result in a changing linewidth.[113]

The difference between the observed phase transition temperature for the VT-FTIR and the PL data is also an area of interest. The VT-FTIR data suggests a ligand phase transition temperature slightly below the the temperature determined using the photoluminescence data. Since the PL data is likely to be more sensitive to changes that occur near the nanoparticle surface, it might miss changes that occur further out into the aliphatic chains. Previous computational work on Au-dodecanethiolate nanocrystals has shown that *gauche* defects begin forming at lower temperatures on the outer carbons of the aliphatic chains, and then progress inward at higher temperatures to the nanocrystal surface.[107] The VT-FTIR measurements would be sensitive to the average configuration of the aliphatic chains, and thus predict a slightly lower phase transition temperature than the PL data, which is more sensitive to the aliphatic chain near the QD surface. Similarly, the observed difference in the phase transition width between the experiment and the model (particularly at high OA coverages), could partially be due to the failure of the model to take into account that the phase transition occurs at slightly different temperatures along the aliphatic chain.

As described in Section 3.4, the observed change in the as-CH_2 peak position, shown in Figure 3.5D, is smaller than in other systems. One possibility is that the surface curvature and faceting of these small particles reduces the order through an increase in chain defects at the facet edges, as has been observed previously in platelet systems[103] and has shown to be larger in smaller QDs.[114] Furthermore the larger spacing in the Cd sublattice as compared to elemental materials (such as Au) could also result in more disorder in the nominally ordered phase, as there would be weaker coupling between the aliphatic chains. This could be relevant in a number of systems, as the solubility of the nanocrystal is strongly impacted by the ligand shell conformation.[60,95,96] In order to maximize the solubility, which is desirable in achieving higher nanocrystal loadings, the ligand shell should be compatible with the organic solvent but not order into bundled domains. This can be achieved a number of ways, including by using branched ligands,,[60] or by including a ligand with a *cis* double bond, which would prevent packing of the straight chain ligands. Furthermore, the model suggests that short aliphatic chains, or unpassivated surface sites would also modify the

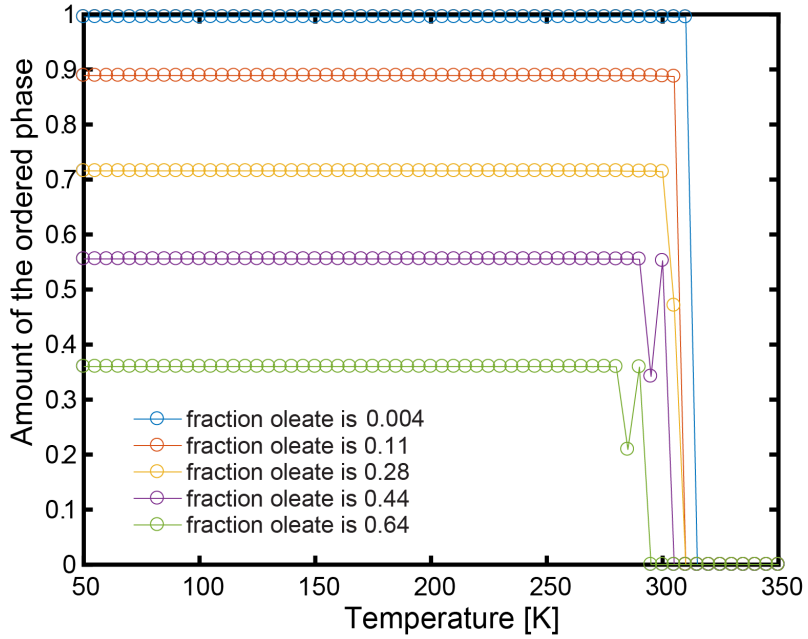

Figure 3.15: Phase transition behavior assuming segregated OA and ODPA. Simulations were performed assuming a square block of OA present in an otherwise ODPA ligand shell.

phase transition within the ODPA in the same manner. This is in agreement with the measurements performed on mixed ligand shells with shorter chain length phosphonic acids, as shown in Figure 3.13. Previous computational studies of the effect of surface coverage on the ligand phase transition confirms that indeed reducing the surface coverage has a significant impact on the phase transition temperature.[65]

The model presented in Figure 3.11 had one assumption that can give insight to the structure of the ligand shell. The model included OA that was randomly distributed within the ligand shell, and it mapped reasonably well to experimental results. However, it is also possible that the OA and ODPA ligands are segregated into different domains. Shown in Figure 3.15 are the results of a simulation that assumes an OA domain exists as a square block within the rest of the ODPA in the ligand shell. The resultant phase behavior clearly does not match the experimental results. There is only a small (approximately 20 K) decrease in the phase transition temperature when increasing the OA to 64% of the ligand shell. Furthermore, there is minimal change in the width of the phase transition, which is inconsistent with the experimental results. This suggests that over the course of the phase transition, the ODPA and the OA remain randomly distributed. The ligand exchange is performed well above the phase transition temperature, so this suggests that the entropy of mixing outweighs enthalpic segregation between the ODPA and the OA.

3.9 Conclusions

The results shown here demonstrate how introduction of OA and other short chain ligands can disrupt the packing of straight chain ODPA and stearic acid chains in the ligand shell of CdSe/CdS QDs. The amount of OA that is present in the ligand shell can be controlled, which in turn modifies the observed order/disorder phase transition that occurs within the ODPA. The presence of small domains of OA seed disorder within the ODPA, and can thus change the phase transition properties. The phase transition is studied using both PL and IR (FTIR and SFG) spectroscopies. The use of PL spectroscopies allows for precise determination of the phase transition temperature of the phase transition temperature and width. The IR spectroscopies complement the PL studies, and are critical in providing further information about the molecular details of the phase transition. The composition-dependence of this phase transition is further analyzed using an Ising-derived model of the phase transition, which shows how the OA disrupt the ODPA during the phase transition. The work highlights the importance of understanding structure-property relationships within the ligand shell structure. In addition to modulating the PL, the ligand shell structure can impact numerous other properties, including the inter-QD interactions and the permeability of the ligand shell, which would be relevant in QD self-assembly and photocatalysis studies, respectively.

Chapter 4

Temperature-Dependent Hole Transfer From Photoexcited QDs

4.1 Background

Temperature-dependent measurements of charge transfer from CdSe/CdS QDs to molecular acceptors can be of use in determining the activation barrier for the charge transfer process. This can help give insight into whether trap-mediated charge transfer is present, and can also give information about the Auger-assisted hole transfer process. At low temperatures, the Marcus parabolae narrow, so it is possible if the energy spacing between intraband states of the remaining charge is large enough (of similar magnitude to the reorganization energy) that the inverted regime could be recovered. While the lack of the inverted regime has also been shown in electron transfer from CdSe QDs, the energy spacing of the hole states is much closer, and can actually be approximated using a continuum model.[75] For this reason, this chapter focuses on the study of hole transfer from CdSe/CdS QDs to tethered ferrocene acceptors, a model system which has been previously developed.[18,76,115] In addition, studying hole transfer is of particular interest as slow hole transfer has been shown to limit efficiency in QD photocatalysis[116] and photovoltaics.[117]

The model system used consists of CdSe/CdS QDs bound via a thiolate head group to a series of six ferrocene-derived ligands with oxidation potentials spanning almost 800 meV.[76] The hole transfer rate can be determined using quenching of QD PL as a function of ferrocene ligands bound to the QD, which is measured through NMR.[18,76] In this chapter, the temperature-dependent hole transfer process will be explored.

4.2 Room temperature hole transfer

Before performing temperature-dependent hole transfer measurements, it is useful to understand the room temperature hole transfer behavior. One way by which the Auger-assisted

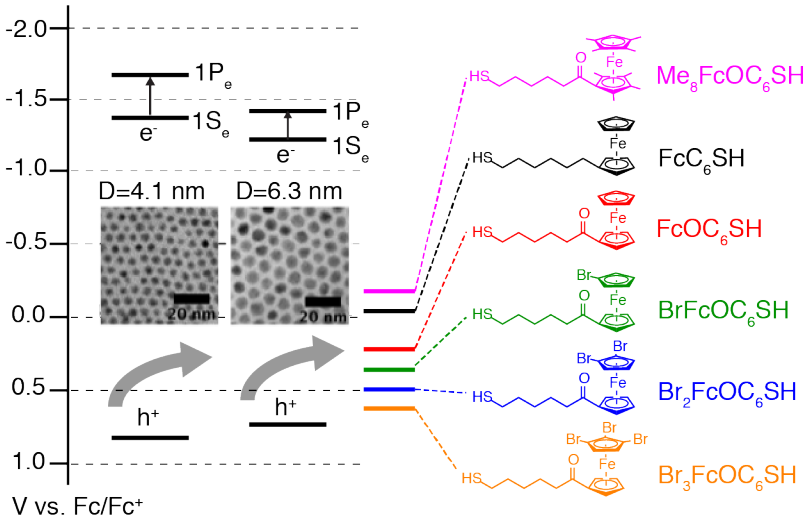

Figure 4.1: Energy level diagram for hole transfer, including the valence band edge and the two lowest energy conduction band states for the QDs studied. Electrochemical potentials of all ferrocene derivatives studied are shown against a ferrocene reference.

hole transfer mechanism can be tested is by varying the conduction band energy level spacings, which can be accomplished by changing the size of the CdSe/CdS QDs, and is presented here. The 1S-1P transition in the conduction can be measured by measuring the IR absorption of chemically reduced QDs.[118] The energy level diagram including the two differently-sized QDs and the electrochemical potentials of the synthesized ferrocene derivatives is shown in Figure 4.1. The 4.1 nm diameter QD has a core diameter of 2.2 nm, and the 6.3 nm diameter QD has a core diameter of 4.3 nm. As the size of the QDs is increased, there is a shift in the conduction band edge position of around 200 meV, but the valence band position shifts less than 100 meV. The 1S-1P energy level spacing can be tuned from about 200 meV for the 6.3 nm diameter QD to just under 300 meV for the 4.1 nm QD. This is relevant as the reorganization energy of the system, given previous measurements, has been shown to be around 400 meV. If the conduction band energy spacing is of similar energy, it is possible to then begin to resolve small decreases in the hole transfer rate at moderate driving forces.

To measure the room temperature charge transfer rate, steady state PL quenching curves were performed. Extinction coefficients of both the QDs and the different ferrocene species were determined and used to consistently determine the concentration of both QDs and ferrocene ligands. The extinction coefficient of the ferrocene ligands was determined by quantitative proton NMR spectroscopy and absorption spectroscopy. To determine this value for the QDs, a combination of absorption spectroscopy, TEM, and inductively coupled plasma-atomic emission spectroscopy (ICP-AES) was used, and is described in Appendix B. The results of the room temperature quenching curves are shown in Figure 4.2. For all

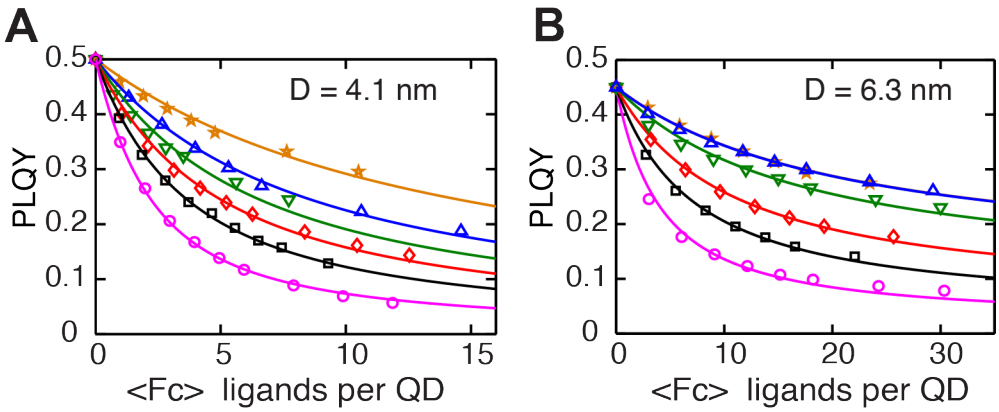

Figure 4.2: Room temperature quenching curves. PLQY quenching for QDs as a function of average number of ferrocene ligands bound per QD for the two QD sizes studied. The data points represent experimental data for each ferrocene ligand: Br_3FcOC_6SH (orange, pentagrams), Br_2FcOC_6SH (blue, upward triangles), $BrFcOC_6SH$ (green, downward triangles), $FcOC_6SH$ (red, diamonds), FcC_6SH (black, squares),Me_8FcOC_6SH (magenta, circles), and the solid lines represent fits to Equation 4.2.

samples, as the driving force for hole transfer is increased, there is increased PL quenching, as is predicted by the Auger-assisted hole transfer theory.[81]

$$\mathrm{PLQY}(N) = \frac{k_r}{k_r + k_{nr} + N k_{ht}} = \frac{\mathrm{PLQY}_o}{1 + N\tau_o k_{ht}} \tag{4.1}$$

The PLQY as a function of the number of bound ferrocene ligands, N, can be fit to Equation 4.1, where PLQY_o corresponds to the PLQY of the native QD and τ_o is the excited state lifetime of the native QDs. Since the number of ferrocene ligands per particle is low, implementation of a Poisson distribution, as shown in Equation 4.2, to describe the distribution of the number of ligands bound per QD results in more accurate fits to the model. The number of ligand binding sites is finite, but using the infinite sum does not make a difference, as for the size of the QDs used, no more than a small fraction of the ligand shell is expected to be replaced.

$$\mathrm{PLQY}(\langle N\rangle) = \sum_{N=0}^{\infty} \frac{\langle N\rangle^N e^{-\langle N\rangle}}{N!} \frac{\mathrm{PLQY}_o}{1 + N\tau_o k_{ht}} \tag{4.2}$$

The PL quenching curves are fit to Equation 4.2 as is shown in Figure 4.2. The PL quenching fits quite well to Equation 4.2, and from these fits k_{ht} at room temperature can be determined for each sample. As shown in Figure 4.3 as the driving force is increased, there is a monotonic increase in the hole transfer rate for both of the QDs studied. The Auger-assisted charge transfer mechanism can be used to fit the observed data. For these samples, the electron can be excited to higher energy states within the conduction band. From

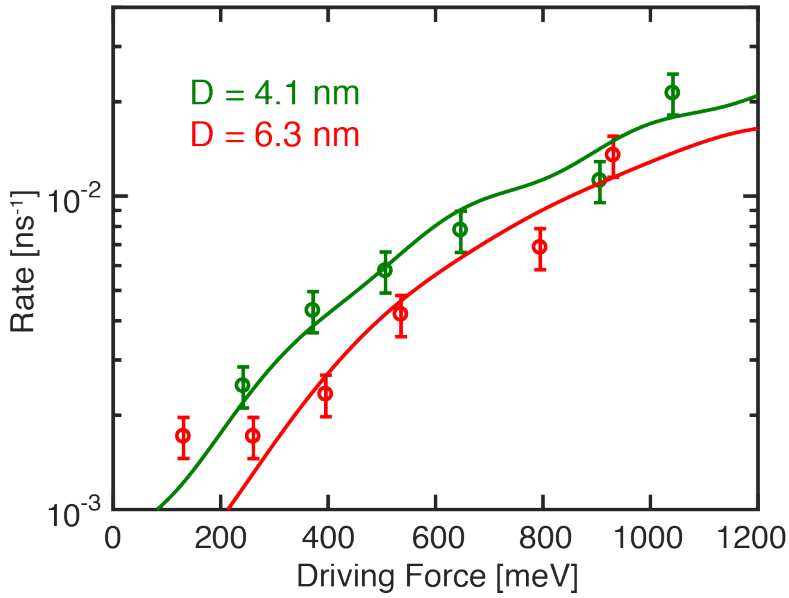

Figure 4.3: RT dependence of rate on driving force. Per molecule hole transfer rates as a function of driving force for the two QD sizes studied: 4.1 nm (green) and 6.3 nm (red). The solid line represent fits to Equation 4.3.

the 1S-1P spacing determined previously, higher energy intraband excitations, $E_{e,i}$, can be incorporated by using a previously developed model for CdSe cores.[119,120] The degeneracies of the conduction band states are given by the associated degeneracies of the spherical harmonics, $g_{e,i}$, resulting in fits of the form shown in Equation 4.3.

$$k_{ht} = \sum_{i=0} \frac{2\pi}{\hbar} g_{e,i} |H_{DA}|^2 \frac{1}{\sqrt{4\pi\lambda k_B T}} \times \exp\left(-\frac{(\lambda + \Delta G + E_{e,i})^2}{4\lambda k_B T}\right) \tag{4.3}$$

The results of fitting the room temperature hole transfer data to Equation 4.3 are shown in Figure 4.3. For these plots the reorganization energy is set to 400 meV, in agreement with previous work.[76,115] The only fitting parameter used is the donor-acceptor coupling, H_{DA}. For a model that incorporates only one fitting parameter the observed agreement between fit and experiment is quite good. In particular, for the 4.1 nm diameter QDs, the model begins to show some non-monotonic behavior even at room temperature. This is suggested by the small change in charge transfer rate between the hole transfer rates for $FcOC_6SH$ and FcC_6SH even at room temperature. However, it is difficult to draw conclusions from the change in hole transfer rate for one data point. In general, the observed room temperature charge transfer behavior observed here is consistent with previous measurements of hole transfer from QDs. Temperature-dependent studies of the charge transfer can now be used to gain more insight into the charge transfer mechanism.

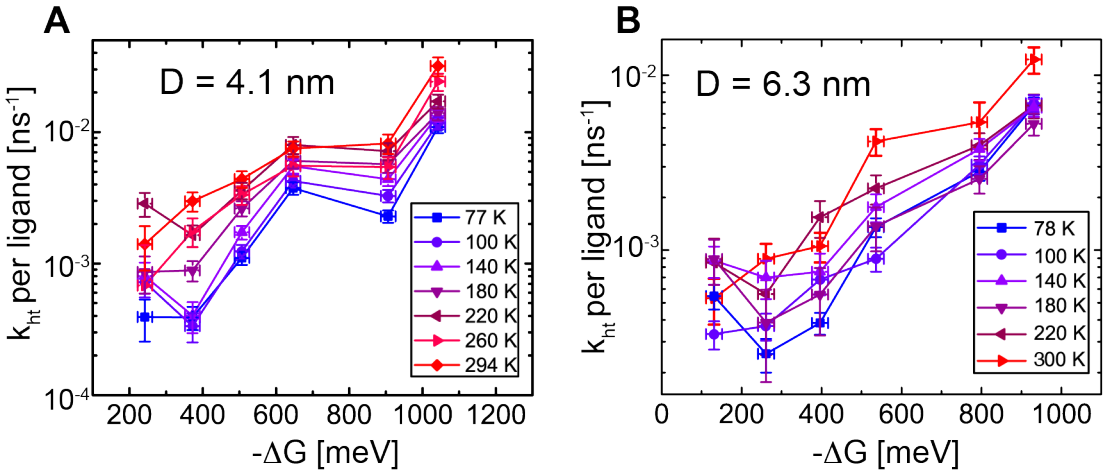

Figure 4.4: Temperature-dependent hole transfer measured by TRPL. Hole transfer as a function of driving force for the 4.1 nm diameter sample (A) and the 6.3 nm diameter sample (B).

4.3 Temperature-dependent hole transfer measurements

TRPL can be used to determine the temperature dependence of hole transfer. By comparing the lifetime extracted from the native QDs to the lifetime of a sample with a known number of ferrocene ligands bound to the QD, the hole transfer rate can be determined using Equation 4.4, where $\tau_{Fc}(N,T)$ describes the lifetime of QDs with N ferrocene ligands at a given temperature.

$$k_{ht}(T) = \frac{\tau_{Fc}(N,T)^{-1} - \tau_o(T)^{-1}}{N} \tag{4.4}$$

For the two QD samples, TRPL with and without ferrocene ligands was performed between 78 and 300 K. Between 10 to 30 ferrocene molecules were bound to each QD for this experiment. The number of ferrocene molecules bound was tuned to ensure there is adequate quenching, and that it is still possible to fit an accurate excited state lifetime. As was the case in Chapter 2, at low temperatures the lifetime decays were monoexponential, and therefore the computed lifetimes are independent of fitting range. Due to charge trapping processes at higher temperatures there is more deviation from monoexponential behavior, so the observed lifetime could be dependent on the fitting range. The results here were fit over the first decade for consistency, so there may be some systematic errors at higher temperatures. However, the relative comparisons between ligands should still be valid.

The temperature-dependent hole transfer rates measured through TRPL are shown in Figure 4.4. The TRPL data shows that for both the 4.1 nm and 6.3 nm diameter samples, there is approximately a 10-fold increase in the hole transfer rate as the temperature is

increased from 78 K to room temperature for all the ligands studied. In addition, inverted kinetics appears to be present between the third highest ($FcOC_6SH$) and second highest (FcC_6SH) driving force ligands measured, as was suggested by the room temperature data shown in Figure 4.3. However, it is unclear if this is evidence of the inverted regime, or simply error. To try to address this, temperature-dependent hole transfer rates are measured through the PLQY, which would address errors in fitting non-monoexponential lifetimes.

As was done with the TRPL measurements, temperature-dependent hole transfer rates can be measured by comparing the native PLQY, $PLQY_o$, to the PLQY of quenched samples using Equation 4.5, where $PLQY_{Fc}(N,T)$ describes the quenched PLQY given N bound ferrocene ligands. Temperature-dependent PLQY was measured by dissolving a mixture of QDs and ferrocene ligand in 3-methylpentane, flame-sealing the sample, and then collecting data as the sample warms to room temperature after being flash-frozen in liquid N_2, as was performed in Chapters 2 and 3. Due to sample limitations, the 4.1 nm diameter QD sample used in the room temperature quenching and temperature-dependent TRPL measurements was replaced with a 4.3 nm diameter core/shell QD using the same CdSe core for the subsequent sections. The small difference in diameter is unlikely to significantly impact the valence band maximum or the conduction band energy level spacings.

$$k_{ht}(T) = \frac{1}{\tau_o(T)N}\left(\frac{\mathrm{PLQY}_o(T)}{PLQY_{Fc}(N,T)} - 1\right) \tag{4.5}$$

A selection of the temperature-dependent hole transfer rate data measured using PLQY is shown in Figure 4.5. As with the TRPL hole transfer data shown in Figure 4.4, there is an increase of almost a factor of ten in the hole transfer rate for all ligands studied and for both samples. There is no evidence of the Marcus inverted regime in the data presented here, but the hole transfer rates and temperature-dependence are in agreement with the lifetime data. This suggests that both methods can be used to provide information about the temperature-dependent hole transfer process. Because the PLQY measurements are easier to collect and there is a potential source of error in fitting the TRPL data, further analysis of the temperature-dependent hole transfer rate is done using the temperature-dependent PLQY.

4.4 Analysis of the temperature-dependence

To gain a better understanding of what the expected temperature-dependent behavior is, three models of charge transfer are compared: the standard two-state model, a multi-state model (which uses the Auger-assisted charge transfer hypothesis), and a continuum model. The continuum model uses the expected density of states of the conduction band in bulk CdSe, with a volume corresponding to a 6 nm diameter QD. The temperature-dependent behavior of these three models is shown in Figure 4.6. As is expected, there is a significant change in the temperature-dependence of the charge transfer process as the driving force is changed. For the two-state model, as shown in Figure 4.6D, there is the most change with temperature at high and low driving forces compared to the reorganization energy. When

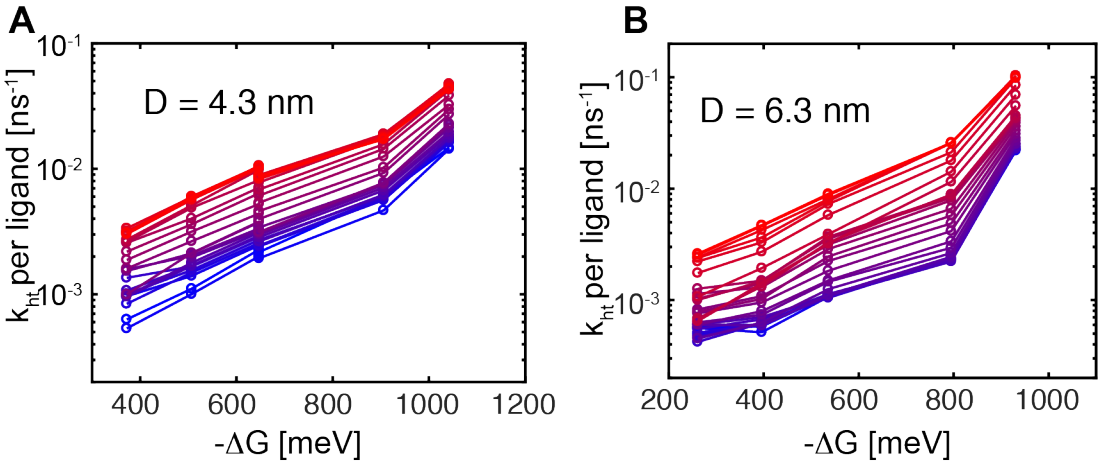

Figure 4.5: Temperature-dependent hole transfer rates measured using PLQY. The temperature ranges from 78 K (blue) to 300 K (red) for the 4.3 nm QD sample (A) and the 6.3 nm diameter QD sample (B).

the driving force is near the reorganization energy, a small increase in the hole transfer rate is observed, due to the exponential pre-factor described in Equation 4.3. This is supported by the Arrhenius plot shown in Figure 4.6G. For driving forces further away from the reorganization energy, there is clearly a larger activation barrier. Significantly different behavior is observed for both the multiple state model (Figure 4.6B,E,H) and the continuum model (Figure 4.6C,F,I). For these models, at driving forces higher than the reorganization energy, there is minimal change in the observed hole transfer rate with temperature, a signature of activation-less charge transfer at high driving forces. The observed behavior using these three models does not fit the temperature-dependence of the hole transfer rate observed with both lifetime (Figure 4.4) and PLQY (Figure 4.5).

In order to illustrate this difference, the Arrhenius plot of the hole transfer rate for the 6.3 nm QDs and the associated extracted activation energies are shown in Figure 4.7. Across the five driving forces studied, the activation energies range between 60 and 90 meV, and do not match the expected activation energies for any of the Marcus theory models (Figure 4.7B). Rather, the observed activation energies suggest that another process is responsible for the temperature-dependent hole transfer rate. One possibility is that rather than observing a direct hole transfer process, a stepwise hole transfer process is present, which would account for the observed activation energies.

4.5 Evidence for trap-mediated hole transfer

The QDs utilized in the study possess several hallmarks of surface charge trapping behavior including lower PLQY and non-monotonic TRPL decays, particularly at higher tempera-

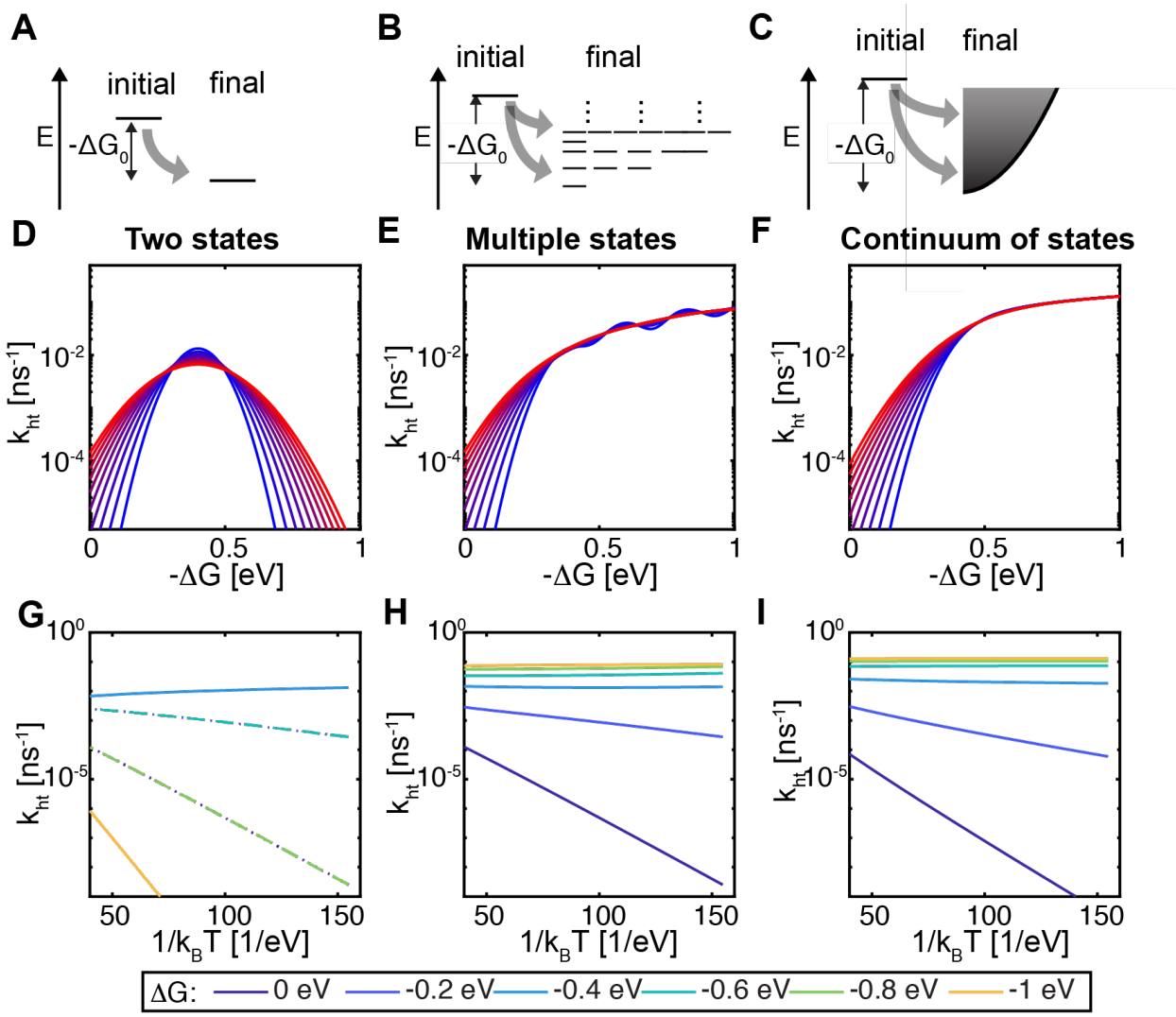

Figure 4.6: Marcus theory models of temperature-dependent charge transfer. Schematics of the two state model, the Auger-assisted model, and the continuum model (A-C, respectively), and temperature-dependent rates for respective models (D-F) all using the same donor-acceptor coupling and a reorganization energy of 0.4 eV, ranging between 75 K (blue line) and 300 K (red line). The Arrhenius plots for a selection of driving forces are shown for the three models (G-I), in the same order.

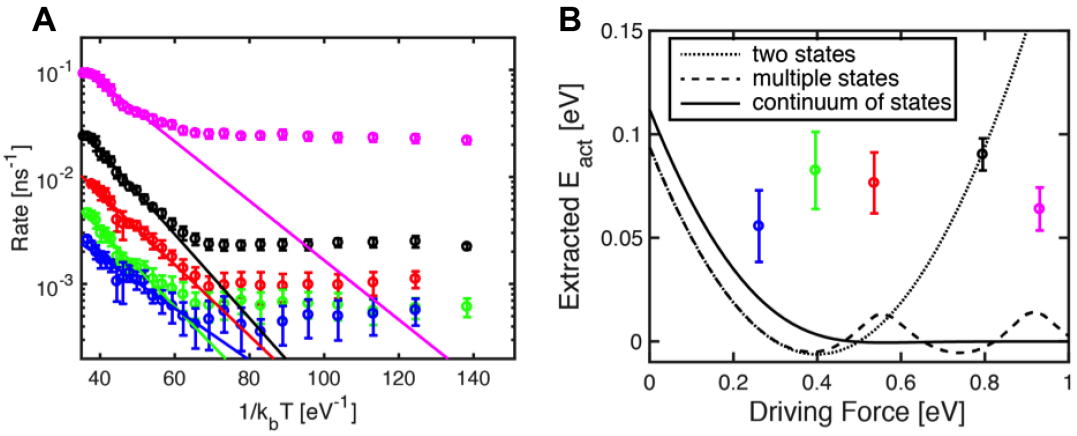

Figure 4.7: Arrhenius behavior for the 6.3 nm QDs. A) Arrhenius plots of the hole transfer rate using the temperature-dependent PLQY data for the five ferrocene ligands studied. The solid lines show linear fits over the activated charge transfer regime B) Extracted activation energies for different driving forces and the expected activation energies for the three charge transfer models.The five different driving forces correspond to the respective ligands Br_2FcOC_6SH (blue), $BrFcOC_6SH$ (green), $FcOC_6SH$ (red), FcC_6SH (black), Me_8FcOC_6SH (magenta).

tures. A number of studies have suggested that the temperature-dependence of QD PL can be attributed to changes in the population of QD surface traps.[28–30] In particular, the observed hole transfer rate would be sensitive to population of reversible trap states in the QD; although hole transfer from an irreversible trap state to tethered ferrocene ligands is also possible, this process would not modify either the excited state lifetime or the PLQY, so such hole transfer processes would not be visible in the current study. Because reversible trapping still allows for band-edge PL, observing reversible trap-mediated hole transfer through PL quenching is possible. Previous computational work has shown that depending on the energy level of the reversible trap, it can outcompete direct charge transfer processes.[115] For example, computational work has shown that binding of FcC_6SH to a CdSe/CdS dot-in-rod creates a hole trap slightly below (higher in energy) the valence band edge.[115] If this trap is less than 200 meV, the stepwise process becomes more favorable than direct charge transfer. Additionally, due to the shorter distance separating the exciton from a surface trap than the Fc in the ligand used, trapping to a surface trap should be much faster than the direct hole transfer process. Computational work has estimated that the charge trapping process is about 700 times faster than the direct hole transfer.[115] Experimental work, which compares the hole transfer rate to FcC_6SH and FcC_3SH, can also be used to estimate that the hole trapping process is on the order of 10^3 times faster than direct charge transfer to FcC_6SH.[18] Similarly, as the back hole transfer (from the surface state into the exciton) would be energetically favorable, that hole transfer rate would also be much faster than the direct hole

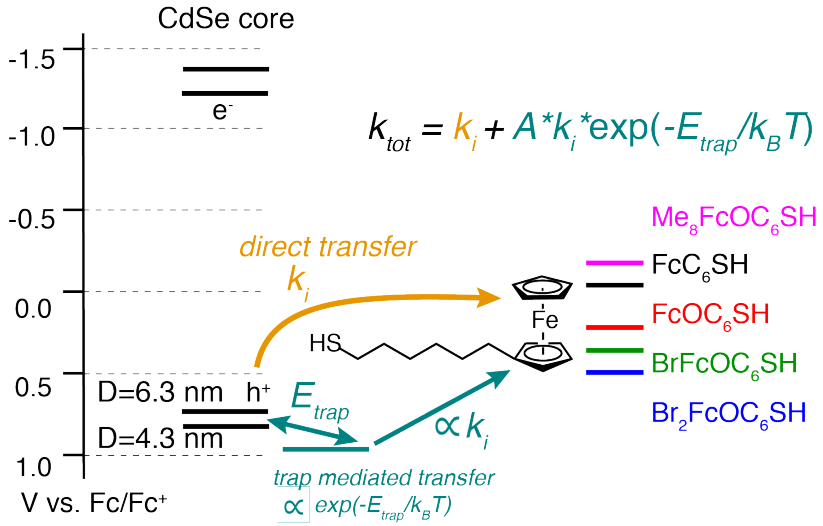

Figure 4.8: Two-step hole transfer process energy diagram. The model here includes a charge transfer rate that is the sum of the direct and stepwise pathways. Stepwise hole transfer relies on thermal excitation into a trap energy, E_{trap}, which describes the temperature dependence of the hole transfer.

transfer rate. Therefore, the population of the trap state can be assumed to be in thermal equilibrium with the exciton.

$$k_{tot} = k_i + A \times k_i \times \exp\left[-E_{\text{trap}}/k_BT\right] \tag{4.6}$$

The associated two-step charge transfer model is shown schematically in Figure 4.8 and described in Equation 4.6. While a distribution of trap state energies is most likely present in this system, for simplicity only a single trap energy E_{trap} below the valence band is used. In addition, this model assumes that there is no change in the dependence of the hole transfer process on driving force and includes an additional pre-factor A that describes both the degeneracy of the trap state and any increase in coupling between the hole and ferrocene due to the presence of surface trapping.

Global fits to Equation 4.6 are performed for both the 4.3 nm and 6.3 nm QDs, and are shown in Figure 4.9. From these fits, values for E_{trap} are determined, as shown in Figure 4.9. Interestingly, E_{trap} is about 50 meV larger for the 6.3 nm QD than for the 4.3 nm QD. This matches the expected difference in valence band levels for the two QDs, and suggests that the trap energy is independent of the QD valence band position. This implies that the trap state consists of a molecular state, not one that is dependent on the QD size. As previous work has suggested that thiols bound to a CdSe/CdS QD surface would create a trap state about 300 meV below the valence band,[115] other undercoordinated S atoms at the QD surface could reasonably be expected to induce trap energies closer to the valence band edge, and therefore more thermally accessible.

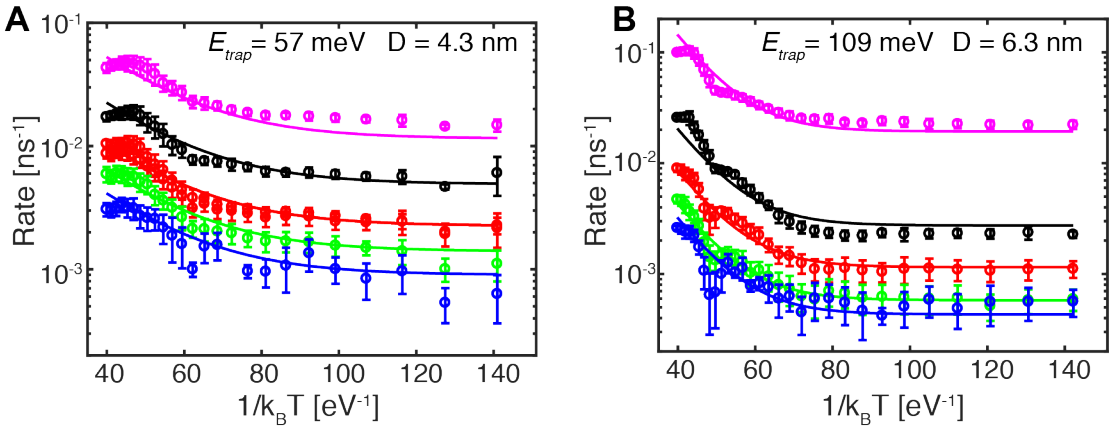

Figure 4.9: Global fits to the two-step hole transfer model for the 4.3 nm diameter QD (A) and the 6.3 nm diameter QD (B).

One simplification used in the two-step model described in Equation 4.6 is that the inherent temperature-dependence in the one-step hole transfer rate k_i is neglected. As shown in Figure 4.6, at driving forces above more than 200 meV or so, there is minimal change in the expected hole transfer rate with temperature for the Auger-assisted charge transfer mechanism. This would result in minimal temperature dependence in k_i, particularly when compared to the strong temperature-dependence of the reversible hole trapping process.

The two-step charge transfer processed observed here also has implications for the Auger-assisted charge transfer model. While it is difficult to determine the thermal population of the trap state, as both the degeneracy and change in coupling are included in A, the results show that the use of a temperature- and mechanism-invariant k_i matches well with the experimental data. Therefore, even for the trap-mediated charge transfer mechanism, in which the hole is no longer localized in the QD core, no inverted regime is observed. This suggests that the electron and hole are still coupled (hole transfer can still be accompanied by electron excitation) even when the hole is localized to a surface trap. The precise states into which the electron can be excited could be more complex in this model. Rather than electron excitation into higher energy conduction band states, it is possible that the electron could access different surface trap states as well. The results presented here indicate the importance of understanding surface trapping behavior in QD systems, and highlight the positive role such trap states can have in increasing the rates of hole transfer from QDs to molecular acceptors.

4.6 Conclusions

The temperature-dependent study of hole transfer from photoexcited QDs to tethered molecular acceptors revealed a trap-mediated mechanism that increases the hole transfer rate at

higher temperatures. Despite the presence of significant hole trapping, no inverted regime was observed during this study, which suggests that even when the hole traps to the surface of the QD, the hole transfer cannot be described by simple two-state Marcus theory. While performing low-temperature measurements did not prove or disprove the Auger-assisted hole transfer theory, the study presented here provides insight on how to test this theory. Rather than by lowering the temperature, the electron-hole coupling could be tuned by controlling surface trapping and charge separation in QD heterostructures prior to hole transfer. Reducing this coupling should result in the emergence of the inverted regime at high driving forces and a confirmation of the Auger-assisted charge transfer theory. This poses an interesting avenue for future work. The observation of reversible trap-mediated hole transfer is also important for future studies. This work suggests that the trap site is molecular in nature, and likely related to undercoordinated surface S or thiol binding. By controlling the surface chemistry of the QD, it should be possible to promote a two-step hole transfer process. This would provide another avenue by which holes can be effectively extracted from QDs.

Chapter 5

Concluding Remarks

The temperature-dependent studies described in this dissertation highlight the complexity of the photophysics present in QD systems. The work performed in Chapter 2 shows how the radiative rate in CdSe/CdS core/shell QDs changes with temperature and core and shell dimensions. Due to the presence of lattice fluctuations and low-lying electron excited states, there is a significant decrease in the radiative rate with increasing temperature. This is of significance for QDs because a decrease in the radiative rate makes QDs more susceptible to nonradiative recombination, an often undesirable pathway. The work for Chapter 2 suggests that there is likely to be an optimal shell thickness for these QDs, and growing too large of a shell could result in a diminished PLQY, an observation that has been previously observed.[121] The results also suggest that for QDs operating at higher temperatures, it is more important to optimize the shell thickness for both the radiative and nonradiative rates.

Similarly, the results shown in Chapter 3 indicate that the structure of the ligand shell can also play a role in tuning nonradiative recombination in CdSe/CdS QDs. By changing the ligand shell from the ordered to the disordered phase, the PLQY is improved. The temperature at which this occurs can also be controlled by changing the degree of unsaturation or the chain length of the aliphatic chain. The ability to control the phase of the ligand shell is also of interest as the ligand shell phase should impact a number of QD properties, including solubility, permeability, and self-assembly. Once it is possible to control the phase of the ligand shell, the effect of the ligand shell structure on these properties can be determined. In addition, these results demonstrate the importance of developing a better understanding of surface trapping in QD systems.

The results presented in Chapter 4 show the positive role that surface traps can play in improving hole transfer from QDs. Due to the presence of surface traps, holes can transfer faster from the photoexcited QD to the molecular acceptor. This study of reversible-trap mediated charge transfer indicates that if it were possible to control the trap state landscape at the surface of the QD, it might be possible to improve charge transfer processes, which is an interesting area for future research. Relatedly, the measurements performed in Chapter 4 were sensitive only to reversible trap-mediated hole transfer. Hole transfer from irreversible traps is also possible, and could be a promising question for future research.

This dissertation shows how temperature-dependent spectroscopy can be a useful tool to better understand the photophysics and ligand shell structure in QD systems. Temperature-dependent spectroscopies facilitated an improved understanding of a number of QD phenomena, including the role lattice fluctuations have on the radiative rate, how the composition of the ligand shell impacts an order/disorder transition within the ligands, and how reversible charge trapping can increase the rate of hole transfer.

Bibliography

(1) Alivisatos, A. P. *Science* **1996**, *271*, 933–937.

(2) Zrazhevskiy, P.; Sena, M.; Gao, X. *Chem. Soc. Rev.* **2010**, *39*, 4326–4354.

(3) Jasieniak, J.; Smith, L.; van Embden, J.; Mulvaney, P.; Califano, M. *J. Phys. Chem. C* **2009**, *113*, 19468–19474.

(4) Scholes, G. D.; Rumbles, G. *Nat. Mater.* **2006**, *5*, 683–696.

(5) Goldstein, A. N.; Echer, C. M.; Alivisatos, A. P. *Science* **1992**, *256*, 1425–1427.

(6) Tolbert, S. H.; Alivisatos, A. P. *Science* **1994**, *265*, 373–376.

(7) Chen, O.; Zhao, J.; Chauhan, V. P.; Cui, J.; Wong, C.; Harris, D. K.; Wei, H.; Han, H.-S.; Fukumura, D.; Jain, R. K.; Bawendi, M. G. *Nat. Mater.* **2013**, *12*, 445–451.

(8) Hu, X.; Gao, X. *ACS Nano* **2010**, *4*, 6080–6086.

(9) Talapin, D. V.; Nelson, J. H.; Shevchenko, E. V.; Aloni, S.; Sadtler, B.; Alivisatos, A. P. *Nano Lett.* **2007**, *7*, 2951–2959.

(10) Pu, C.; Peng, X. *J. Am. Chem. Soc.* **2016**, *138*, 8134–8142.

(11) Medintz, I. L.; Uyeda, H. T.; Goldman, E. R.; Mattoussi, H. *Nat. Mater.* **2005**, *4*, 435–446.

(12) Holmes, J. D.; Ziegler, K. J.; Doty, R. C.; Pell, L. E.; Johnston, K. P.; Korgel, B. A. *J. Am. Chem. Soc.* **2001**, *123*, 3743–3748.

(13) Mastronardi, M. L.; Hennrich, F.; Henderson, E. J.; Maier-Flaig, F.; Blum, C.; Reichenbach, J.; Lemmer, U.; Kübel, C.; Wang, D.; Kappes, M. M.; Ozin, G. A. *J. Am. Chem. Soc.* **2011**, *133*, 11928–11931.

(14) Song, W. S.; Kim, J. H.; Lee, J. H.; Lee, H. S.; Do, Y. R.; Yang, H. *J. Mater. Chem.* **2012**, *22*, 21901–21908.

(15) Protesescu, L.; Yakunin, S.; Bodnarchuk, M. I.; Krieg, F.; Caputo, R.; Hendon, C. H.; Yang, R. X.; Walsh, A.; Kovalenko, M. V. *Nano Lett.* **2015**, *15*, 3692–3696.

(16) Bekenstein, Y.; Koscher, B. A.; Eaton, S. W.; Yang, P.; Alivisatos, A. P. *J. Am. Chem. Soc.* **2015**, *137*, 16008–16011.

(17) Shirasaki, Y.; Supran, G. J.; Bawendi, M. G.; Bulović, V. *Nat. Photonics* **2013**, *7*, 13–23.

(18) Ding, T. X.; Olshansky, J. H.; Leone, S. R.; Alivisatos, A. P. *J. Am. Chem. Soc.* **2015**, *137*, 2021–2029.

(19) Amirav, L.; Oba, F.; Aloni, S.; Alivisatos, A. P. *Angew. Chem. Int. Ed.* **2015**, *54*, 7007–7011.

(20) Kamat, P. V. *J. Phys. Chem. C* **2008**, *112*, 18737–18753.

(21) Amirav, L.; Alivisatos, A. P. *J. Phys. Chem. Lett.* **2010**, *1*, 1051–1054.

(22) Kalisman, P.; Nakibli, Y.; Amirav, L. *Nano Lett.* **2016**, *16*, 1776–1781.

(23) Caputo, J. A.; Frenette, L. C.; Zhao, N.; Sowers, K. L.; Krauss, T. D.; Weix, D. J. *J. Am. Chem. Soc.* **2017**, *139*, 4250–4253.

(24) Lian, S.; Kodaimati, M. S.; Dolzhnikov, D. S.; Calzada, R.; Weiss, E. A. *J. Am. Chem. Soc.* **2017**, *139*, 8931–8938.

(25) Lian, S.; Kodaimati, M. S.; Weiss, E. A. *ACS Nano* **2018**, *12*, 568–575.

(26) Biadala, L.; Siebers, B.; Gomes, R.; Hens, Z.; Yakovlev, D. R.; Bayer, M. *J. Phys. Chem. C* **2014**, *118*, 22309–22316.

(27) Efros, A.; Rosen, M.; Kuno, M.; Nirmal, M.; Norris, D.; Bawendi, M. *Phys. Rev. B* **1996**, *54*, 4843–4856.

(28) Jones, M.; Lo, S. S.; Scholes, G. D. *Proc. Natl. Acad. Sci. U.S.A.* **2009**, *106*, 3011–3016.

(29) Mooney, J.; Krause, M. M.; Saari, J. I.; Kambhampati, P. *Phys. Rev. B* **2013**, *87*, 081201.

(30) Mooney, J.; Krause, M. M.; Kambhampati, P. *J. Phys. Chem. C* **2014**, *118*, 7730–7739.

(31) Bae, W. K.; Padilha, L. a.; Park, Y. S.; McDaniel, H.; Robel, I.; Pietryga, J. M.; Klimov, V. I. *ACS Nano* **2013**, *7*, 3411–3419.

(32) Carbone, L. et al. *Nano Lett.* **2007**, *7*, 2942–2950.

(33) Coropceanu, I.; Rossinelli, A.; Caram, J. R.; Freyria, F. S.; Bawendi, M. G. *ACS Nano* **2016**, *10*, 3295–3301.

(34) Mahler, B.; Nadal, B.; Bouet, C.; Patriarche, G.; Dubertret, B. *J. Am. Chem. Soc.* **2012**, *134*, 18591–18598.

(35) Hens, Z.; Martins, J. C. *Chem. Mater.* **2013**, *25*, 1211–1221.

(36) Rabouw, F. T.; Kamp, M.; van Dijk-Moes, R. J. A.; Gamelin, D. R.; Koenderink, A. F.; Meijerink, A.; Vanmaekelbergh, D. *Nano Lett.* **2015**, *15*, 7718–7725.

(37) Katari, J. E. B.; Colvin, V. L.; Alivisatos, A. P. *J. Phys. Chem.* **1994**, *98*, 4109–4117.

(38) Hines, D. A.; Becker, M. A.; Kamat, P. V. *J. Phys. Chem. C* **2012**, *116*, 13452–13457.

(39) Minotto, A.; Todescato, F.; Fortunati, I.; Signorini, R.; Jasieniak, J. J.; Bozio, R. *J. Phys. Chem. C* **2014**, *118*, 24117–24126.

(40) Griffiths, D., *Introduction to Quantum Mechanics*; Pearson international edition; Pearson Prentice Hall: 2005.

(41) Norris, D. J. In *Nanocrystal Quantum Dots*, Klimov, V., Ed., 3rd ed.; CRC Press: 2010; Chapter 2, pp 63–96.

(42) Kim, S.; Fisher, B.; Eisler, H.-J.; Bawendi, M. *J. Am. Chem. Soc.* **2003**, *125*, 11466–11467.

(43) Steiner, D.; Dorfs, D.; Banin, U.; Della Sala, F.; Manna, L.; Millo, O. *Nano Lett.* **2008**, *8*, 2954–2958.

(44) Wu, K.; Rodriguez-Cordoba, W. E.; Liu, Z.; Zhu, H.; Lian, T. *ACS Nano* **2013**, *7*, 7173–7185.

(45) Eshet, H.; Grünwald, M.; Rabani, E. *Nano Lett.* **2013**, *13*, 5880–5885.

(46) Labeau, O.; Tamarat, P.; Lounis, B. *Phys. Rev. Lett.* **2003**, *90*, 257404.

(47) Brovelli, S.; Schaller, R. D.; Crooker, S. A.; García-Santamaría, F.; Chen, Y.; Viswanatha, R.; Hollingsworth, J. a.; Htoon, H.; Klimov, V. I. *Nat. Commun.* **2011**, *2*, 280.

(48) Green, M. L. *J. Organomet. Chem* **1995**, *500*, 127–148.

(49) Anderson, N. C.; Hendricks, M. P.; Choi, J. J.; Owen, J. S. *J. Am. Chem. Soc.* **2013**, *135*, 18536–18548.

(50) Gomes, R.; Hassinen, A.; Szczygiel, A.; Zhao, Q.; Vantomme, A.; Martins, J. C.; Hens, Z. *J. Phys. Chem. Lett.* **2011**, *2*, 145–152.

(51) Kim, W.; Lim, S. J.; Jung, S.; Shin, S. K. *J. Phys. Chem. C* **2010**, *114*, 1539–1546.

(52) Gao, Y.; Peng, X. *J. Am. Chem. Soc.* **2015**, *137*, 4230–4235.

(53) Hassinen, A.; Moreels, I.; De Nolf, K.; Smet, P. F.; Martins, J. C.; Hens, Z. *J. Am. Chem. Soc.* **2012**, *134*, 20705–12.

(54) Zhang, H.; Hu, B.; Sun, L.; Hovden, R.; Wise, F. W.; Muller, D. A.; Robinson, R. D. *Nano Lett.* **2011**, *11*.

(55) Baumgardner, W. J.; Whitham, K.; Hanrath, T. *Nano Lett.* **2013**, *13*, 3225–3231.

(56) Lee, J.-S.; Kovalenko, M. V.; Huang, J.; Chung, D. S.; Talapin, D. V. *Nat. Nanotech.* **2011**, *6*, 348–52.

(57) Luther, J. M.; Law, M.; Song, Q.; Perkins, C. L.; Beard, M. C.; Nozik, A. J. *ACS Nano* **2008**, *2*, 271–280.

(58) Akselrod, G. M.; Prins, F.; Poulikakos, L. V.; Lee, E. M. Y.; Weidman, M. C.; Mork, A. J.; Willard, A. P.; Bulović, V.; Tisdale, W. A. *Nano Lett.* **2014**, *14*, 3556–3562.

(59) Nienhaus, L.; Wu, M.; Geva, N.; Shepherd, J. J.; Wilson, M. W.; Bulović, V.; Van Voorhis, T.; Baldo, M. A.; Bawendi, M. G. *ACS Nano* **2017**, *11*, 7848–7857.

(60) Yang, Y.; Qin, H.; Jiang, M.; Lin, L.; Fu, T.; Dai, X.; Zhang, Z.; Niu, Y.; Cao, H.; Jin, Y.; Zhao, F.; Peng, X. *Nano Lett.* **2016**, *16*, 2133–2138.

(61) Dorokhin, D.; Tomczak, N.; Han, M.; Reinhoudt, N.; Velders, A. H.; Vancso, G. J. *ACS Nano* **2009**, *3*, 661–667.

(62) Calzada, R.; Thompson, C. M.; Westmoreland, D. E.; Edme, K.; Weiss, E. A. *Chem. Mater.* **2016**, *28*, 6716–6723.

(63) Wuister, S. F.; Van Houselt, A.; De Mello Donegá, C.; Vanmaekelbergh, D.; Meijerink, A. *Angew. Chem. Int. Ed.* **2004**, *43*, 3029–3033.

(64) Widmer-Cooper, A.; Geissler, P. *Nano Lett.* **2014**, *14*, 57–65.

(65) Widmer-Cooper, A.; Geissler, P. L. *ACS Nano* **2016**, *10*, 1877–1887.

(66) Luedtke, W. D.; Landman, U. *J. Phys. Chem.* **1996**, *100*, 13323–13329.

(67) Ghorai, P. K.; Glotzer, S. C. *J. Phys. Chem. C* **2007**, *111*, 15857–15862.

(68) Badia, A.; Cuccia, L.; Demers, L.; Morin, F.; Lennox, R. B. *J. Am. Chem. Soc.* **1997**, *119*, 2682–2692.

(69) Kister, T.; Monego, D.; Mulvaney, P.; Widmer-Cooper, A.; Kraus, T. *ACS Nano* **2018**, *12*, 5969–5977.

(70) Wang, Z.; Schliehe, C.; Bian, K.; Dale, D.; Bassett, W. A.; Hanrath, T.; Klinke, C.; Weller, H. *Nano Lett.* **2013**, *13*, 1303–1311.

(71) Geva, N.; Shepherd, J. J.; Nienhaus, L.; Bawendi, M. G.; Van Voorhis, T. *J. Phys. Chem. C* **2018**, *122*, 26267–26274.

(72) Menagen, G.; Macdonald, J. E.; Shemesh, Y.; Popov, I.; Banin, U. *J. Am. Chem. Soc.* **2009**, *131*, 17406–17411.

(73) Marcus, R. *Ann. Rev. Phys. Chem.* **1964**, *15*, 155–196.

(74) Miller, J. R.; Calcaterra, L. T.; Closs, G. L. *J. Am. Chem. Soc.* **1984**, *106*, 3047–3049.

(75) Zhu, H.; Yang, Y.; Hyeon-Deuk, K.; Califano, M.; Song, N.; Wang, Y.; Zhang, W.; Prezhdo, O. V.; Lian, T. *Nano Lett.* **2014**, *14*, 1263–1269.

(76) Olshansky, J. H.; Ding, T. X.; Lee, Y. V.; Leone, S. R.; Alivisatos, A. P. *J. Am. Chem. Soc.* **2015**, *137*, 15567–15575.

(77) Zhu, H.; Yang, Y.; Wu, K.; Lian, T. *Ann. Rev. Phys. Chem.* **2016**, *67*, 259–281.

(78) Morris-Cohen, A. J.; Frederick, M. T.; Cass, L. C.; Weiss, E. A. *J. Am. Chem. Soc.* **2011**, *133*, 10146–10154.

(79) Lian, S.; Weinberg, D. J.; Harris, R. D.; Kodaimati, M. S.; Weiss, E. A. *ACS Nano* **2016**, *10*, 6372–6382.

(80) Knowles, K. E.; Peterson, M. D.; McPhail, M. R.; Weiss, E. a. *J. Phys. Chem. C* **2013**, *117*, 10229–10243.

(81) Hyeon-Deuk, K.; Kim, J.; Prezhdo, O. V. *J. Phys. Chem. Lett.* **2015**, *6*, 244–249.

(82) Balan, A. D.; Eshet, H.; Olshansky, J. H.; Lee, Y. V.; Rabani, E.; Alivisatos, A. P. *Nano Lett.* **2017**, *17*, 1629–1636.

(83) Olshansky, J. H.; Balan, A. D.; Ding, T. X.; Fu, X.; Lee, Y. V.; Alivisatos, A. P. *ACS Nano* **2017**, *11*, 8346–8355.

(84) Urbach, F. *Phys. Rev.* **1953**, *92*, 1324.

(85) Cody, G. D.; Tiedje, T.; Abeles, B.; Brooks, B.; Goldstein, Y. *Phys. Rev. Lett.* **1981**, *47*, 1480–1483.

(86) Raino, G.; Stöferle, T.; Moreels, I.; Gomes, R.; Kamal, J. S.; Hens, Z.; Mahr, R. F. *ACS Nano* **2011**, *5*, 4031–4036.

(87) Shabaev, A.; Rodina, A. V.; Efros, A. L. *Phys. Rev. B* **2012**, *86*, 205311.

(88) Kamisaka, H.; Kilina, S. V.; Yamashita, K.; Prezhdo, O. V. *J. Phys Chem. C* **2008**, *112*, 7800–7808.

(89) Javaux, C.; Mahler, B.; Dubertret, B.; Shabaev, A.; Rodina, A. V.; Efros, A. L.; Yakovlev, D. R.; Liu, F.; Bayer, M.; Camps, G.; Biadala, L.; Buil, S.; Quelin, X.; Hermier, J.-P. *Nat. Nanotech.* **2013**, *8*, 206–12.

(90) Lupo, M. G.; Della Sala, F.; Carbone, L.; Zavelani-Rossi, M.; Fiore, A.; Lüer, L.; Polli, D.; Cingolani, R.; Manna, L.; Lanzani, G. *Nano Lett.* **2008**, *8*, 4582–4587.

(91) Chilla, G.; Kipp, T.; Menke, T.; Heitmann, D.; Nikolic, M.; Frömsdorf, A.; Kornowski, A.; Förster, S.; Weller, H. *Phys. Rev. Lett.* **2008**, *100*, 057403.

(92) de Mello Donegá, C.; Bode, M.; Meijerink, A. *Phys. Rev. B* **2006**, *74*, 085320.

(93) Feldmann, J.; Peter, G.; Göbel, E. O.; Dawson, P.; Moore, K.; Foxon, C.; Elliott, R. J. *Phys. Rev. Lett.* **1987**, *59*, 2337–2340.

(94) Gurioli, M.; Vinattieri, A.; Colocci, M.; Deparis, C.; Massies, J.; Neu, G.; Bosacchi, A.; Franchi, S. *Phys. Rev. B* **1991**, *44*, 3115–3124.

(95) Monego, D.; Kister, T.; Kirkwood, N.; Mulvaney, P.; Widmer-Cooper, A.; Kraus, T. *Langmuir* **2018**, *34*, 12982–12989.

(96) Kister, T.; Monego, D.; Mulvaney, P.; Widmer-Cooper, A.; Kraus, T. *ACS Nano* **2018**, *12*, 5969–5977.

(97) Wuister, S. F.; De Mello Donegá, C.; Meijerink, A. *J. Am. Chem. Soc.* **2004**, *126*, 10397–10402.

(98) Zenkevich, E.; Stupak, A.; Goehler, C.; Krasselt, C.; von Borczyskowski, C. *ACS Nano* **2015**, *9*, 2886–2903.

(99) Kroupa, D. M.; Vörös, M.; Brawand, N. P.; McNichols, B. W.; Miller, E. M.; Gu, J.; Nozik, A. J.; Sellinger, A.; Galli, G.; Beard, M. C. *Nat. Commun.* **2017**, *8*.

(100) Snyder, R. G.; Strauss, H. L.; Elliger, C. A. *J. Phys. Chem.* **1982**, *86*, 5145–5150.

(101) Srinivasan, G.; Pursch, M.; Sander, L. C.; Müller, K. *Langmuir* **2004**, *20*, 1746–1752.

(102) Badia, A.; Cuccia, L.; Demers, L.; Morin, F.; Lennox, R. B. *J. Am. Chem. Soc.* **1997**, *119*, 2682–2692.

(103) Zhang, H.; Li, F.; Xiao, Q.; Lin, H. *J. Phys. Chem. Lett.* **2015**, *6*, 2170–2176.

(104) Schleeger, M.; Nagata, Y.; Bonn, M. *J. Phys. Chem. Lett.* **2014**, *5*, 3737–3741.

(105) Imry, Y. *Phys. Rev. B* **1980**, *21*, 2042–2043.

(106) Challa, M. S. S.; Landau, D. P.; Binder, K. *Phys. Rev. B* **1986**, *34*, 1841–1852.

(107) Luedtke, W. D.; Landman, U. *J. Phys. Chem. B* **1998**, *102*, 6566–6572.

(108) Doniach, S. *J. Chem. Phys.* **1978**, *68*, 4912–4916.

(109) Mouritsen, O. G.; Boothroyd, A.; Harris, R.; Jan, N.; Lookman, T.; MacDonald, L.; Pink, D. A.; Zuckermann, M. J. *J. Chem. Phys.* **1983**, *79*, 2027–2041.

(110) Clayden, J.; Greeves, N.; Warren, S., *Organic Chemistry*, 2nd ed.; Oxford University Press: 2012.

(111) Chen, Z.; Moore, J.; Radtke, G.; Sirringhaus, H.; O'Brien, S. *J. Am. Chem. Soc.* **2007**, *129*, 15702–15709.

(112) Salem, L. *J. Chem. Phys.* **1962**, *37*, 2100–2113.

(113) Liu, J.; Kilina, S. V.; Tretiak, S.; Prezhdo, O. V. *ACS Nano* **2015**, *9*, 9106–9116.

(114) Frederick, M. T.; Achtyl, J. L.; Knowles, K. E.; Weiss, E. A.; Geiger, F. M. *J. Am. Chem. Soc.* **2011**, *133*, 7476–7481.

(115) Tarafder, K.; Surendranath, Y.; Olshansky, J. H.; Alivisatos, a. P.; Wang, L. W. *J. Am. Chem. Soc.* **2014**, *136*, 5121–5131.

(116) Wu, K.; Chen, Z.; Lv, H.; Zhu, H.; Hill, C. L.; Lian, T. *J. Am. Chem. Soc.* **2014**, *136*, 7708–7716.

(117) Kamat, P. V.; Christians, J. A.; Radich, J. G. *Langmuir* **2014**, *30*, 5716–5725.

(118) Rinehart, J. D.; Schimpf, A. M.; Weaver, A. L.; Cohn, A. W.; Gamelin, D. R. *J. Am. Chem. Soc.* **2013**, *135*, 18782–18785.

(119) Ekimov, A. I.; Hache, F.; Schanne-Klein, M. C.; Ricard, D.; Flytzanis, C.; Kudryavtsev, I. A.; Yazeva, T. V.; Rodina, A. V.; Efros, A. L. *J. Opt. Soc. Am. B* **1994**, *11*, 524.

(120) Norris, D. J.; Bawendi, M. G. *Phys. Rev. B* **1996**, *53*, 16338–16346.

(121) Hanifi, D. A.; Bronstein, N. D.; Koscher, B. A.; Nett, Z.; Swabeck, J. K.; Takano, K.; Schwartzberg, A. M.; Maserati, L.; Vandewal, K.; van de Burgt, Y.; Salleo, A.; Alivisatos, A. P. *Science* **2019**, *363*, 1199–1202.

(122) Rivest, J. B.; Jain, P. K. *Chem. Soc. Rev.* **2013**, *42*, 89–96.

(123) Bronstein, N. D.; Yao, Y.; Xu, L.; O'Brien, E.; Powers, A. S.; Ferry, V. E.; Alivisatos, A. P.; Nuzzo, R. G. *ACS Photonics* **2015**, *2*, 1576–1583.

(124) Benkabou, F.; Aourag, H.; Certier, M. *Mater. Chem. Phys.* **2000**, *66*, 10–16.

(125) Smith, W.; Todorov, I. T. *Mol. Simul.* **2006**, *32*, 935–943.

(126) Wang, L.-W.; Zunger, A. *Phys. Rev. B* **1996**, *53*, 9579–9582.

Appendix A

Synthetic Methods

A.1 Chemicals

cadmium oxide (CdO $\geq$ 99.99%), selenium (Se, 99.99%), tri-n-octylphosphine oxide (TOPO, 99%), oleic acid (OA, 90%),1-octadecene (ODE, 90%),oleylamine (OlA, 90%), and 1-octanethiol ($\geq$ 98.5%) were purchased from Sigma-Aldrich. Octadecylphosphonic acid (ODPA, 99%, PCI Synthesis) and tri n-octylphosphine (TOP, 99%, STREM) were also used. Anhydrous solvents hexanes, acetone, THF, 3-methylpentane, and 2,2,4,4,6,8,8-heptamethylnonane were used after degassing with Ar.

A.2 CdSe core synthesis

wurtzite-CdS core QDs were synthesized using a modified literature preparation.[32] In a typical synthesis, 60 mg of CdO, 280 mg ODPA, and 3 g of TOPO were combined in a 25 mL three-neck round bottom flask. The mixture was placed under vacuum and heated to 150 ^{o}C for 20-30 minutes. The flask was then placed under Ar and heated to 320-325 ^{o}C until the solution turned from red to transparent. Typically this process takes 30-60 minutes. 1 mL of TOP was then injected. The mixture was then heated to between 365-380 ^{o}C and 59 mg of Se dissolved in 0.5 mL of TOP was swiftly injected. Different core sizes can be synthesized by modulating the injection temperature and the growth time. The reaction is allowed to grow for between 30 s and 2 mins before being cooled. 4 mL of toluene was injected as the solution cooled, and the QDs were cleaned with successive precipitation with acetone and redispersion in hexanes.

For the QDs described in Chapter 3, two small modifications were made to this procedure. The reaction scale was doubled, and after complexation at 320 ^{o}C, the flask was then cooled to 150 ^{o}C and placed under vacuum until the line reached its base pressure, which took several minutes.

For the QDs described in Chapter 4, there were also a few modifications to this procedure. For the large core sample, the CdSe cores were allowed to grow for 15 seconds. In order to produce the smaller cores (4.1 and 4.3 nm diameter samples), growth of CdSe must be quenched quickly, which is accomplished through injection of ODE (5 mL) immediately after the TOP-Se solution is injected. In addition, these QDs were precipitated initially with IPA, and no toluene was added after injection.

A.3 CdSe/CdS synthesis

In a typical CdS shelling reaction between 50 and 700 nmol of CdSe cores (concentration determined using absorption[3]), are added to a 3-neck flask with a 1:1 (v/v) mixture of OlA and ODE. Typically, there was a total of 3-6 mL of the OlA and ODE mixture for every 100 nmol of CdSe QDs used. This solution was put under vacuum for 1 hour and then heated to 100-120 ^{o}C for 20 minutes under vacuum. The reaction was then placed under Ar and then heated to 240^{o}C. 0.2 M Cd-oleate (10.25 OA/Cd) in ODE and 0.2 M octanethiol in ODE were then slowly injected to the reaction flask and the solution was heated to 310 ^{o}C. The amounts of Cd-oleate and octanethiol were chosen in order to achieve the appropriate shell thickness. After the injection is complete, the reaction is kept at 310 ^{o}C for 10 minutes, and is then cooled to room temperature. The QDs are purified through subsequent precipitation with acetone and redispersion in hexanes.

For the QDs described in Chapter 2 50 nmol of the 3.4 nm cores were used, dissolved in 1.5 mL each of OlA and ODE. The injection rate of the 0.2 M Cd-oleate and octanethiol solutions was 1.5 mL/hour. For the 4.9 nm CdSe cores, different QD sizes were achieved by taking aliquots of the reaction mixture at different times during the shelling procedure.

The QDs described in Chapter 3 used 700 nmol of CdSe cores to synthesize the initial sample N and the sample on which different chain lengths and stearic acid was exchanged. These QDs and were dissolved 40 mL of ODE. The injection rate of the 0.2 M Cd-oleate and octanethiol solutions was set to 10.5 mL/hour. Due to the fast injection rate, the solution was allowed to stir at 310 ^{o}C for at least 30 minutes after the reaction completed. For the sample described in Figure 3.3 200 nmol of CdSe cores were used.

The QDs described in Chapter 4 were synthesized in a mixture of ODE and OlA. For the 4.1 nm QDs 4 mL of ODE and 4 mL of OlA were degassed, and 200 nmol of CdSe cores were added. The Cd precursor solution contained 0.1 mmol of $Cd(OA)_2$ in 1 mL of ODE, and the S precursor solution contained 17.3 μL of octanethiol in 1 mL of ODE (each solution was 0.1 M). The solution was injected over the course of 1 hour. The 4.3 nm QDs were synthesized at a 400 nmol scale with 8 mL each of ODE and OlA. The Cd and S precursor solutions were each 0.1 M, and 2 mL of each precursor solution was injected of 1.5 hours. The 6.3 nm core/shell QDs were synthesized on a 100 nmol scale in 3 mL each of ODE and OlA. The Cd precursor solution had 0.144 mmol of $Cd(OA)_2$ and the S precursor solution had 30 μL of octanethiol, both in 2 mL of ODE, and were injected over the course of 1.5 hours. All QDs in this chapter were kept at 310 ^{o}C for 10 minutes after precursor injection.

A.4 Ligand Exchanges

Ligand exchanges from OA to different phopshonic acids and stearic acid were performed in THF. Approximately 100 nmol of QDs is dissolved in 5-15 mL of THF under Ar. The phosphonic acid or stearic acid is then added as a solution in THF. The phosphonic acid exchanges are approximately quantitative, while the stearic acid exchanges are driven mainly

by mass action, and therefore an excess of stearic acid is required. The exchanges are allowed to stir for an hour. Excess solvent is then evaporated until there is less than 2 mL of THF present. The QDs are then precipitated with antisolvent and resuspended in hexanes two to three times. Ligand composition is determined using proton NMR spectroscopy.

Appendix B

Spectroscopic and Computational Methods

B.1 Cryostat PL and TRPL measurements

Temperature-dependent photoluminescence measurements were taken using a time-correlated single photon counting apparatus. The apparatus consisted of a Picoquant Fluotime 300 spectrometer, a PMA 175 detector, and a LDH-P-C-405 diode laser with a 407 nm excitation wavlenegth, and approximately a 50 ps pulse width. Repetition rates were tuned between 500 kHz and 10 MHz depending on the lifetime of the QD sample. For each pulse, the maximum pulse power is less than 0.3 nJ, which would result in $\ll 1$ excitations per QD each pulse. The temperature was tuned using a Lakeshore 330 temperature controller, and samples were prepared by dissolving a small amount of QDs in 2,2,4,4,8,8-heptamethylnonane or 3-methylpentane, optical glass forming solvents. Two different sample cells were used which consisted of two sapphire windows and an inert (Teflon or Ti-coated Al) spacer. It is important to choose an appropriate spacer, as there can be significant interactions between

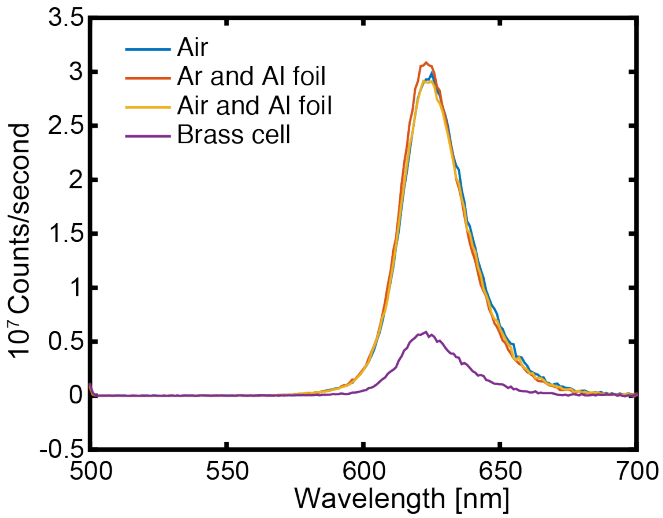

Figure B.1: QD quenching for different sample cell materials. A solution of QDs is put overnight in four different configurations, and the PL is then measured. Significant quenching due to the brass cell is observed.

QDs and spacer. For example, when the spacer used is brass, the QD photoluminescence is quenched. As Cu can easily cation exchange with Cd in CdSe,[122] the presence of trace surface oxides could result in quenching of QD photoluminescence. This is shown in Figure B.1, in which the brass cell quenches native QDs by a almost a factor of six compared to QDs kept in air or in contact with Al foil.

B.2 Temperature-dependent integrating sphere measurements

QDs were added to 0.4 mL of 3-methylpentane in an NMR tube, such that the O.D. at 500 nm was approximately 0.2 (approximately 50x dilution from NMR concentrations). The NMR tube was flame-sealed, samples were flash frozen in liquid N_2 and PLQY was collected as they warmed in an integrating sphere setup[123] using a 500 nm excitation. As the emission peak wavelength varies with temperature, we can relate the emission peak position through the Varshni relation to the temperature, using temperature-dependent PL measurements taken in an optical cryostat as described in Section B.1. For the QD sample described in Figure 3.4, this first processing step is shown in Figure B.2.

The calibration appears relatively accurate, however there is a non-monotonic behavior around the phase transition region that is present in sample L3 (84% ODPA). This behavior is clearly not physical, and can be explained by non-monotonic behavior in the temperature-dependent emission peak around the phase transition temperature (shown in the region around 200 K). This is shown in Figure B.4 , in which the temperature from emission calibration is shown against time for sample N (36% ODPA). Around the observed phase transition temperature there is a slight kink in the temperature calibration. This behavior could potentially be due to a size distribution present in the sample. If smaller dots disorder at lower temperatures, there will be a slight blue shift as temperature increases around the phase transition point. This would be most significant in samples that have a sharp phase transition, as is evident in Figure B.2.

It is possible to improve the temperature calibration by adding another constraint: simply, that over time, the temperature increases as the sample warms up. This can be modeled using a fit with Newton's law of cooling:

$$T(t) = T_{\text{room}} + (T_{\text{initial}} - T_{\text{room}})\text{e}^{-kt} \tag{B.1}$$

We use a global fit to the room temperature over each sample run to extract the appropriate parameters. The time constant k is allowed to vary as it is possible slight changes in orientation could change the convection and thus the rate of heating and the time constant T_{initial} is allowed to vary as the time between the sample being flash-frozen and the beginning of data collection is variable. The fits are shown in Figure B.4. The result of this additional calibration step is to slightly increase the apparent width of the phase transition, as shown in Figure B.3. This offsets the error from the calibration to a slight blue shift with increasing

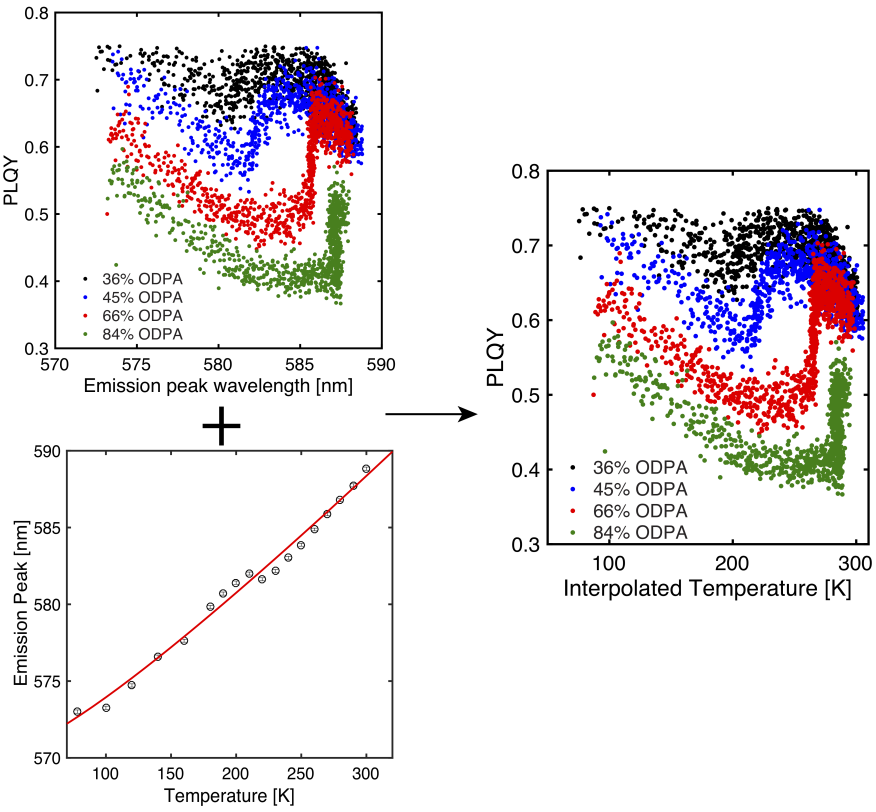

Figure B.2: Temperature calibration using emission: The raw PLQY data are plotted against the emission peak wavelength. Temperature-dependent photoluminescence data collected in a cryostat on the 36% ODPA sample (N) is used to calibrate the temperature.

temperature that is present in the emission-only calibration method. Furthermore, it is clear that this fitting method resolves the un-physical non-monotonic behavior that was observed in the 84% ODPA sample.

This fitting method is sufficient to achieve reasonable temperature calibrations, but there are still some issues inherent to this method. The use of the emission peak as an internal calibrant is somewhat inconvenient, as evidenced by the necessity of performing the Newton's law of cooling fit as described in Figure B.3. A cleaner approach might be to use an external calibrant in the integrating sphere that has no non-monotonic behavior, which would enable simpler calibration. One possibility is to use a sample of thick-shell QDs as the standard for determining the temperature. This would also reduce the number of required cryostat measurements, which would simplify and expedite the temperature-dependent PL workflow. There are several requirements for this QD sample. These QDs should have a strong absorption at the excitation wavelength, 500 nm, they should be a high PLQY, the PLQY should not change with the temperature, the emission should vary smoothly with temperature, and the emission peak should be sufficiently shifted from the sample emission

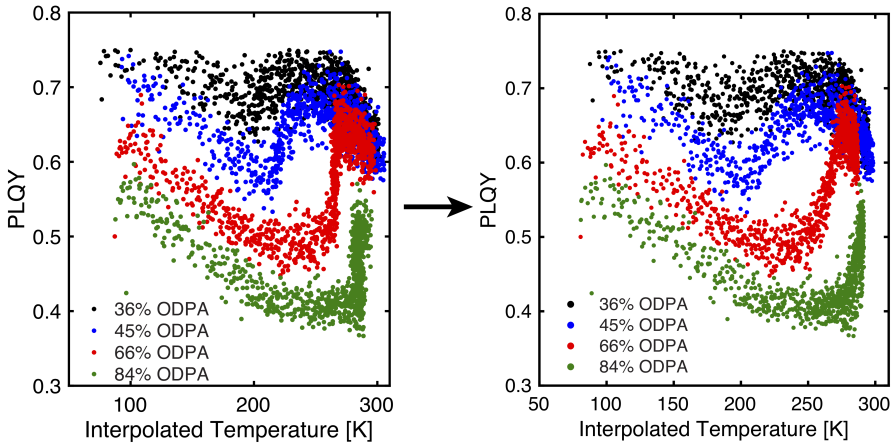

Figure B.3: Temperature calibration using emission and time: We use a Newtons law of cooling model to further process the temperature data. The results here show that it has minimal impact on the curves, except to somewhat stretch out the phase transition and to remove the apparent non-monotonic behavior shown in the 84% ODPA sample (L3).

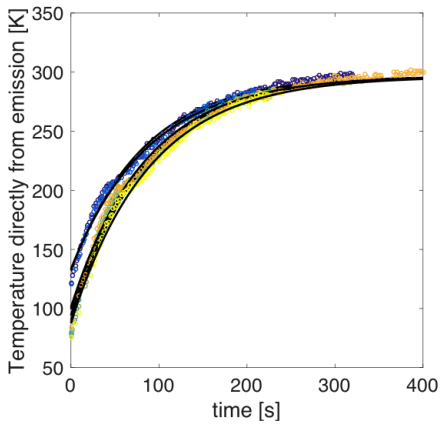

Figure B.4: Newton's law of cooling fits. Temperature from the Varshni interpolation vs. time for the 36% ODPA sample (N), The black lines show the Newtons law of cooling fit used to determine the final temperature.

to decouple them. Conveniently, all of these requirements can be met by using a sample of thick shell CdSe/CdS QDs, as shown in Figure B.5.

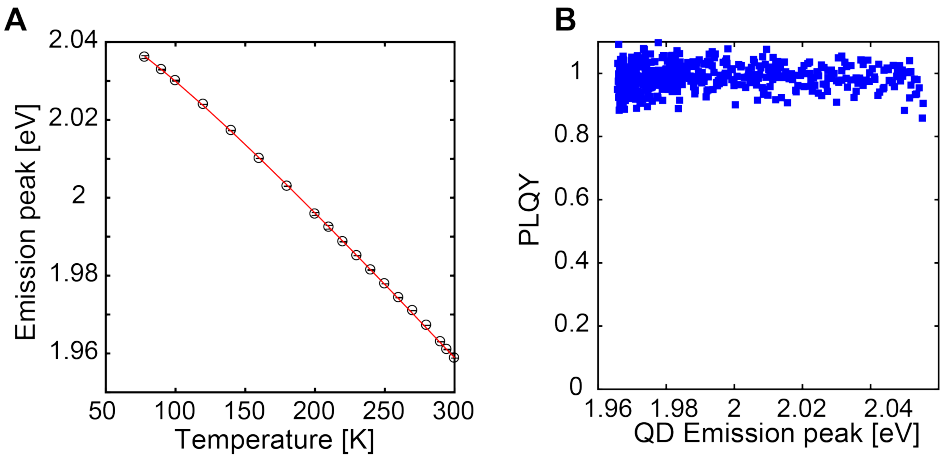

Figure B.5: External QD for temperature calibration. A) Shows that the emission shifts smoothly with temperature, without any non-monotonic behavior that is observed in the thin-shell QD samples. B) The PLQY of this sample is high and does not change with the temperature.

Just as the Newton's law of cooling calibration method broadens the transition region, the external standard method results in a similar calibration change. Shown in Figure B.6 is the PLQY versus the emission of the thin-shell QD, using the same sample discussed in Chapter 3. We note that the phase transition behavior is somewhat shifted from what is observed in Chapter 3, as these measurements occurred significantly after the previous measurements, which results in a slightly different ligand shell coverage density. The sharp jump characteristic of using the thin-shell QDs as the calibrant is clearly visible in Figure B.6. This is in strong contrast with the observed behavior when using the external calibrant to determine the temperature, as shown in B.7.

While this method is of use in more precisely determining the temperature, it does introduce some error into a precise determination of the PLQY. As there are not error bars for each individual data point here, it is difficult to separate out the component of the PLQY that arises from the standard against the component that arises from the sample without additive error bars in determining the PLQY. For this reason, this calibration method was not used in either Chapter 3 or 4. However, this calibration method does qualitatively reproduce the changes observed using the Newton's Law of Cooling method, which suggests such a calibration is valid.

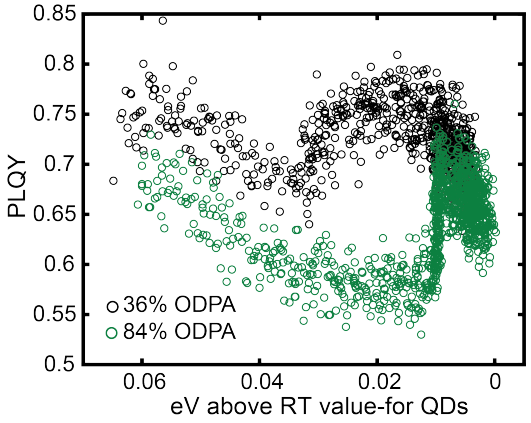

Figure B.6: Phase transition behavior using same QDs as the calibrant.

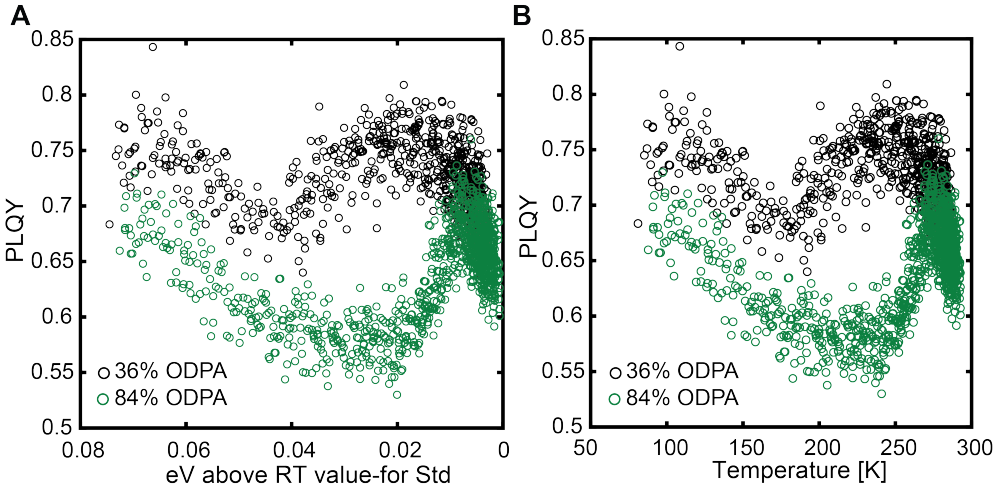

Figure B.7: QD PLQY using the external calibrant: A) Shows that the observed PLQY as a function of the emission peak of the standard B) shows the PLQY as a function of temperature using the external calibrant.

B.3 VT-FTIR measurements

QDs were dried and then redispersed in $CDCl_3$ such that the ligand concentration is approximately 20 mM. This solution was loaded into a 500 μm path length Specac Variable Temperature IR cell with CaF_2 windows. FTIR data were collected on a Nicolet 6700 FT-IR Spectrometer upon warm-up.

B.4 SFG measurements

Quartz substrates were prepared by cleaning with Nochromix solutions and then successive washings with water, IPA, and toluene. QDs were deposited *via* spin-coating from a 200 nM solution of QDs in toluene. The picosecond laser system consisted of a 1064 nm Nd:YAH pump laser (PL2230 Ekspla) with a repetition rate of 50 Hz and an average peak power of 25 mJ. A LaserVision optical parametric generator and amplifier system converted the 1064 nm to a visible 532 nm beam and a mid-IR beam ranging between 2200 and 4000 cm^{-1}. The visible and infrared beams overlap spatially and temporally on a medium. The beam angles were 34^o and 48^o respectively, regarding the perpendicular plane to the sample surface. We collected the SFG beam (in the UV range) by a Hammamatsu photomultiplier tube. We added several band-pass filters to minimize stray 532 nm light.

B.5 PL quenching curves

PL quenching curves were performed by mixing QDs with a known concentration of ferrocene ligands and measuring the PLQY relative to the native QDs on a Horiba Jobin Yvon TRIAX 320 Fluorolog. These quenching curves were performed on 3 mL of approximately 300 nM QD solutions in hexanes, with 10μL aliquots of a ferrocene ligand solution added. NMR measurements confirmed quantitative binding for the 3.6 nm and 4.1 nm QD samples, but for the 6.3 nm QD sample, an equilibrium ligand exchange model is used to determine binding in the PL quenching curves.

B.6 Quantitative NMR

Quantitative proton NMR were obtained on a Bruker 400 MHz instrument. The absolute concentration of the ligands is computed by referenced an external standard of 10 mM ferrocene in toluene-d_8. For quantitative NMR spectra the 90^o pulse width was calibrated.

B.7 TEM

Transmission Electron Microscopy (TEM) of QDs was performed using a an FEI Tecnai T20 with a LaB filament and 200 kV of acceleration. QD samples were prepared by drop-casting dilute QD solutions onto a a carbon film 400 square mesh copper grids.

B.8 Determination of QD concentrations

In order to determine the concentration of core/shell QDs in solution, a number of techniques are required. The QD concentration was determined by measuring the concentration of Cd^{2+}

using an Optima 7000 DV ICP-AES. The size of the QDs are determined using Transmission Electron Microscopy (TEM). ICP was performed by compared a sample of QDs digested with nitric acid and then diluted with Millipore water to similar concentrations as a series of Cadmium ICP standards. By correlating the optical density and volume of the QDs in the ICP measurements, the concentration of QDs in subsequent solutions can be determined.

B.9 Ising model simulation

The Ising model used was implemented in Matlab, with 10^7 Monte Carlo steps using the Metropolis sampling algorithm to ensure the system reached equilibrium. The lattice simulated was a 15x15 square lattice, which would correspond to a surface coverage of 2-3 ligands/nm^2 for the QDs studied. 20 different OA configurations were averaged over for each data point in order to account for variation in the phase transition properties depending upon the random configuration of OA in the sample.

B.10 Computation of temperature-dependent emissions and lifetimes

All nanoparticle structures used consist of a wurtzite lattice and have an approximately spherical shape. The configurations were obtained by taking a sufficiently sized wurtzite crystal with a lattice constant similar to bulk CdS, and cleaving it down to the desired size. Then, all S atoms with a distance of the core radius from the center point were replaced with Se atoms.

These configurations were the starting points for energy minimization simulations. After the configurations were quenching, 10-20 constant temperature molecular dynamics runs of 100 ps were performed for each temperature. The forces between atoms were modeled using a modified Tersoff-type potential that was developed by Benkabou et al.[124] The simulations were carried out using the DLPOLY simulation package,[125] with a Berendsen thermostat and a 1 fs time step. Equilibrium for all structural properties was reached for each of these molecular dynamics runs. The potential energy and the lattice constants of the materials fluctuated around constant average values, without observable drift. The properties calculated including (HOMO, LUMO, oscillator strength, lifetimes) were achieved by averaging over the set of configurations.

In order to effectively calculate the electronic structure, surface dangling bonds were passivated by ligand potentials. This was done using the outermost monolayer of Cd and S atoms, and the following procedure. All Cd and S atoms with less than four nearest neighbors are removed from the configuration. Then all Cd (S) missing bonds are passivated by adding a potential that corresponds to a S (Cd). The ligand potentials used were taken from Wang et al.[126]